

Assessing fluid migration around fault in the Aurora CO₂ storage site, combining seismic analysis and outcrop data

Victoria Kjeldstad



Master Thesis in Geosciences
Structural Geology and Tectonics
60 credits

Department of Geosciences
Faculty of Mathematics and Natural Sciences

UNIVERSITY OF OSLO

June 2023

© Victoria Kjeldstad

2023

Assessing fluid migration around fault in the Aurora CO₂ storage site, combining seismic analysis and outcrop data

Supervisors: Alvar Braathen, Nora Holden, Rikke Bruhn

This work is published digitally through DUO – Digitale Utgivelser ved UiO

<http://www.duo.uio.no/>

Printing: Graphic Centre, Universitetet i Oslo

Acknowledgements

First, I will express my gratitude to my supervisor Alvar Braathen at the Department of Geoscience, University of Oslo. Thank you for the guidance and expertise and for giving me this exciting topic that fulfilled my two wishes of combining seismic interpretation and fieldwork. I am very grateful for my co-supervisor Nora Holden; you were my close travel companion in Floy Canyon, and your guidance in fieldwork and seismic interpretation was extremely helpful. Thank you, Rikke Bruhn, for your expertise in sedimentology and contribution to writing feedback.

Secondly, I will thank the Norwegian CCS Research Center (NCCS) for funding my travel expenses in Floy Canyon, including the payments for the stay at the motel in Green River.

Finally, I would thank my partner William Jarbeaux for being a great source of motivation and support during these challenging times. A last thanks to my family for their unwavering support and interest in my studies.

Oslo, Norway. June, 2023

Victoria Kjeldstad

Preface

This master thesis (ECTS 60) is submitted to the Department of Geosciences, University of Oslo (UiO), as a part of the Structural Geology and Tectonics program in the Master of Science in Geosciences (ECTS 120). The main supervisor of the thesis is Professor Alvar Braathen (UiO), and co-supervisors are Doctoral Research Fellow Nora Holden (UiO) and Adjunct Associate Professor Rikke Bruhn (UiO, Nautilus Carbon Services).

This master thesis work is an integral part of research into CO₂ storage at the Department of Geosciences, UiO, contributing to the Norwegian CCS Research Center (NCCS). The principal scope of all the work is on CO₂ sequestration in the North Sea Basin. Seismic data is courtesy of Gassnova SF, which images the Aurora CO₂ storage site. The data from the 31/5-7 well is provided by the NPD Diskos repository and the Northern Lights project (Equinor ASA, Total E&P Norge AS, and A/S Norske Shell). The software used in this thesis is the courtesy of Schlumberger (Petrel E&P Software Platform) and Petroleum Experts (Move suite).

Abstract

This thesis addresses how minor faults affect CO₂ migration. To achieve this goal, the study combines a detailed seismic interpretation of an isolated fault (F1) located in the Aurora CO₂ storage site, complimented with detailed mapping of outcrop faults exposed in the Floy Canyon in the foothills of the Book Cliffs (Utah, SW USA). The Aurora CO₂ storage site in the Horda Platform (northern North Sea) represents the Northern Lights project's current target for CO₂ storage. Due to the dip of the storage unit, buoyant CO₂ injected into well 31/5-7 is expected to migrate north and first encounter the smaller scale fault F1.

Significant uncertainties exist around the influence of faults on the migration of a CO₂ plume: hereunder fault interpretation strategies, limitations in seismic resolution, and input parameters in reservoir modelling. Therefore, detailed assessment of faults in outcrops provide a better understanding of how faults in the subsurface may influence fluid migration pathways. Evaluating the sealing capability of fault outcrops combined with methods used to assess across-fault juxtaposition and membrane seal in the context of seismic data, offer a powerful blend to test the reliability of today's methods in subsurface reservoir seal assessment.

Results from the Floy Canyon area show that the five selected faults display a distinct structural geometry and spatial distribution of structural elements that can be classified into fault facies categories (discrete structures, membranes, and lenses), which cannot be resolved in seismic data. The extensional faults in Floy Canyon are considered an analogue to the F1 fault in Aurora due to similar throw magnitudes and depositional environment. The fault facies sealing evaluations show varying results, such as two faults containing sand lenses that can allow across fault fluid pathways. Simple Shale Gouge Ratio (SGR) calculation at a point in each fault of Floy Canyon show that three out of five faults' SGR sealing probability fit the outcrop fault facies sealing evaluation, whereas two faults challenge the SGR predictions. The latter structures offer possible migration routes within the fault core despite a juxtaposition seal being present. In conclusion, SGR techniques to predict fault-seal probability in the surface comply with a very general framework for the fault. Adding fault facies analogues into the discussion nominate certain points and zones in the fault which fluids may flow along and bypass the structure.

Table of Contents

Acknowledgements	III
Preface	IV
Abstract	V
1 Introduction	1
1.1 Motivation.....	1
1.2 The technological process of Carbon Capture Storage (CCS).....	2
1.3 General geological properties required to store CO ₂ in the subsurface.....	4
1.4 Background information of the Aurora site and Floy Canyon area.....	5
1.5 Aim of study.....	6
2 Geological setting	8
2.1 Geologic setting of Utah.....	8
2.1.1 Geologic history of Utah.....	8
2.1.2 Structures and stratigraphic column of Upper Cretaceous Floy Canyon.....	13
2.2 Geologic setting of the northern North Sea.....	16
2.2.1 Structural framework.....	16
2.2.2 Geological history of northern North Sea.....	17
3 Theoretical framework	23
3.1 Fault zone architecture of normal faults.....	23
3.1.1 Across – fault seals.....	25
3.1.2 Fault Facies classification.....	26
3.2 Fault development.....	29
3.2.1 Fault throw and growth.....	31
3.3 Across-fault seals.....	33
3.3.1 Juxtaposition seals.....	33
3.3.2 Membrane seals.....	34
3.3.3 Possibility of sealing sand lenses and internal structures.....	37
4 Methods and data	39
4.1 Fieldwork.....	39
4.1.1 Equipment.....	39
4.1.2 Scan line data.....	40
4.1.3 Fault facies interpretation.....	40
4.1.4 Processing field data.....	41
4.1.5 Sealing assessment.....	41
4.1.6 Field data limitations.....	41

4.2	Seismic interpretation data	42
4.2.1	3D seismic data	42
4.2.2	31/5-7 well data.....	45
4.2.3	Velocity model.....	45
4.2.4	Data Limitations.....	45
4.3	Seismic interpretation methods	46
4.3.1	Eos well tie	47
4.3.2	Horizon interpretation	48
4.3.3	F1 – fault interpretation.....	50
4.3.4	F1 – fault modelling and analysis	50
5	Results	52
5.1	Floy Canyon outcropping faults.....	52
5.1.1	Facies description and interpretation.....	53
5.1.2	Fault facies descriptions and interpretations	59
5.1.3	Net-to-Gross and SGR calculations	75
5.2	Seismic fault interpretation of F1 in Aurora storage site	75
6	Discussion.....	83
6.1	Geological comparison of the North Sea and the Book Cliffs.....	83
6.1.1	Stratigraphic similarities	84
6.1.2	Comparison of faults	85
6.2	Field data uncertainties.....	87
6.3	Seismic interpretation uncertainties	87
6.4	Floy Canyon; Fault facies and sealing capabilities	88
6.4.1	Presence of fault seal.....	89
6.4.2	Implications for fluid migration	91
6.5	SGR-calculation – Floy Canyon	94
6.6	F1 -Aurora storage site interpretation	95
6.6.1	Extended fault tips.....	96
6.7	Fault seal assessment of Aurora F1 fault in light of outcrop analogues of Floy Canyon	97
6.8	Further research.....	102
7	Conclusion.....	104
	Reference list.....	106
	Appendix	119

1 Introduction

This study will assess how smaller-scale faults could affect the CO₂ migration of the Aurora storage site. Both seismic data and physical outcrop observations will be used in this study to evaluate the properties and impacts of smaller-scale faults in sedimentary basins. This chapter provides insight to motivations behind CCS operations, followed by general structural characterizations for a storage site, and some background information of the main study. In the end the chapter outlines the main aims for this study.

1.1 Motivation

This thesis targets CO₂ storage technology with its current knowledge needs. These needs can be seen from a global and political perspective, as outlined here. The consequences of global warming can be severe if the Paris Agreement cannot be accomplished, where the goal is to limit the rise of global temperature to 1.5°C (IEA, 2021). To realistically achieve such a goal, we need to reach net-zero emission globally by 2050, which will unlikely happen without the help of Carbon Capture Storage (CCS) technology (IPCC, 2005). We are in the right direction of implementing clean energy technology such as renewable energy sources; sunlight, wind, hydro and geothermal energy. Even though most industries can vastly reduce CO₂ emissions, the production of cement, chemicals and steel are the hardest ones to reduce; therefore, CCS is an essential technology that stores the CO₂ emissions instead of releasing it into the atmosphere (IEA, 2021). Other existing CO₂ capture technologies such as direct air capture and storage (DACCS) using aquifers and sea as a CO₂ storage are still under development but often have the problem of low efficiency, energy loss, lack of technology innovation and little information on the storage area (Shreyash et al., 2021). Therefore, developing technologies or using available technology implemented in areas that are highly known and studied can offer higher efficacy in lowering CO₂. Using aquifers as underground storage is also possible, but the lack of information on their heterogeneities in sandstone aquifers and the existence of a suitable seals can delay the process (Freund & Ormerod, 1997).

Meanwhile, for decades, CCS technology in geological sequestrations has been used in oil and gas industries where the CO₂-based enhanced oil recovery (EOR) was applied (Shreyash et al., 2021). This method is based on injecting CO₂ into existing oil wells to recover oil in the reservoir. Furthermore, CCS in reservoirs is certain to contribute to controlling the changes in

climatic conditions. Suitable CO₂ storage sites, including large storage space, are crucial since the amount of CO₂ captured annually is exceptionally high, whereas the IPCC (2018) cited in Global CCS institute (2021) states that 5-10 gigatons (Gt) of CO₂ must be captured each year in the second half of this century to limit the rise of global temperature to 1.5°C. Consequently, using depleted oil and gas reservoirs as a storage site for CO₂ is an attractive solution because of the knowledge gained from previous petroleum explorations (e.g., detailed geological structures, already existing geological seals) (Freund & Ormerod, 1997).

1.2 The technological process of Carbon Capture Storage (CCS)

Norway has been one of the leading countries in CCS and has kept working with this technology since 1996 (Lipponen et al., 2017), when the oil company Equinor started to inject CO₂ into the Sleipner Field in the North Sea. The subsequent 16 years of injection into this field have been performed without significant operational problems (Torp & Gale, 2004). Another CCS operation by Equinor is the Snøhvit Field in the Barents Sea, that has seen CO₂ injection for 15 years, since 2008.

The Government in Norway is planning on full-scale CCS operation on the Northern Lights project Longship by mid-2024. This project will demonstrate that CCS is a safe and feasible solution for permanent underground storage for industries (Norwegian Ministry of Petroleum and Energy, 2020). For this endeavour to take place with uttermost success and learning gains, research has been performed by the Norwegian CCS Center (NCCS). This is a Center for Environment-friendly Energy Research funded by the Research Council of Norway and industry, which contributes to the CCS landscape in Norway. NCCS aim to work alongside the Northern Lights project and is funded for the period 2016-2024. The centers main mission is to fast-track CCS deployment (NCCS, 2021). Figure 1.1 demonstrates the basic process of CCS based on the Northern Light project. The Aurora storage site in the Horda platform located in the northern North Sea represents the current target for CO₂ storage led by Equinor, Total and Shell (owners of Northern Lights). The Containment Risk Analysis (CRA), a process of evaluating if the storage complex is safe for storing CO₂, needs to first take place before transporting CO₂ starts. The Northern Lights CCS project can start if the storage site is safe (e.g. low risk of leakage) (Furre et al., 2020).

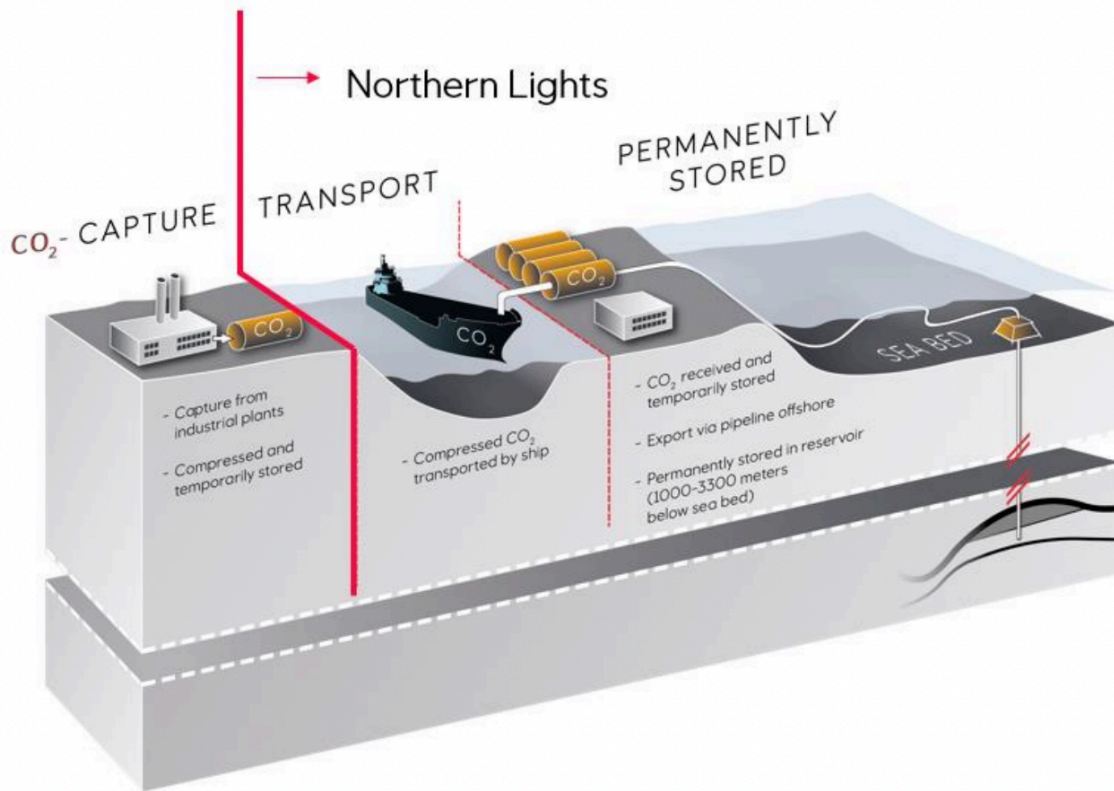


Figure 1.1 – Northern Lights CCS project illustration. The CO₂ will be captured onshore from industrial sources in the Oslofjord region and transported in liquid form by newly designed ships to the storage sites. The CO₂ gets injected through pipelines and permanently stored in an offshore storage complex in the North Sea. Figure from Equinor (2019).

As mentioned, this thesis targets the Aurora site that will see the CO₂ injection in 2024 by the Northern Lights company (industry consortium). The first step of the CCS process is to capture the CO₂ from industrial sources in the Oslofjord region (Equinor, 2019). The second step is compressing the CO₂ into liquid form in cargo tanks on ships at onshore terminals, for transport to a process hub in West Norway. Thereafter, the liquid CO₂ will be piped from the onshore process hub to the offshore injection well. The liquid CO₂ will, at last, be injected into a Lower Jurassic storage complex (i.e., storage and seal unit) within the Aurora storage site (Equinor, 2019). Besides ensuring that the storage site is safe for injecting, it is also crucial to ensure that the procedure of transporting the CO₂ from the industrial site to the storage complex follows through safely. Whereas the safest way to transport CO₂ is in single-phase condition (liquid), it is important to ensure that the storage vessels, cargo tanks, and pipelines can safely manage such pressure (Equinor, 2019). The CCS operation is completed when the CO₂ is injected into the reservoir. What is left is monitoring the plume migration to see if the storing of CO₂ goes safely and can get an early detection if the CO₂ behaves undesirably and vastly take action to correct it (Furre et al, 2020).

1.3 General geological properties required to store CO₂ in the subsurface

CO₂ will be injected into the Lower Jurassic sandstone aquifers in the Aurora storage site approximately 2.6 km below the seabed (Equinor, 2019). The reservoir pressure is expected to secure liquid phase conditions, which reassures that the CO₂ stays in the single-phase condition throughout the operation. First, a storage site must be aseismic and tectonically stable to make sure that there are no major earthquakes and active volcanism that can initiate faults and rupture (Bachu, 2000). Another requirement for the CO₂ storage is the material properties of the storage units. The storage units must consist of a suitable sandstone reservoir with high porosity and permeability and extends in wide areas to store large amounts of CO₂ (Furre et al, 2020). The second criterion is the caprock to prevent CO₂ migration from the reservoir and again leaking into the atmosphere. The seal above the storage unit consists of non-permeable rock (e.g., shale), to seal the CO₂ in the reservoir. The third criterion is the fault properties, where the faults can act as barriers or conduits for up-fault CO₂ migration. If the fault act as a conduit for up-fault fluid migration, the CO₂ can migrate up along the fault, resulting in CO₂ leakage (Bretan et al., 2011). Faults can also consist of migration pathways (sand-sand juxtaposition) where CO₂ might migrate through the fault (depending on the pore pressure communication) but do not contribute to leakage to the atmosphere. Any leakage risk indicator in faults will result in a high possibility of CO₂ migrating up to the surface, thereby becoming released into the atmosphere. Another potential leakage event is if the CO₂ escapes the storage complex and migrates to non-storage areas; hydrocarbon fields could potentially result in contamination of the area (Furre et al., 2020). Although these are the essential criteria to store CO₂, other structural factors such as damage zone, fault facies, deformation bands and migration pathways are crucial to assess when predicting where the CO₂ will migrate. Therefore, a thorough outcrop study of fault properties in Floy Canyon of eastern Utah will be essential to comprehending structures in the damage zone and fault facies, which are small-scale structures where the seismic data cannot resolve.

1.4 Background information of the Aurora site and Floy Canyon area

The Aurora CO₂ storage site is located in the Horda platform within the northern North Sea, and offers a suitable storage and caprock seal. The 31/5-7 confirmation well (Eos) (Figure 4.1 in chapter 4) was drilled by the Northern Lights project from the 2nd of December 2019 to the 7th of March 2020 to confirm the presence of suitable storage and seal within the Aurora CO₂ storage site (Furre et al., 2020). The Northern Lights project will likely inject CO₂ at or near the location of newly drilled Eos 31/5-7 well (Figure 4.1). Due to a gentle southerly dip of the storage unit, the buoyant CO₂ is expected to migrate northwards towards and underneath the Troll West field. Migrating CO₂ will encounter numerous faults (Furre et al., 2020). The Aurora CO₂ storage site offers several faults formed during multiple rift phases. Previous research, such as by Bretan et al. (2011), analyzed in-situ stresses in the Troll West field and concluded that the faults are not close to failure; therefore, upfault leakage of CO₂ is unlikely to happen. In a study of the Aurora field faults, the conclusion is that there is low risk of CO₂ migration out of the storage units and the faults within the storage unit overall gives a positive impact on CO₂ storage capacity (Holden et al. 2022). When the CO₂ become injected into the Aurora field, it will first encounter numerous smaller-scale faults (Furre et al. 2020). All faults, smaller and larger, can act as barriers, baffles and/or conduits to fluids. A sealing fault will restrict the CO₂ migrating, and a permeable fault can act as a travel path for the CO₂ (Bjørlykke, 1993). The previous studies of the Aurora and Troll West fields mainly focused on the larger-scale faults and second-order faults (smaller-scale faults). Faults of all sizes plays a crucial role in accommodating deformation and effecting fluid flow (Caine & Forster, 1999; Faulkner et al., 2010). Therefore, a study that focuses mainly on the first encountering smaller-scale faults and its sub-seismic structures are of significance to understand more of the possible fluid migration pathways. The isolated F1 fault (Figure 4.1 and 5.13) fault will be the first structure the CO₂ plume encounter. The importance of this fault on CO₂ storage in Aurora is the focus of the work – covered in the seismic interpretation part of this thesis and further considered through an analogue (outcrop) case study.

Because of the resolution limits of seismic data, outcrop observation provides higher-detail information of sub-seismic structures and fault zone architecture in sedimentary basins. Analysis of well-exposed normal faults in the Floy Canyon in the foothills of the Book Cliffs of Eastern Utah (USA) with similar properties as the F1 fault in the Aurora site will be used as

an addition instrument to enhance the understanding of CO₂ migration in the Aurora storage site. The Book Cliff contains sedimentary units deposited in offshore marine to shallow-marine and terrestrial environments, seen as sandstones, shales, and local coal seams (Davies et al., 2006). The exposed normal faults in the Floy Canyon allow us to investigate the fault core and the damage zone to identify structures such as deformation bands, smears, mixed units, slip surfaces, etc. (Braathen et al., 2009), which cannot be studied in seismic interpretation. Detailed analysis of outcropping faults (i.e., fault zone architecture, fault rock composition) such as the case study of the Floy Canyon (Utah), provide essential information that can be used to further assess the CO₂ migration along and across smaller-scale faults in the Aurora CO₂ storage site, northern North Sea.

1.5 Aim of study

This study will provide a better understanding of how smaller-scale faults influence the migration of CO₂. Datasets and analyses combine the detailed seismic interpretation of the isolated fault F1 (Holden et al., 2022) in the Aurora CO₂ storage site with mapping of outcrop faults exposed in the Floy Canyon (Utah, SW USA). The seismic interpretation and modelling objectives are to provide a detailed seismic analysis of a 3D seismic cube that covers fault F1 in the Jurassic delta system of the Aurora site. The seismic interpretation will include a detailed interpretation of key fault F1, key horizons across F1 fault, and potentially generate and visualize total fault displacement and attribute (e.g., strike, dip, curvature) analysis to inform fault complexities on seismic scale. In addition, outcrops in Utah with exposed fault within similar paleogeographic (sedimentary facies) setting as in the Aurora site will be used in this study to aid the learnings derived from the seismic interpretation. The objectives for outcrop studies in Utah are:

- (i) Analysis of well-exposed normal faults in the Floy Canyon area that deforms mildly consolidated delta deposits of the lower Book Cliffs.
- (ii) Analyze fault facies distribution in faults located in the Floy Canyon and assess the presence of mud and coal smearing in the fault cores. We will assess whether we can identify a throw on the fault with a through-going slip surface (fracture). The third objective of the outcrop studies

(iii) Analyze the damage zone in poorly consolidated sand, shale and coal successions. We identify the deformation bands in porous rocks and assess whether the damage zone is controlled by lithology and porosity, emphasizing fracture vs. deformation bands.

Four scientific questions are considered to address the main objectives of this study. These questions will be analyzed and will be discussed towards the end of the thesis.

- Is there a relationship between calculated SGR values for faults and the presence of clay membranes in the faults?
- Will the presence of coal and mud in the host rock create smears within the fault core?
- Are there continuous smears or clay membranes that will act as barriers for across-fault flow?
- Will there be indications of across- or up-fault fluid migration based on the fault facies architecture?

2 Geological setting

In this chapter I will present the geological setting of the Floy Canyon in the eastern Utah, USA (sub-chapter 2.1) and the Horda Platform in the northern North Sea, Norway (sub-chapter 2.2). Both locations are presented with a description of the general geological history of that area, followed by a detailed description of the stratigraphy. Since the Floy Canyon provides a physical analogue for the Horda Platform, there are similar depositional environment and tectonic influence in both areas. The Book Cliffs in Floy Canyon contain the Blackhawk Formation, which consists of a succession that progrades into the Mancos Shale and demonstrates a variety of wave-dominated to fluvial-influenced deltaic facies and shelf facies. (Chan et al., 1991). Similarly, formations and groups in the Horda Platform contain continental and fluvial-deltaic to shallow-marine affinity (Deegan & Scull, 1977).

2.1 Geologic setting of Utah

The geological history of Utah links to its diverse landscape, such as the rugged mountains of the Uinta Range, large volcanic fields in western Utah, canyons, and the basins (Hintze, 1988). Figure 2.1 shows the Utah state and the area around Floy Canyon.

2.1.1 Geologic history of Utah

Utah's geological history traces back to the Archean to the early Proterozoic (3000 – 1000 million years ago (mya)). The rocks of this period are metamorphosed gneisses, schists, and some granitic pegmatites (Hintze, 1988). In Proterozoic to Devonian times (1000 – 360 mya), Utah formed the western edge of North America (Figure 2.3). Several hundred meters of shallow water marine sediment accumulated in the subsiding western part. In the eastern part, there are similar sedimentary strata, but they are just a tenth as thick as the western part (Hintze, 1988). Most Precambrian and lower Cambrian units consists of quartzitic sandstones, siltstones and mudstones, whereas middle Cambrian to Devonian units is made up of limestone and dolomite carbonate deposition with records of sea level fluctuations (Hintze, 1988; UGS, n.d.).

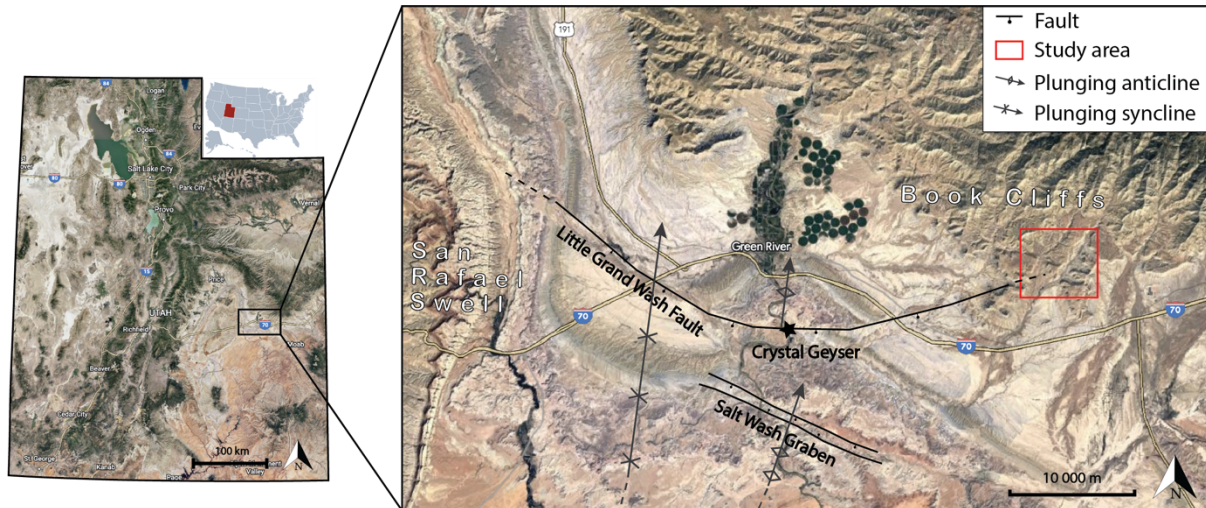


Figure 2.1 – Map of Utah (USA) with closer section of the region around the study area Floy Canyon (red box), including structural elements and names. Insert shows USA and the location of Utah state. The maps are modified from Google Earth and 50states.com. Fault zones structures are compiled from Heath et al., (2009) and Ogata (2014).

From Late Triassic to Early Jurassic, there was a south-eastward uplift, where Utah was located at the northwest end of the chain of the linked basin and uplifts called “Ancestral Rockies”. Isolated basins accumulated hundreds of meters of evaporites such as the Paradox Basin in South East Utah, where salt structures can be observed (Figure 2.1) (Hintze, 1988; UGS, n.d.). The end of the Triassic was also the start of the development of the Cordilleran magmatic arc along the western margin of the North American plate as a response to the subduction of the western Pacific oceanic plate (DeCelles & Coogan, 2006). Rising mountains to the west also ascribe to desert environments in most of Utah, causing the formation of aeolian dunes from siliceous sand brought in from the north (Hintze, 1988; UGS, n.d.). This predominately aeolian depositional system in eastern Utah is represented by the Triassic to Lower Jurassic Moenkopi, Chinle, Wingate, Kayenta, and Navajo sandstone-dominated formations (Figure 2.2; Martz et al., 2017; Zuchuat et al., 2018, 2019). Marine incursions from the north initiated a transitional aeolian-shallow marine environment platform, best expressed in the Carmel, Entrada, Curtis, and Summerville formations (Figure 2.2). In the late Jurassic period, Utah’s climate became wetter, allowing for the development of meandering rivers and lakes (Hintze, 1988; UGS, n.d.). As the western oceanic plate was subducted beneath the west coast of North America, the Cordilleran thrust system was active east of the Cordilleran magmatic arc in the Late Jurassic time. It resulted in thrusts breaking toward the surface, including granitic intrusions in western Utah (DeCelles & Coogan, 2006; Hintze, 1988).

In the late Cretaceous (101-66 m.y. ago), the Sevier Orogeny, an eastern thrust-tectonic segment of the frontal part of the Cordilleran fold-and-thrust belt, formed which spans from Alaska to Mexico (Hintze, 1988; DeCelles & Coogan, 2006; UGS, n.d.). This led to the rising mountains of western Utah. Compressional tectonics prevailed, with eastward propagating, piggyback style thrusts and little basement involvement in Utah. The Sevier Orogeny led to lithospheric flexure to the east and development of the Cordilleran foreland-basin system (Currie, 1997; Currie, 2002). An inland sea covered the eastern part of Utah with a NE-SW shoreline from the Gulf of Mexico to the Arctic. The Upper Cretaceous Mesaverde Group in Central Utah forms a thick coastal prism of numerous progradational deltaic tongues fed from the rising Sevier fold-thrust belt (Wills & Gabel, 2001; Davies et al., 2006; see also Hintze, 1988; Currie, 1997; UGS, n.d.).

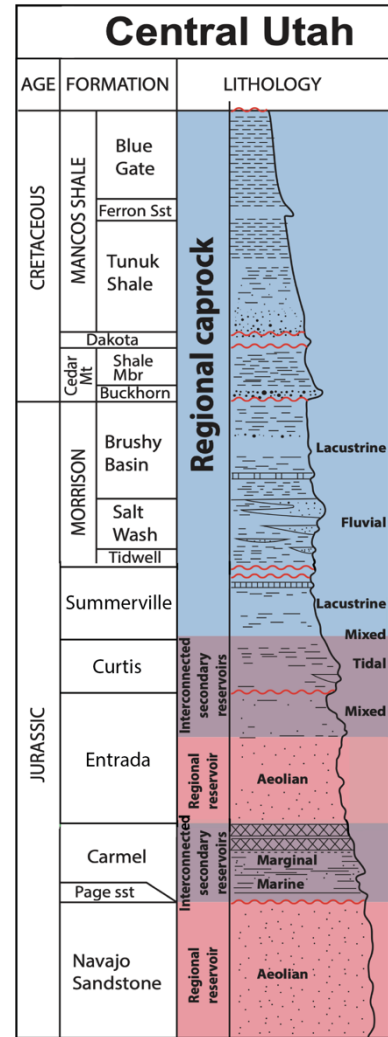


Figure 2.2 – Stratigraphic column of Central Utah. Modified from Zuchuat et al. (2018).

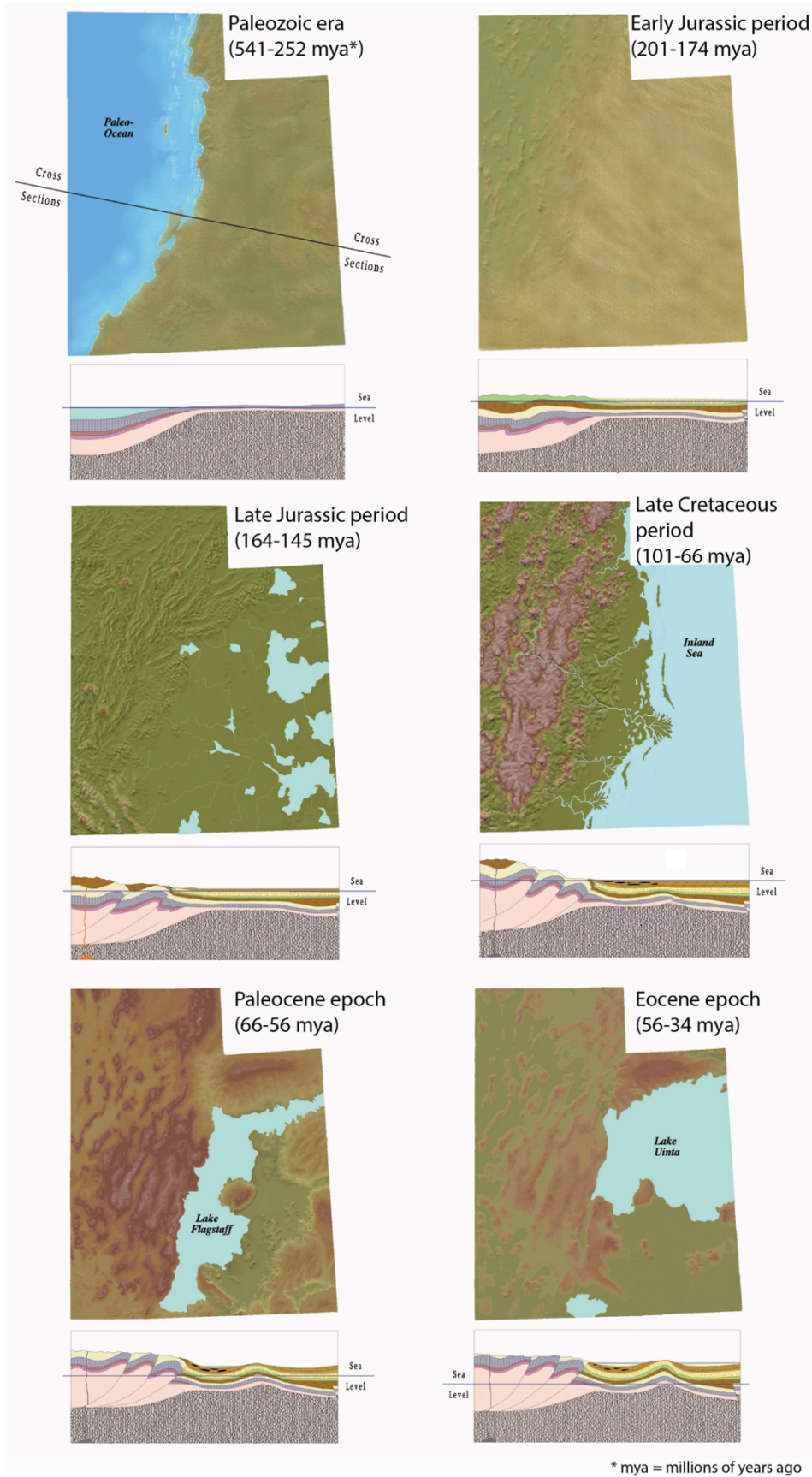


Figure 2.3 – Paleogeography of Utah from Paleozoic to Eocene times. Figure modified from UGS (n.d.); geology.utah.gov

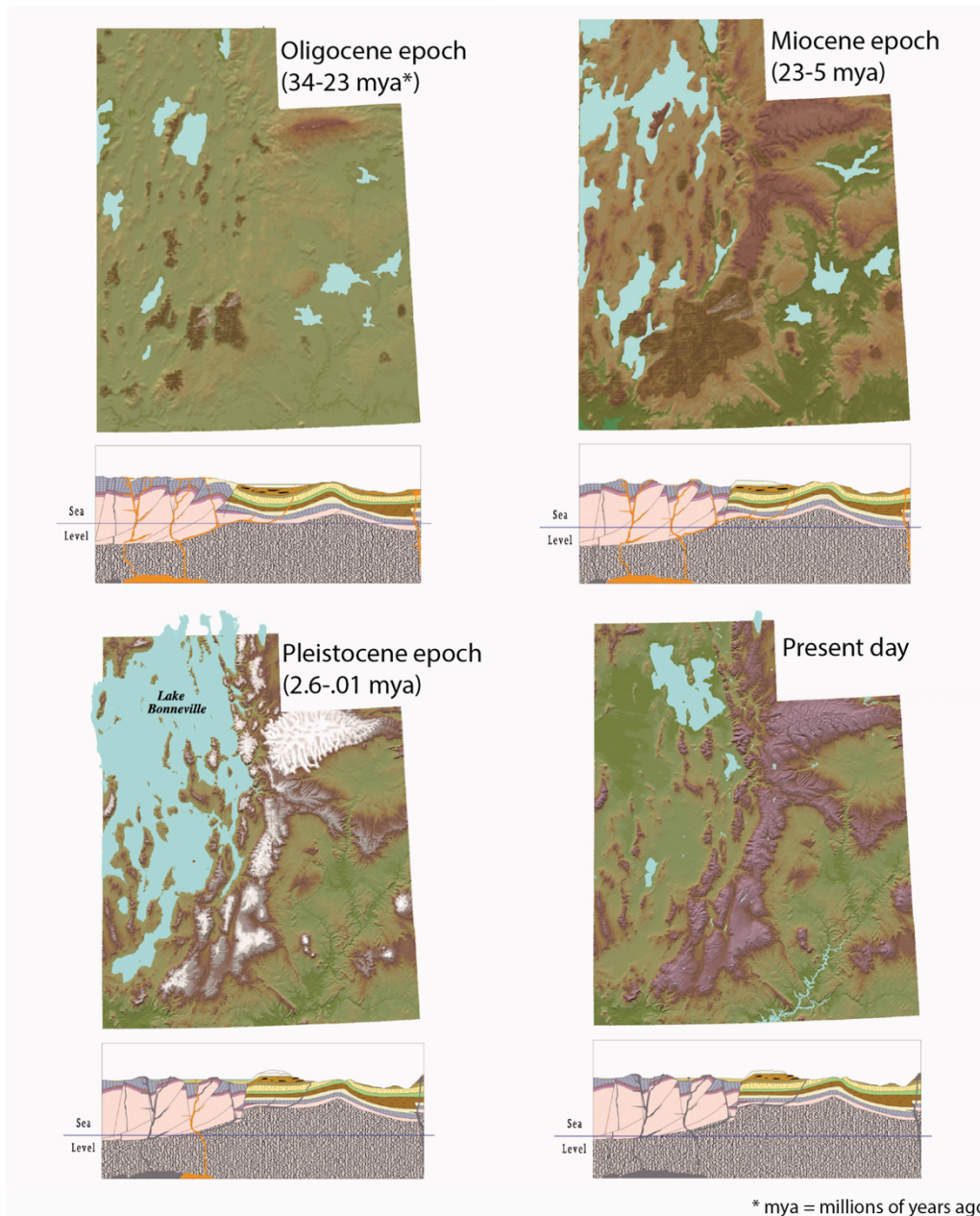


Figure 2.4 - Paleogeography of Utah from Oligocene to present day. Figure modified from UGS (n.d.); geology.utah.gov

In the Paleocene to Eocene epochs (66-34 mya), erosion of the mountains to the west supplied a wave of sediments eastward (Hintze, 1988; UGS, n.d.). At the same time, the Laramide orogeny initiated with a reverse fault driving basement-cored uplift. This uplift was caused from the continued pressure from the Pacific Plate affecting the Colorado Plateau province and the mountains (Davis, 1978; Dickinson et al., 1988; Hintze, 1988; Bump & Davis, 2003; Davis & Bump, 2009). The Laramide deformation involved the whole crust, including the basement, which resulted in buckling and shears; monoclinical flexures such as the San Rafael Swell on the

Colorado Plateau. The uplift is also linked to the downwarping of the synclinal Uinta Basin, caused by the tectonic loading from the basement involved uplift. The lacustrine Uinta Basin accumulated organic-rich sediments, which turned into prolific oil and gas source rocks (Davis, 1978; Dickinson et al., 1988; Hintze, 1988; Bump & Davis, 2003; Davis & Bump, 2009; UGS, n.d.).

During the Oligocene and Miocene epochs (34-5 mya), uplift and the “ignimbrite flare-up”, a major post-Laramide igneous activity of mantle origin, occurred in northwestern Utah and spread southwards, affecting almost all parts except the Uinta Basin (Humphreys, 1995; Hintze, 1988). Figure 2.4 shows the paleogeography of this period. It is proposed that the magmatic flare-up and uplift are ascribed to the removal of the sub horizontally subducting Oceanic slab, also called the Farallon Slab (Humphreys, 1995). The removal of the oceanic slab adjacent to the continental lithosphere subsequently led to the rising of the underlying asthenosphere, and the mantle getting heated (Garzanti, 2018). Regional uplift in the Miocene rejuvenated major river systems in the Rocky Mountains and the Colorado Plateau, filling the newly created basins by lakes, and modern-day rivers started to develop (e.g. Green River), which carved the canyonlands we observe today (Hintze, 1988; UGS, n.d.). Continental extension also occurred in western Utah, preceding volcanism related to the Farallon Slab detachment and flare-up by 2 Ma. Consequently, led to the breaking up of western Utah into the north-south Basin and Ranges provinces, which also filled up the adjacent basins (Hintze, 1988; Putirka & Platt, 2012; UGS, n.d.). Putirka & Platt (2012) discuss if the Basin and Range volcanism is a passive response to extensional tectonics. From 2.6 mya to the present, the geography of Utah resembles much of what we have today. There was more carving of canyons because of the wetter and colder climate in 2.6-0.1 Mya (Hintze, 1988; UGS, n.d.).

2.1.2 Structures and stratigraphic column of Upper Cretaceous Floy Canyon

In this subchapter, I will describe the sedimentary successions regionally within Utah and locally within the study area in Floy Canyon, eastern Utah (Figure 2.1). The Floy Canyon contains exposed clastic depositional units in the Book Cliffs from the Late Cretaceous, the Blackhawk Formation and interfingering Mancos shale, both part of the Mesaverde Group, shown in Figure 2.5 (Chan et al., 1991).

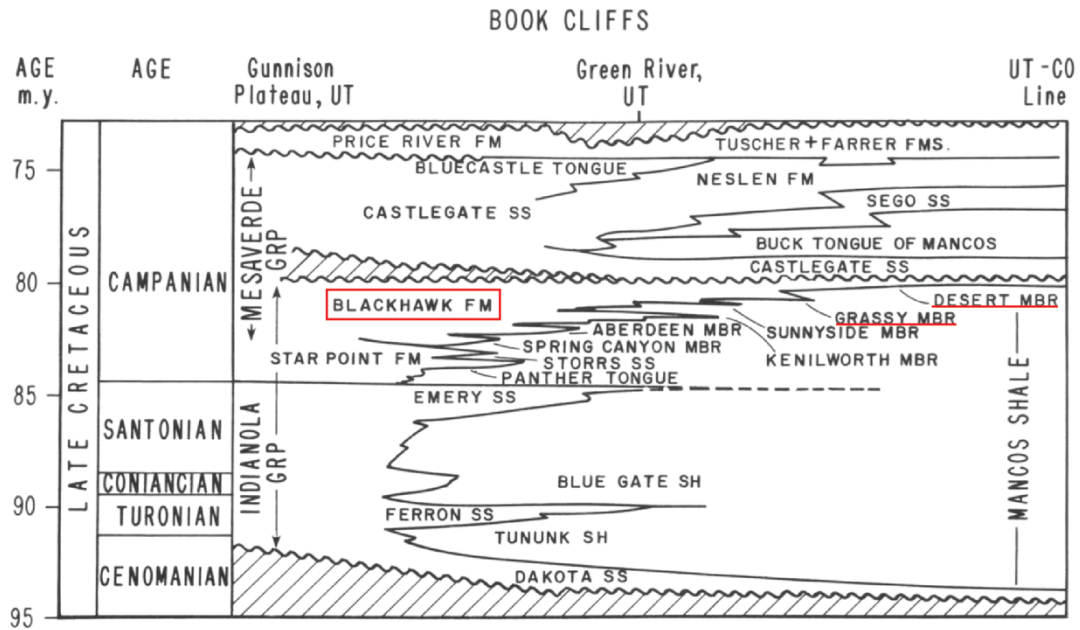


Figure 2.5 – Simplified cross-section of stratigraphic units. Blackhawk Formation, Grassy and Desert members are marked with red. Figure modified from Chan et al. (1991).

Regional geology – Book Cliffs in general

As previously mentioned, in Cretaceous times, the Sevier fold-thrust belt propagated eastward, setting up thin-skinned deformation, crustal thickening and the isostatically forced foredeep basin in Central-East Utah (Davies et al., 2006; DeCelles & Coogan, 2006). This basin was occupied by an inland sea, along the edge of which the successions of the Book Cliffs area were deposited (Chan et al., 1991; Hampson & Howell, 2005; Davies et al., 2006). The Upper Cretaceous succession in the Book Cliffs area consists of stacked coastal plain and nearshore deposits recording the repeated progradation and retrogradation of river and wave-dominated deltas (Blackhawk Formation) into the marine basin (Mancos Shale) (Chan et al., 1991; O’Byrne & Flint, 1996; Hampson & Howell, 2005; Davies et al., 2006). Figure 2.5 shows a stratigraphic cross-section from Utah to Colorado (W-E) and displays the entire length of onshore to the offshore inland sea, intertonguing between the Mancos Shale and the Mesaverde Group (Hettinger & Kirschbaum, 2002; Chan et al., 1991). The Mancos shale is a widespread unit found in western Colorado, northwestern New Mexico, northeastern Arizona and eastern Utah (Cross, 1899; Young, 1955, as cited in Chan et al., 1991). The Blackhawk Formation consists of six lithostratigraphic members in ascending order: Spring Canyon, Aberdeen, Kenilworth, Sunnyside, Grassy and Desert; each of which record major eastward coastal progradation (Chan et al., 1991; Davies et al., 2006).

Local geology – Floy canyon in detail

The Upper Cretaceous stratigraphy of the Blackhawk Formation and Mancos Shale are described as intertonguing sandstone and shale (Chan et al., 1991). Mancos Shale displays dark grey to steel-blue colouring, and the accumulation environment was an offshore, open marine (Hettinger & Kirschbaum, 2002; Chan et al., 1991). The climate during the deposition was warm to sub-tropical (Balsley, 1982, cited in Chan et al., 1991). Stacked strand-plain packages are common in the Blackhawk Formation, with coal seams accumulated in coastal-plain and lagoonal-swamp environments (Chan et al., 1991; Davies et al., 2006). According to the article by Chan et al. (1991), Floy Canyon represents the upper Blackhawk Formation, either the Grassy or Desert member (Figure 2.5).

Both the Campanian (84-72 Ma) Grassy and Desert members are prominent coarsening upward sequences (Chan et al., 1991; O'Byrne & Flint, 1996). Both contain siltstone, and fine to very fine sandstone interbedded with organic-rich or silty shale in the lower part (Chan et al., 1991). Sedimentary structures such as cross-stratification, ripples and bioturbation are abundant in the middle part of both members, and both contain light/white fine to medium-grained sandstone, also referred to as whitecap sandstone. The upper Grassy member consists of coarser sandstone and 2,8 m thick bituminous coal. The upper portion of the Desert member consists of thin coals and channel-fills sandstone with trough stratification beneath the Castlegate sandstone (Chan et al., 1991).

The Grassy and Desert members are offset by several NE-SW trending normal faults, the timing of which is poorly understood (Figure 5.1 in Chapter 5). The faults could stem from deformation during the latest Cretaceous to early Cenozoic Post- Laramide Orogeny and the uplift of the Colorado Plateau (Kauffman, 1977 and Stokes, 1986, as cited in Chan et al., 1991). Hecker (1993, as cited in Shipton et al. 2004) reported Quaternary fault-activity along the Salt Wash fault (Figure 2.1) in the local area south of Green River. The Little Grand Wash fault north of the Salt wash fault (Figure 2.1) cuts the north plunging anticline, which can be related to salt movement from the Paradox basin formations (Shipton et al., 2004). Another explanation of how the faults in Floy Canyon were formed, is from observations on syn-depositional faulting indicators in the study area (Braathen & Midtkandal, pers. comm., 2022). Synsedimentary normal faults, also named growth fault, is associated with deltas and are activation of faults during sedimentation and typically display thicker strata on the downthrown side of the hanging wall (Bhattacharya & Davies, 2004; Braathen et al. 2018).

2.2 Geologic setting of the northern North Sea

The study area is, as mentioned, within the Aurora CO₂ storage site with its targeted formations for the CO₂ injection in the Horda Platform, northern North Sea. The regional geology of the northern North Sea will be summarized in two parts; the structural framework (sub-chapter 2.2.1), and the geological history (sub-chapter 2.2.2), which emphasizes the tectonic history and the stratigraphical column of the target formations within the study area.

2.2.1 Structural framework

The North Sea is located on the Norwegian Continental Shelf (NCS), connected with the Norwegian Sea in the north and lies between Norway, Denmark, and Great Britain, (Figure 2.6A). The North Sea is an Intracratonic basin, which means that it is underlain by continental crust (Faleide, 2010). The North Sea Basin consists of several structural elements formed during successive rifting events from the Devonian to Jurassic, of which the Late Jurassic Viking Graben and flanking East Shetland and Horda platforms are the most important elements in the northern North Sea (Figure 2.6B). The Horda Platform is an N-S trending, 300 km long structural high located on the eastern side of the Viking Graben, bounded by N-S striking thick-skinned (basement involved) normal faults with 3-5 km displacement (Whipp et al., 2014; see also Færseth, 1996). This structural high is bounded to the east by the Øygarden Fault Complex, which marks a sharp transition in thickness of the crust (Figure 2.6C; Sellevoll, 1973; Hospers & Ediriweera, 1991 as cited in Færseth et al., 1995). The Horda Platform is made up of half grabens (the Vette-, Tusse-, Svartalv-, and Troll fault blocks) that are tilted and rotated to the east (Figure 2.6C; Whipp et al., 2014; Færseth, 1996). These half grabens contain approximately 3 km of Permo-Triassic syn-rift strata (some contain even older Devonian strata), overlain by 1 km Triassic to Middle Jurassic post-rift strata, and again overlain by less than 500 m Late Jurassic to Early Cretaceous syn-rift strata (Figure 2.6C; Whipp et al., 2014). The N-S striking thick-skinned rotated fault blocks are ca. 2 km high, have 1.5 km of throw (vertical displacement) and are over 60 km long (Whipp et al., 2014). The Horda platform also consists of a smaller population of predominately NW-SE-striking normal faults, which are more closely spaced (<5km), offer less than 100 m throw and are less than 10 km long, as shown in figure 4.1 in chapter 4 (Whipp et al., 2014). These faults are mainly restricted to the Late Jurassic to Cretaceous succession and are thin-skinned (not basement-involved faults).

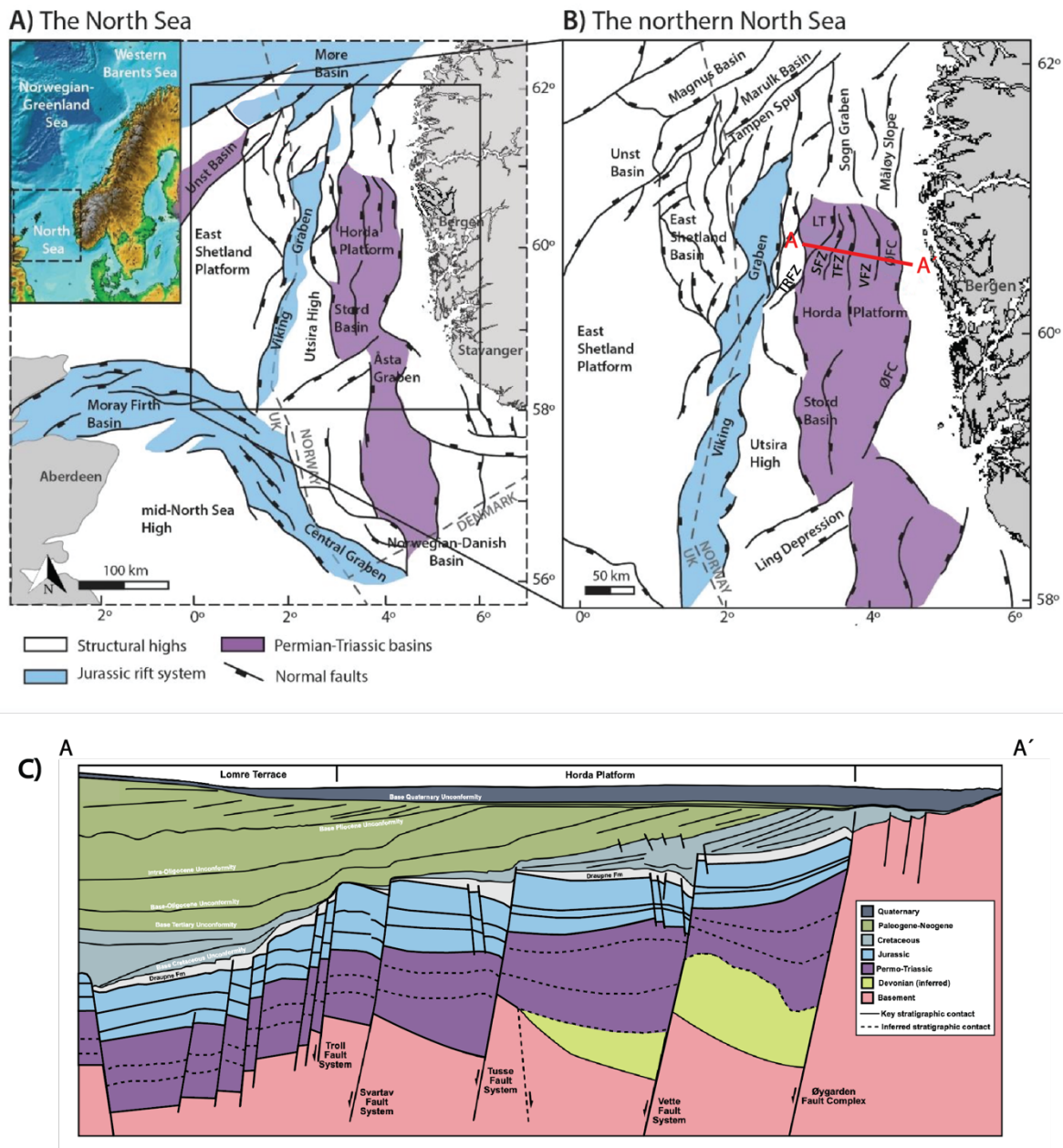


Figure 2.6 – (A) and (B) are maps of the North Sea, which show the structural elements, modified from Holden (2021). (A) The insert overview photo to the left corner shows the map's location in the Norwegian Continental Shelf (NCS). The map shows the North Sea and the location of section (B). (B) Section showing the northern North Sea. Crossline A-A' is displayed in (C). (C) Simplified Cross-section across the Horda Platform. Figure modified from Whipp et al. (2014). Abbreviations: LT = Lomre Terrace, TRFZ = Troll Fault Zone, SFZ = Svartlv Fault Zone, TFZ = Tusse Fault Zone, VFZ = Vette Fault Zone, ØFC = Øygarden Fault Complex.

2.2.2 Geological history of northern North Sea

The northern North Sea's geological development of Late Permian to Quaternary periods covers several rift stages with associated pre-, syn- and post-rift depositional patterns, Figure 2.7 gives an overview of the stratigraphy in the Horda Platform and the tectonic phases.

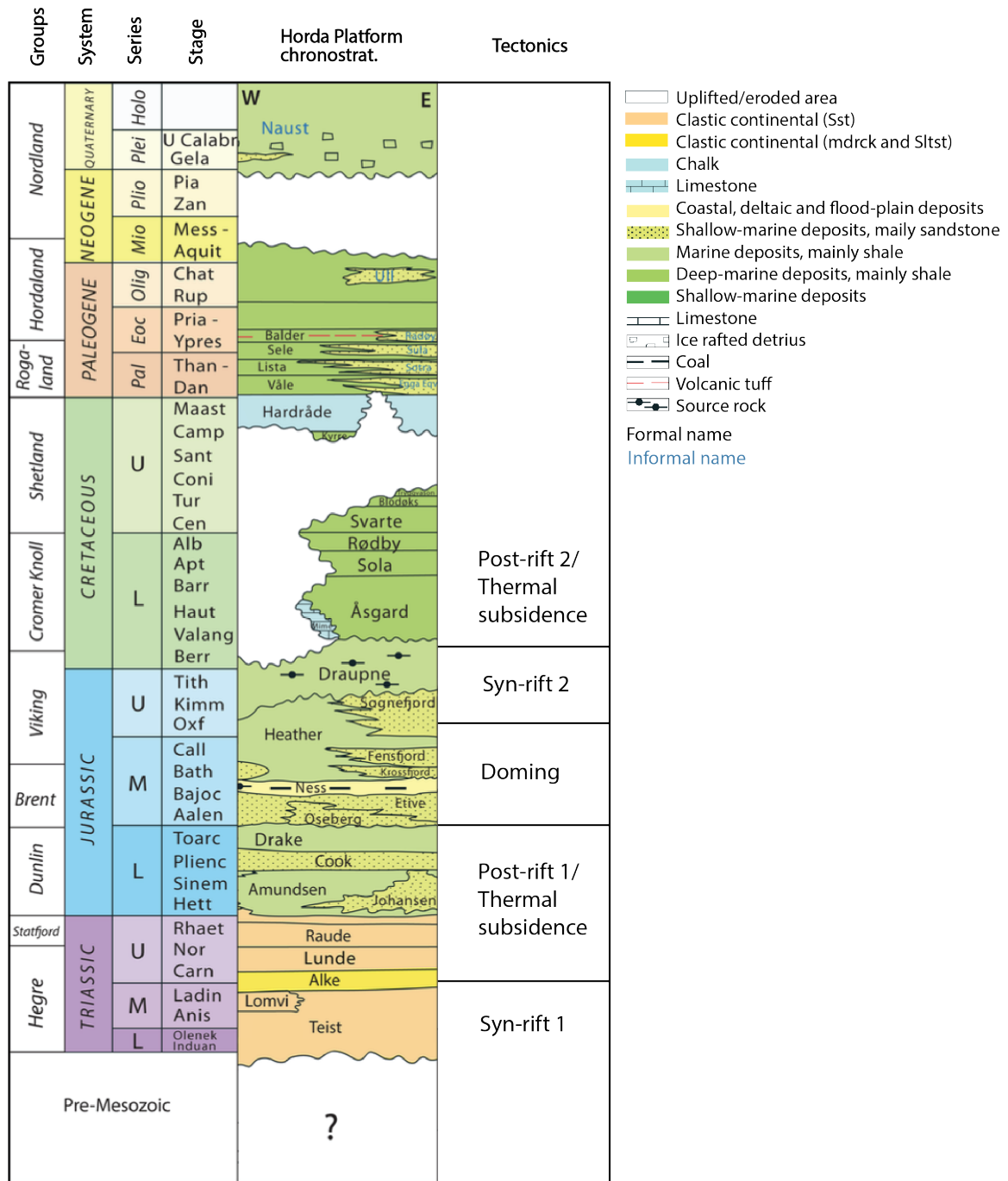


Figure 2.7 – Stratigraphic chart of Triassic to Quaternary deposits in the Horda Platform. Modified from NPD (2014). The timing of tectonic events is compiled from Færseth (1996), Odinsen et al. (2000a, b), Bell et al. (2014), Duffy et al. (2015), Wrona et al. (2017) cited in Mulrooney (2020).

Pre- Permian

Crystalline basement of metamorphic and magmatic rocks was rejuvenated and generated and emplaced into a stack of thrust sheets during the Caledonian orogeny, which culminated in the Ordovician. Subsequent extensional collapse of the Caledonides took place in Carboniferous to

Devonian times with formation of supradetachment rift basins filled with coarse clastic intracontinental clastics (Ziegler, 1975; Faleide et al., 2010; Fazlikhani et al., 2017).

Permian to early Triassic

In the early Permian, localized extensional faulting-initiated formation of sedimentary basins, is first seen in the southern North Sea (Faleide et al., 2010; Phillips et al., 2019). This was the onset of the so-called Rift phase 1. Extensional movements continued and became more widespread, with inter-connected strike-slip and extensional faults impacting most of the North Sea realm. Rifting continued into the earliest Triassic time (Figure 2.7), representing the tail of Rift-phase 1.

During Phase 1, faults contributed to E-W extension. Larger faults were basement involved, W-dipping, and N-S striking faults, such as the faults in Horda platform; Øygarden Fault Complex, Vette Fault Zone, Tusse Fault Zone, and Svartalv Fault Zone (Færseth, 1996). This rifting stage also led to fault-block rotation, the creation of accommodation space in the hanging walls, and erosion of the uplifted footwalls (Færseth, 1996; Phillips et al., 2019). The accommodation space in the hanging walls filled up with up to 3 km of wedge-shaped, syn-rift sediments.

Middle Triassic to Early Jurassic

During late Triassic to Middle Jurassic development, large clastic wedges were shed from the Norwegian and East Shetland hinterlands, filling the post-rift basin – this is the post-rift 1 stage, as shown in Figure 2.7 (Steel, 1993; Faleide et al., 2010). Different rates of thermal subsidence took place throughout the Triassic time, driving mild rejuvenation of some faults. For instance, the Øygarden Fault Zone appears to have been active along the eastern margin of the Permo-Triassic basin. The sedimentation rate was sufficient to keep up with the subsidence in the Horda Platform, resulting in a flat continental landscape with clastic input from flowing rivers (Deegan and Scull, 1977; Faleide et al., 2010). Near the end of the Triassic, a semi-arid continental climate gave way to gradually more humid conditions, under which the Statfjord Formation was deposited. Subsequently, in the Early Jurassic, the Dunlin Group present humid tropical conditions and marginal marine depositional environments in the northern North Sea (Deegan and Scull, 1977; Faleide et al., 2010).

The Lower Jurassic Dunlin Group, from base to top, consists of the Amundsen, Johansen, Cook, and Drake formations (Marjanac & Steel, 1997). The Johansen and Cook formations are targeted aquifers for CO₂ injection in the Aurora site. The Amundsen Formation comprises dark marine shales that, in middle parts, interfingers with the sandier Johansen Formation. Accordingly, the Amundsen Formation subdivides into two sub-groups; Upper and Lower Amundsen. The Johansen Formation represents a large sandstone body representing deltas which prograded towards the west and north (Vollset and Doré, 1984; Marjanac & Steel, 1997; Sundal et al., 2016). Clinoform geometries restricted on topographic lows developed at the base level of the Dunlin Group, were observable on seismic data suggesting deposition during a fall in sea level (Marjanac & Steel, 1997). Notably, this formation is restricted to the Horda Platform. The Johansen Formation comprises fine-grained sandstone and siltstone belts, making up a maximum thickness of 160 meters (Marjanac & Steel, 1997).

The Cook Formation overlies the Johansen Formation in the Horda Platform. It consists of four sandstone tongues (Marjanac & Steel, 1997). The pattern of each tongue comprises, from bottom to top, interbedded sandstones and shales, referred to as the heterolithic facies, and an upper clean sandstone unit called the Cook sandstone. The lower heterolithic facies are interpreted as lower shoreface deposits of a progradational marginal-marine system during falling sea level. Noticeably, the lower unit of the heterolithic facies is strongly bioturbated with bio-activity diminishing upwards in an coarsening package (Marjanac & Steel, 1997; Vollset and Doré, 1984). The heterolithic facies is truncated by the clean Cook sandstone, which is interpreted as tide-dominated deltaic to outer estuarine deposition environments (Marjanac & Steel, 1997).

The Drake Formation, which overlies the Cook Formation, where the lower section predominantly consists of laminated shale and silty shale deposited in an offshore marine environment (Marjanac & Steel, 1997). Of significance is that the Lower Drake Formation represents a seal within an overall sandstone dominated succession, which will act as a flow-barrier (primary top-seal) for CO₂ injection in underlying units of the Aurora site.

Middle Jurassic to Cretaceous

Above the Dunlin Group, another succession ascribed to prograding delta sequences make up the Brent Group. Both units were deposited during tectonic quiescence, prior to Rift-phase 2 (see below). The Brent Group is sourced from regions of domal uplift in the Central North Sea

in Middle Jurassic times, where the deltaic successions prograded northward in the Viking Graben (Figure 2.7; Ziegler, 1975; Underhill & Partington, 1993). Models predict that volcanic activity links to mantle-related up-welling and related warming of a large dome (Torsvik et al., 2002). In Middle to Late Jurassic times, the dome collapsed, triggering gradual subsidence, and marine conditions recurred (Torsvik et al., 2002). Timewise, the transition from the upper Brent Group to the overlying Viking Group coincides with collapse of the dome and the start of a new rift phase, Rift-phase 2. The progradational systems of the Viking Group – i.e the Krossfjord, Fensfjord and Sognefjord systems, are all sourced from the from the Norwegian mainland and build out across the northern Horda Platform during increasing rifting in the middle-Late Jurassic (Vollset and Doré, 1984; Steel, 1993). In the late Jurassic, volcanism perished, and along with the Rift-phase 2 created large-scale normal faults in response to crustal extension in the northern North Sea, as shown in Figure 2.7 (Ziegler, 1975; Ravnås & Steel, 1997; Faleide et al., 2010; Davies et al., 2001). During this event, sediment supply was outpaced by basin subsidence, which led to the drowning of the Progradational systems of the Viking Graben (Faleide et al., 2010), leading to regional-scale deep marine deposits of the Draupne Shale. Extension in Rift Phase 2 mainly affected the Viking Graben area less so the Horda Platform. Faults formed in Rift Phase 1 was reactivated with overall minor subsidence, and a new population of smaller faults striking in N-S and NW-SE formed. These smaller faults abut or cross-cut the larger, Rift Phase 1 faults (Færseth, 1996; Whipp et al., 2014). Subsidence and sea-level rise during the Cretaceous led to the accumulation of deep-water mudstones, marls and calcareous shales of the Cromer Knoll Group, as observed on the surrounding platforms (Brekke et al., 2001). The Cromer Knoll Group is of economic significance, as it acts as a proven top-seal along crests of footwall fault-blocks where Draupne Formation is missing, as for instance observed in the Troll East Field. In Early Cretaceous times most faults activity ceased, where the post-rift transition was highly diachronous (Faleide et al., 2010).

In the Early Cretaceous, different degrees of subsidence in the post-rift stage 2 was caused by thermal cooling after the Jurassic rifting (Gabrielsen et al., 2001; Faleide et al., 2010). The sediment supply outpaced or balanced the subsidence, as seen by shallow to deep marine sediments of the upper parts of the Cromer Knoll Formation (Figure 2.7; Brekke et al., 2001). In the Late Cretaceous, the sea reached its transgressive maximum, where no clastic sediments were deposited across a large area of northwestern Europe, and deep marine calcareous shales dominated (Faleide et al., 2010).

Cenozoic

Rifting, breakup and initiation of seafloor spreading in the NE Atlantic during the early Cenozoic led to tectonic uplift in the east and west of the North Sea, creating depocenters close to the basin margins. Uplifts fed prograding clastic wedges. Of these wedges, the prograding sandstone package in the Horda Platform are most likely sourced from mainland Norway (Faleide et al., 2002). Southern Norway experienced uplift in the Eocene to Oligocene, countered by marine deposition in the northern North Sea. This phase continued until Miocene, ending with a hiatus across the northern North Sea (Faleide et al., 2010). The last uplift occurred in the Plio-Pleistocene time, where extensive glacial erosion led to isostatic uplift events (Faleide et al., 2002).

3 Theoretical framework

Faults are three-dimensional intricate zones composed of linked fault segments (e.g., Walsh and Watterson, 1988; Walsh et al. 1991, Childs et al. 2009; Braathen et al. 2009; Fossen and Rotevatn 2016). Within fault zones, most of the strain is localized in a fault core, which is surrounded by a much wider damage zone of discrete structures and subsidiary faults. Nearly all displacement on the fault is absorbed in the core (Braathen et al. 2009). Understanding fault architecture is highly relevant to the smaller-scaled F1 fault in the Aurora storage site, which will be the first fault the CO₂ encounters during plume migration when injection starts in 2024. Faults represent baffles or seals, and less frequently pathways, for fluid migration. Accordingly, there has been a focus on the importance of the structure and the fluid flow properties (e.g., porosity, permeability, and capillary properties) of reservoir to seal scale faults (e.g. Knipe, 1997; Knipe et al., 1997; Fisher & Knipe, 1998). This chapter presents an insight into the theory behind fault zone architecture, fault development and the influence of faults on CO₂ fluid migration. Of relevance is the limitations in seismic resolution which controls what we can and cannot observe in the fault zone. This section outlines fundamental understanding that are required to fully comprehend results of the presented study: there are benefits and limitations when comparing outcrop observations with seismic reflection data.

3.1 Fault zone architecture of normal faults

Even though fault zones occupy small portions of the crust, they have a significant influence on the crust’s mechanics and fluid flow properties (Faulkner et al., 2010; Miocic et al., 2019). Faults can be classified hierarchically, where a fault system can be separated into individual faults. Each fault carries a strain envelope which holds information on the volume (length, width, height), shape (planar, listric, ramp-flat-ramp), and the zonation and structures within (Braathen et al., 2009). This hierarchical order is shown in Figure 3.1.

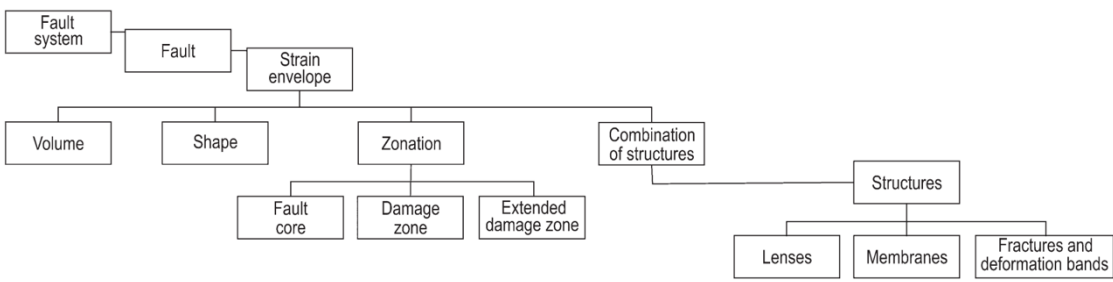


Figure 3.1 – Fault-facies hierarchical classification scheme. Fault system contains several faults, each with its geometry, size (length, width, height), and sense of slip (normal, reverse, strike-slip). The fault contains zonation, where structures can be classified within. Figure from Braathen et al., 2009.

The fault architecture and geometry vary depending on the scale we are working on. In seismic fault interpretation, limits in seismic resolution restricts us from observing structures that are smaller than the seismic detection level. Therefore, interpretation of faults in seismic results in more simplified fault structures (Færseth et al., 2007; Bond, 2015; Faleide et al., 2021). This can potentially jeopardize or lead to less accurate results when calculating the sealing capacity of a given fault. Figure 3.2 exemplifies of how a fault will be interpreted in seismic data versus how the fault is seen in nature.

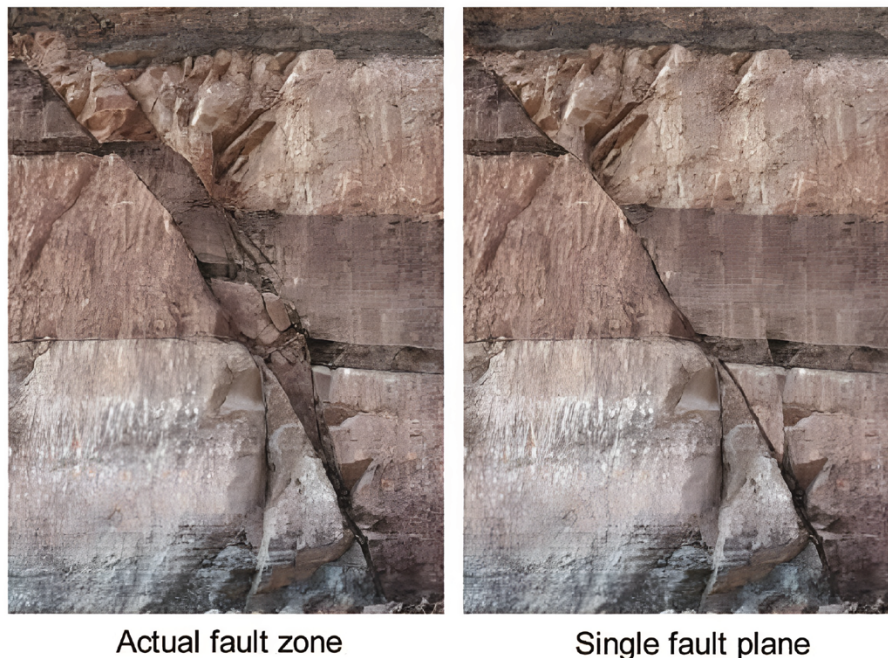


Figure 3.2 – Picture to the left is taken from Arches National Park in Utah. Picture to the right is the photoshopped version, representing the standard seismic interpretation of a single fault plane. Figure is enhanced by Botter (2016).

In seismic fault interpretation, the faults are conveyed as a single continuous surface, while realistically, faults contain several slip planes (Færseth et al., 2007). This deviation in description of the fault is brought across to forecasts of fault-sealing capabilities, see section 3.3. A fault can be sealing or non-sealing in CO₂ storage formations (Miocic et al., 2019). Fault sealing depends on the rock stratigraphy, intrinsic structure and composition, and the mechanics behind the fault strain.

3.1.1 Across – fault seals

The fault strike's length and orientation can significantly affect fluid migration (Miocic et al., 2019). For instance, the longer the fault is, the more fluid migration will be impacted, potentially slowing down the migration rate by increasing the distance. When buoyant CO_2 is injected into the storage unit, it naturally seeks upwards until it encounters a sealing caprock or fault. Then the CO_2 will build up close to the flow barrier, such as the fault plane, until the pressure exceeds the pressure for capillary breakthrough, leading to fluid migration. Less commonly, pressure build-up exceeds rock strength and then induces fracturing (Schowalter, 1979; Miocic et al., 2019) that allow fluids to migrate across the seal. This will be further explained in section 3.3.2.

Figure 3.3 shows various scenarios for fault impact on a CO_2 plume: sealing, across-fault migration, and leakage. Figure 3.3a displays an impermeable cap rock unit juxtaposed on the CO_2 storage, creating a seal, but also shows sand-on-sand juxtaposition underneath, which allows for across-fault migration. Figure 3.3b shows that the fault is inherently sealing. In contrast, Figure 3.3c shows a similar sealing part of the fault as in Figure 3.3b, but also displays fault-parallel seep through fracture networks, which may be caused by

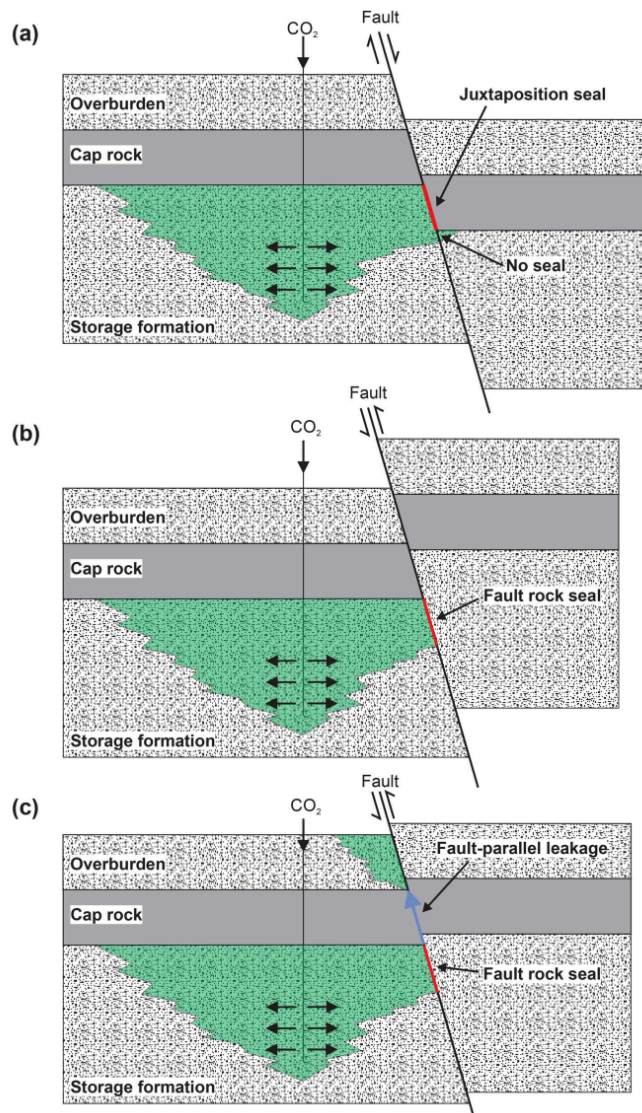


Figure 3.3 – Three different cross-fault seals and cross-fault fluid migration scenarios. (a) Juxtaposition seal with across fluid migration where it is self-juxtaposition; no up-dip leakage. (b) Fault rock sealing in self-juxtaposition; membrane seal. (c) Membrane seal in self-juxtaposition, including up-dip leakage in the fault. Figure from Miocic et al. (2019).

overpressure-induced fracturing (Miocic et al., 2019) or fluid mobility in fractured fault core and/or damage zones.

3.1.2 Fault Facies classification

Previous studies have considered the structures of brittle fault rocks as chaotic, but recent detailed observations show they are highly structured (Braathen et al., 2009; Faulkner et al., 2010). Fault facies is related to physical field data, where geologist can classify any features in a fault derived from tectonic deformation. Fault facies appears in certain combinations and occurs in certain zonations (Braathen et al., 2009). As previously mentioned, the strain envelope of the fault is divided into core and damage zone, as shown in Figure 3.4. Typically, the fault envelope exhibits fault-parallel zonation, and the structural elements within are classified into three main groups: discrete structures, membranes and lenses (Braathen et al., 2009).

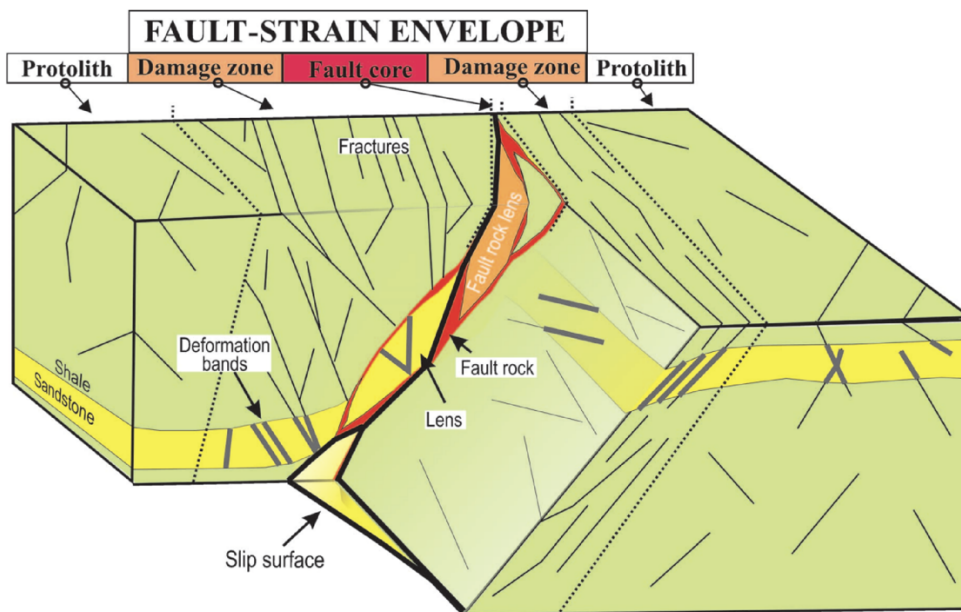


Figure 3.4 – Illustrative figure of the structural elements and zonation of a normal fault in a siliciclastic rock. Figure from Braathen et al. (2009).

Discrete structures

Discrete structures are described as sharp discontinuities without cohesion during development (Schultz & Fossen, 2008; Braathen et al., 2009). These are the slip surfaces and fractures (Figure 3.4). Deformation bands are mm-wide tabular shear zones in which sand-grains are reorganized and/or broken into a fine-grained rock-mass (Braathen et al., 2009). All slip surfaces offer shear movement and, and larger fault (> c. 10 m; Braathen pers. comm.) exhibit a principal slip surface. Slip surfaces experience significantly more slip/movement than other fractures in the fault zone, and in many cases damage wall-rocks into mm-wide very fine-grained membranes of crushed material. Besides, slip surfaces are sub-parallel to the fault and exclusively occur within the fault core (Braathen et al., 2009).

Fractures are strain localization structures that can occur in the fault core and damage zone area (Schultz & Fossen, 2008; Fossen, 2016). Fractures can form by opening or shearing: joints accommodate dilation without shear movement, whereas shear fractures accommodate shear movements. Fractures in the damage zone increase permeability compared to the host rock (Miocic et al., 2019). It is worth elaborating that a slip surface is, by definition, a type of shear fracture. However, to make it less confusing, we restrict the term slip surface to planar structures with offset on meter-scale or larger, which are parallel to the sense of fault movement (Schultz & Fossen, 2008; Fossen, 2016). Figure 3.4 shows fractures placed in the damage zone in different orientations, while the slip surface is in the fault core between the displaced footwall block and the hanging-wall block.

Highly porous rocks such as sandstone usually form deformation bands instead of fractures, as reviewed in Fossen et al. (2017) (see also Braathen et al., 2020 for description of band and fracture combinations). Deformation bands differ from fractures, as their formation require at least 12-15% porosity. Bands are long (10-100 m) in out-going but in many cases are bound to layers of given thickness. Individual bands appear as thin (<1 cm) tabular zones. Kinematically, they divide into dilation (less common) or compaction bands, without or with various degrees of shear on mm-cm scale. Band formation will in most cases cause porosity loss and permeability reduction, by reorganization and fragmentation of sand grains during deformation. They are commonly encountered in fault damage zones of porous sandstones, where they appear in populations making up various types of band swarms.

Membranes

Membranes sit along the fault core, with typical membranes named breccias, gouges or smears, shown in Figure 3.5a (Braathen et al., 2009). Breccias and gouges generate from the comminution of rocks, while smears are formed by ductile rotation of the layer (Woodcock & Mort, 2008; Braathen et al., 2009). We typically find gouges and smears along slip surfaces, and we classify them if these are continuous or not (Figure 3.5b). Gouges are primarily incohesive very fine-grained fault rocks and can be millimeters to centimeters thick. There has been some confusion with the definition of breccias, and according to the revised breccia classification article from Woodcock & Mort (2008), breccias are better off being defined by their coarse grain size than their incohesive-ness during faulting. Breccias contain at least 30 percent clasts larger than 2 mm in diameter of its volume with fine-grained matrix or cement.






(a)		(b)		
	FACIES	Continuity		Fault rock facies
		Appearance	%	
Breccias (with clasts)	Mt1		100	Mf1
Sand gouge	Mt2		90–100	Mf2
Shale gouge	Mt3		50–90	Mf3
Sand smear	Mt4		10–50	Mf4
Shale smear	Mt5		< 10	Mf5
Coal smear	Mt6			

Figure 3.5 – Membrane (M) fault facies classification schemes. (a) The different kinds of membranes with code name. (b) Geometry and the continuity of a smear, which range from fully continuous two small pockets. Figure from Braathen et al. (2009).

Lenses

Lenses are individual rock bodies detached from the host rock, are lozenge-shaped and bounded by slip surfaces on all sides and/or zones of shearing (Lindanger et al., 2007; Braathen et al., 2009). There are commonly membranes and/or slip surfaces along the boundary of lenses. Lenses can be found in the fault core and the damage zone and are not juxtaposed to their original location. Lenses can be homogeneous sandstone or shale, for instance, or a mix of both and other lithologies, as shown in Figure 3.6. Internal deformation can occur and range from undeformed to highly sheared networks (Lindanger et al., 2007; Braathen et al., 2009).

Diagenesis

Changes in properties in sedimentary rocks occur during increasing burial depth due to fluid mobility, and increasing temperature and pressure (Bjørlykke & Høeg, 1997), leading to processes such as compaction, recrystallization and cementation, in turn creating diagenesis in sedimentary rocks. Cementation is more common in more permeable units such as fractures and coarser sandstone and changes the sediments to become stronger and more brittle (Bjørlykke & Høeg, 1997; Braathen et al., 2009). Cementation processes, such as quartz cementation, can further lower the permeability of fluid migration (Færseth et al., 2007; Miocic et al., 2019).

3.2 Fault development

The early stage of extensional strain in the crust, or rifting, starts with localized zones of deformation (fractures and deformation bands), the develop into numerous short and isolated faults. These faults gradually grow in length and displacement (throw) over time (Whipp et al., 2014), commonly ending with a few very large faults surrounded by smaller abandoned faults. The length of a fault can be defined as the longest horizontal dimension. Overall, displacement of the fault tips is zero, while it usually increases close to the center of the fault surface. Of relevance herein, in seismic interpretation the fault tips are not visible because of the resolution limits, shown in Figure 3.7 (Kim & Sanderson, 2005).

FACIES		LtA	LtB	LtC
		Sand	Shale	Mixed
1	Undeformed			
	Isolated shears			
	Open network shears			
	Dense network shears			
	Anastomosing network shears			
	Swarm			

Figure 3.6 – Facies classification of fault lenses (L). The lenses are divided into sand, shale and Mixed. Mixed lenses can also contain coal and silt lithology. Lenses can contain internal deformation, such as fractures in different degrees and patterns. Figure from Braathen et al. (2009).

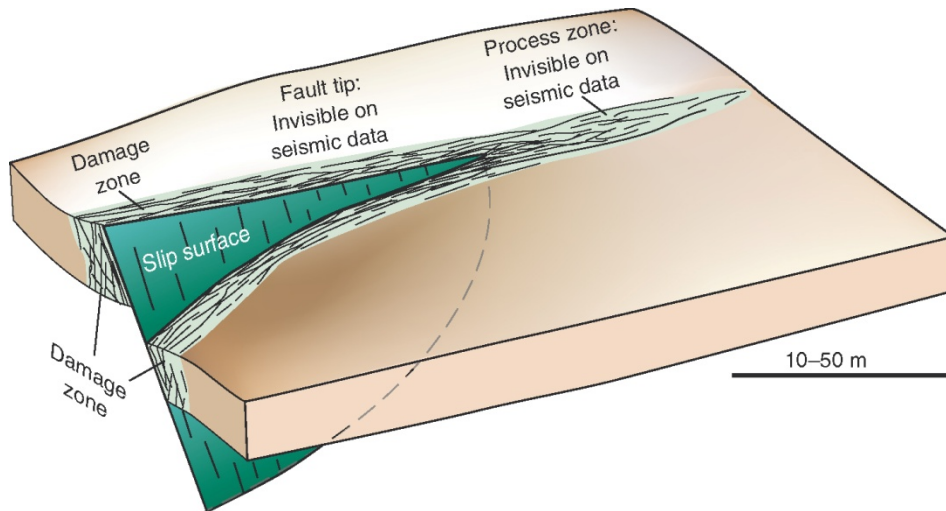


Figure 3.7 – Simplified illustration of a fault. In seismic data, the fault is interpreted with a single slip surface. The fault edges of a fault are not detected in seismic data and is therefore invisible. Figure from Fossen (2016) after Fossen et al. (2007).

Heave is the horizontal components of the dip-separation for a given fault, whereas the throw is measured by the vertical component of the dip-separation between the formerly adjacent beds of the fault, as shown in Figure 3.8 (Peacock et al., 2000; Lohr et al., 2008). In seismic interpretation, the fault surface is usually not smooth but instead exhibits curvature and irregularities in which the line along the fault surface between the two displaced adjacent beds represents the real displacement (Figure 3.8). Such irregularities on the fault surface, often termed corrugations, are assumed to result from fault growth by progressive segment linkage, as outlined below (Lohr et al., 2008).

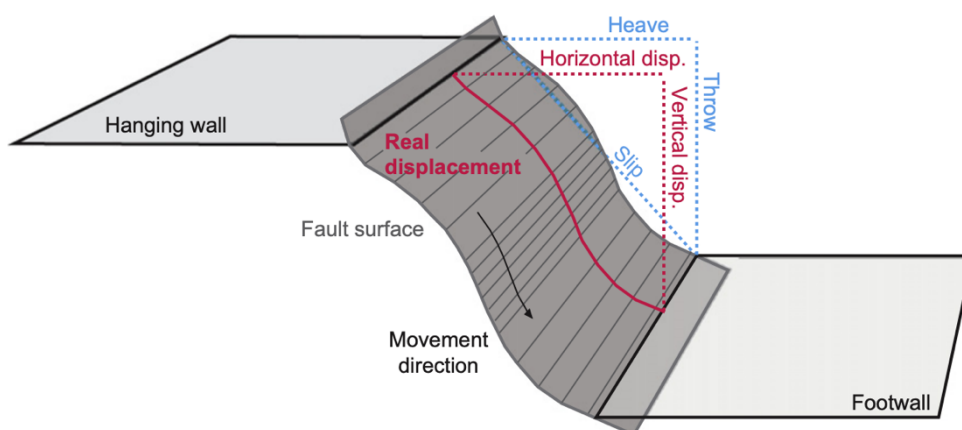


Figure 3.8 – Conceptual model showing the displacement (dip separation) parallel to the fault dip and the real displacement which follows the movement direction of the fault plane. Figure from Lohr et al. (2008)

3.2.1 Fault throw and growth

In any given stages of rifting, isolated faults will in most cases interact and propagate towards each other (Walsh and Watterson, 1988, Walsh et al., 1991, Kim & Sanderson, 2005; Fossen and Rotevatn, 2016; Rotevatn et al. 2018). Figure 3.9 shows three stages of fault growth by segment linkage. In stage 1, the isolated faults start propagating towards each other, whereas in stage 2 they start to interact and form a soft linkage. In this case they are not fully connected, offering a gap between the two segments, termed a relay zone. Simultaneously there is fault-length growth. Displacement versus distance profiles (throw-distance plots) shows the maximum displacement/length (d_{\max}/L) ratio, where there is a low ratio in the overlap zone between the two segments for stage 2. In stage 3, the fault segments become fully connected, i.e. hard linked, resulting in a rapid growth spurt in displacement especially in the former relay zone. Therefore, it is likely that the length and throw vary throughout the stages of fault growth and do not grow proportionally and linearly (Rotevatn et al., 2018). By analyzing throw variations, showing wave patterns in throw-distance profiles, troughs in displacement suggests pre-existing segments, either fully hard-linked or indicating more or less non-connected segments in relay zones.

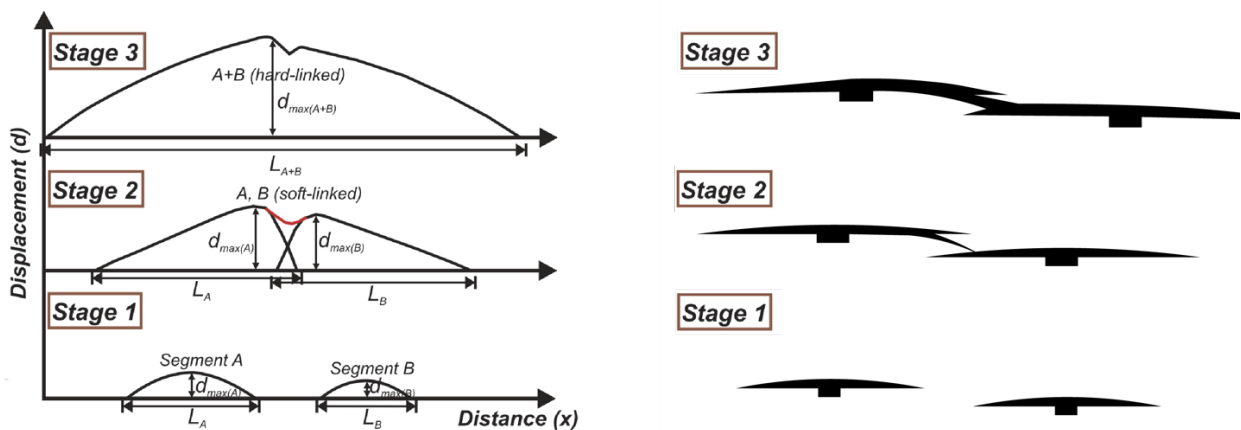


Figure 3.9 – Fault segmentation and linkage illustrations showing the throw (displacement) vs. length profile to the left and a drawing showing how isolating faults start to link with each other. The distance profiles to the left are from Kim & Sanderson (2005).

All large-scale faults (hundreds of meters to km throw) are primarily developed by fault linkage (Kim & Sanderson, 2005). When faults interact or link, the scaling attributes become more complicated, leading to the idea that small and large-scale faults should be interpreted

separately (Torabi & Berg, 2011). It is natural to assume that structures within and the zonation of the fault will grow proportionally with growing displacement. For instance, data from various fault sizes show that an increase in displacement is mimicked by an increase in fault core thickness (e.g., Bastesen and Braathen 2010), but there are two orders of magnitude uncertainties in such datasets (Fossen, 2020). The majority of studies have reported that there is a linear trend between the size of the fault and the size of the fault attributes (e.g. fault core, length and damage zone) (Torabi & Berg, 2011). However, there could have been sampling biases and other uncertain statistical decisions. Different scaling laws of small faults from larger faults are discussed (Marrett & Allmendinger, 1991). However, Schueller et al. (2013) conducted a study on 106 scanlines across normal faults in porous siliciclastic sediments and found a robust nonlinear relationship between the damage zone and throw, represented by a power-law equation with a 0.5 exponent. Therefore, the width of a damage zone can be approximately estimated based on the throw value with confidence. Predicting the distribution of internal structure in large-scale faults from small-scale faults (e.g. slip planes, lenses, breccia) is also challenging (Færseth et al., 2007).

A conceptual model of an isolated fault is often displayed as an elliptical figure (Figure 3.10, 1; Barnett et al., 1987; Nicol et al., 1996; Marchal et al., 2003; Torabi et al., 2019). They often display the displacement contours of a seismically interpreted fault, which usually illustrate a circular or elliptical shape. When the fault interacts with other features, such as the ground surface, soft linkage (relay zone) or full intersection, the shape of the fault changes (Figure 3.10, 2-4).

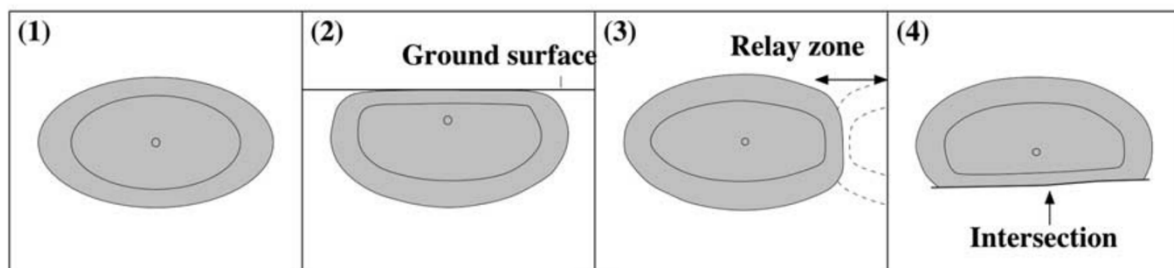


Figure 3.10 – Simplified figures of normal faults. The shape can be affected when interacting with other features. (1) Simple shape for an isolated fault is the elliptical figure. (2) Restriction to the ground surface. (3) Soft linkage interaction with another fault; Relay zone. (4) Intersection with another plane. Figure from Marchal et al. (2003).

3.3 Across-fault seals

Fault systems are inevitable in most the North Sea settings; therefore, when storing CO₂ in the subsurface, faults must be inherently sealed to prevent leakage. Faults can be obstacles (seals), baffles or conduits for fluid flow in the CO₂ storage reservoir, both across and along the fault, hence affecting fluid migration (Bjørlykke, 1993). There are different ways of forecasting sealing of a fault; some have better sealing probabilities than others.

3.3.1 Juxtaposition seals

Juxtaposition seals provide the highest fault seal probability in seismic interpretation, with the 1D triangle diagram used in analyzing this type of sealing (Figure 3.11b; Knipe, 1997; Færseth et al., 2007). Figure 3.11a display a three-dimensional view of a normal fault, where the throw increases from the left tip to the bottom of the block. In a normal fault, the hanging wall has moved relatively down compared to the footwall. With increasing throw,

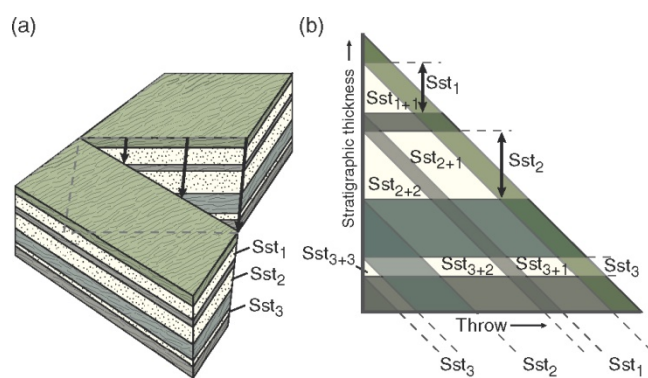


Figure 3.11 – Concept of 1D triangle diagram, (a) 3D figure displacing how the juxtaposition is displayed in the triangle diagram, where the throw start from zero on the left size and increases in the right direction. (b) 1D triangle diagram showing the sandstone (sst) and shale units juxtaposing in increasing throw values. Figure from Fossen (2016).

various stratigraphic units in the hanging wall are juxtaposed with the older units in the footwall (Dennis, 1967; Knipe, 1997). This is further communicated in an Allan diagram (Allan, 1989), which shows the stratigraphy of the overlapping hanging wall and footwall of a fault plane. The juxtaposition relationship varies along the fault plane, possibly leading to cross-fault migration caused by self-juxtaposition spilling points, for instance where throw is low, and a sandstone is placed in contact with its hanging wall counterpart (Figure 3.12). Figure 3.12 shows the Allan diagram and the map view of a fault, where the stratigraphy consists of sandstone units with fluid marked in colors. The fluid accumulates and traps in the highest point of the sandstone units. The sandstone units with red arrows display the self-juxtaposition and the direction of the buoyant CO₂ migrates (Allan, 1989). An advantage of using the 1D triangle diagram instead of the Allan diagram is the avoidance of performing detailed 3D mapping of the stratigraphic

horizons and the fault plane. 1D triangle diagram also allows further modelling of important parameters such as permeability and Shale Gouge Ratio (SGR) values (sealing capacity) (Knipe, 1997).

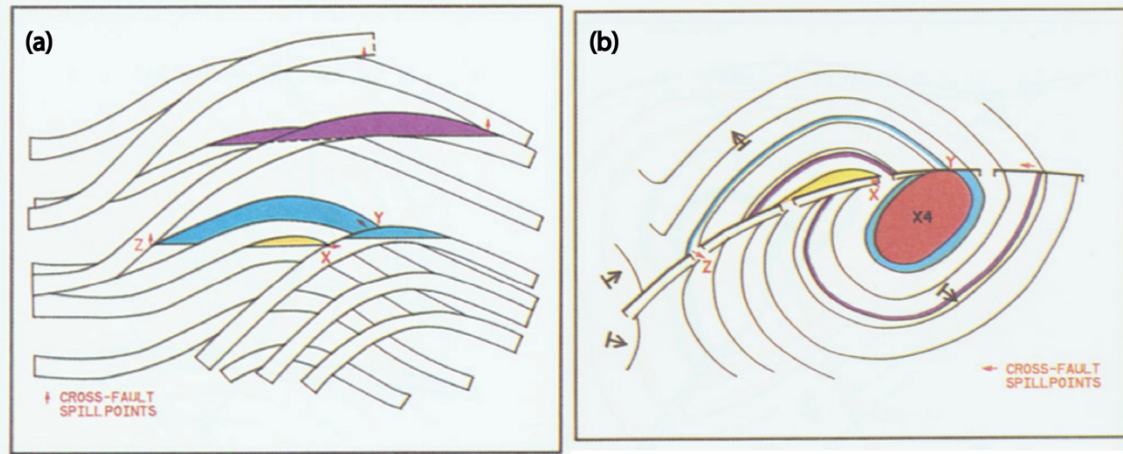


Figure 3.12 – Illustration of cross-fault migration scenario. (a) Allan diagram (b) map view. Red arrows showing the cross-fault spill points with letters. Figure from Allan (1989).

In a juxtaposition seal, a permeable sandstone layer is juxtaposed with an impermeable unit, such as shale or a mudstone layer. The potential fluid in the sandstone layer is not likely to migrate because of the sealing impermeable shale/mudstone layer and, essentially, the fluid getting trapped. The opposite of juxtaposition seal is sand-on-sand juxtaposition, where it is less likely to seal and can potentially promote across-fault fluid migration. A juxtaposition seal is considered a very high probability seal (70-100%) only if excluding other factors. However, if the fault core contains porous structures, the fault plane is not a barrier to fluid flow (Færseth et al., 2007). The juxtaposition seal is based on seismic data; therefore, it is important to utilize other sealing categories to strengthen the sealing probability.

3.3.2 Membrane seals

Juxtaposition seals are considered the most probabilistic forecast for seal or CO₂ leakage. However, membrane seals can also attribute a viable seal probability (50-70%) (Færseth et al., 2007). This reasoning is based in the fact that here have been examples of sealing faults that display self-juxtaposition, where the membrane is the sealing component (e.g., Schowalter, 1979; Watts, 1987; Fristad et al., 1997; Yielding et al., 1997; Færseth et al., 2007).

How trustworthy the membrane seals are, depends on the pressure build-up from the CO₂ or hydrocarbon accumulation underneath the seal (Schowalter, 1979; Miocic et al., 2019). The buoyant CO₂ or hydrocarbons accumulation creates a pressure difference (ΔP) at the interface of the seal to the reservoir, proportional to the column height (h) of the buoyant fluids, gravitational constant (g) and the density difference between the brine (ρ_w) and the buoyant fluids (ρ_f), expressed in equation (3.1) (Schowalter, 1979; Miocic et al., 2019).

$$\Delta P = (\rho_w - \rho_f)gh \quad (3.1)$$

The capillary forces control the trapping of the CO₂ or the hydrocarbons, which the capillary pressure is the pressure difference that occurs at the interface of the buoyant fluids CO₂ or hydrocarbons and the brine; the pressure of buoyant fluids (P_f) and pressure of the brine (P_{brine}) (Miocic et al., 2019). The capillary pressure (P_c) is expressed in equation (3.2) as the interfacial tension (IFT) between the buoyant fluid and the brine, the wettability of rock-mineral surface with respect to the buoyant fluids, expressed as the contact angle (θ), and inversely proportional to the size of the pore-throat radius (r) (Schowalter, 1979; Miocic et al., 2019).

$$P_c = P_f - P_{brine} = \frac{2IFT \cos(\theta)}{r} \quad (3.2)$$

Leakage or seal failure occurs when the pressure from the buoyant fluids exceeds the capillary breakthrough or threshold pressure and the maximum column height that can no longer support, expressed in equation 3.3 using equations 3.1 and 3.2 (Miocic et al., 2019). The Capillary threshold pressure is defined as the wetting phase in a low permeability rock, such as shale, which does not go through where the threshold of the percolation is exceeded, and therefore, a non-wetting phase forms across the pore network.

$$h = \frac{2IFT \cos(\theta)}{r} \times \frac{1}{(\rho_w - \rho_f)g} \quad (3.3)$$

Clay Smear Potential (CSP), Shale Smear Factor (SSF) and Shale Gouge Ratio (SGR) are fault seal algorithms, which disregard the fault architecture. These methods presume the fault consists of a simple shear zone (Figure 3.13; Færseth et al., 2007), in an upscaling or simplification that basically suggests that there is a perfect mixing of fault core materials into a membrane.

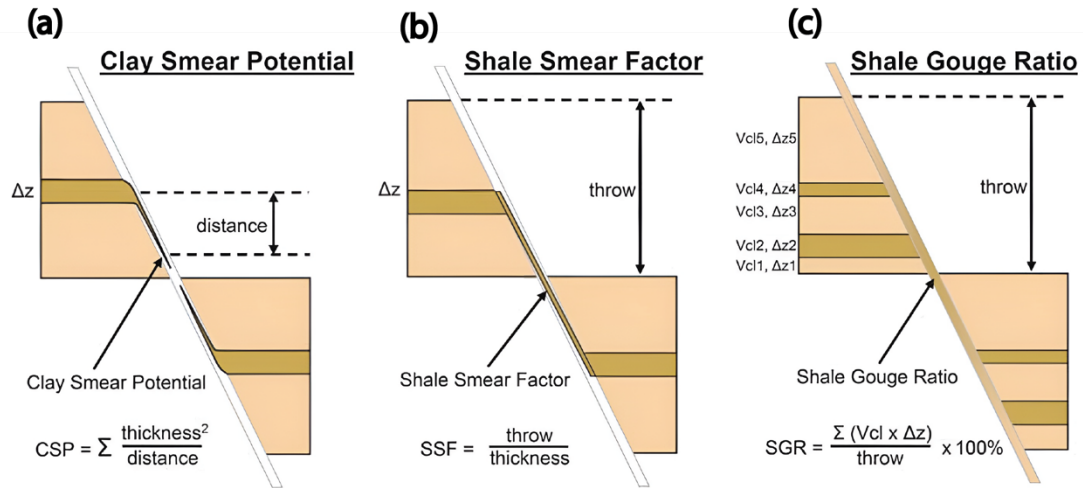


Figure 3.13 – The three main seal probability algorithms. (a) Clay Smear Potential (CSP). (b) Shale Smear Factor (SSF). (c) Shale Gouge Ratio (SGR). Figure from Yielding et al. (2010) after Yielding et al. (1997)

Clay Smear Potential (CSP) algorithm does not directly calculate the presence of clay smear but the likelihood of clay smear in a fault zone (Figure 3.13a; Bouvier et al., 1989; Fulljames et al., 1996). CSP calculates at a certain point of the fault of how much clay has been smeared from each shale unit that passed the calculation point.

Shale Smear Factor (SSF) algorithm calculates at any given point on a fault by estimating how likely a specific shale unit is to form a continuous smear on that point (Figure 3.13b; Lindsay et al., 1993). SSF factors greater than seven lead to incomplete fault smear (holes in the membrane), and SSF equal to four or closer to zero gives a better probability of forming an intact layer of sealing smear (Færseth et al., 2007).

Shale Gouge Ratio (SGR) calculates the percentage of shale or clay smear in a slipped interval (throw) at any given point on the fault surface, considering the ratio of sand to shale (Yielding et al., 1997). This algorithm (equation 3.4) is based on the net shale thickness times volumetric shale fraction V_{cl} divided by the throw of the fault.

$$SGR = \frac{\sum V_{cl} \times \Delta z}{\text{throw}} \times 100\% \quad (3.4)$$

V_{cl} is the amount of clay in the shale/clay beds, which can be derived from petrophysical well log data, such as gamma-ray and neutron-density logs (Bretan et al., 2003). If we assume that the shale/clay beds are 100% clay material, equation (3.5) can be used instead (Yielding et al., 1997).

$$SGR = \frac{\sum \Delta z}{throw} \times 100\% \quad (3.5)$$

Smear can form from other lithologies, such as coal, micaceous sand, silt, and carbonates (Færseth, 2006). There is a higher chance of continuous smear from a single thick source bed than from multiple thin shale/clay units, even if the SGR ratio is the same for both instances (Færseth et al., 2007). Leakage points are more likely to be present from multiple smaller shale/clay units. For a specific SGR value, the sealing capacity of a fault increases if the temperature exceeds 90 degrees Celsius (i.e., a burial of 3000 m or more), which also includes the possibility of quartz cementation (Færseth et al., 2007).

Of relevance for this thesis is the fact that SGR is considered for both a subsurface fault (Aurora CO₂ storage site) and for outcropping faults (Utah). Hence, different methods are employed: Aurora site apply a gamma log approach, whereas outcrop fault of Utah uses detailed stratigraphic logs in which clay-silt-sand content are considered in the field (see Methods).

3.3.3 Possibility of sealing sand lenses and internal structures

As we previously mentioned, faults are likely to offer an intricate architecture, such as multiple slip planes, sand lenses and other mixing lithologies that the seismicity cannot detect (Færseth et al., 2007). If existing sand lenses within the core are placed in a way where they are in contact with both sand beds in the hanging wall and the footwall, this can reduce the sealing probability to 30-60% of membrane and juxtaposition seals (Figure 3.14). Then reduced seal probability is caused by the higher possibility of leak pathways through the entrained sand lenses due to

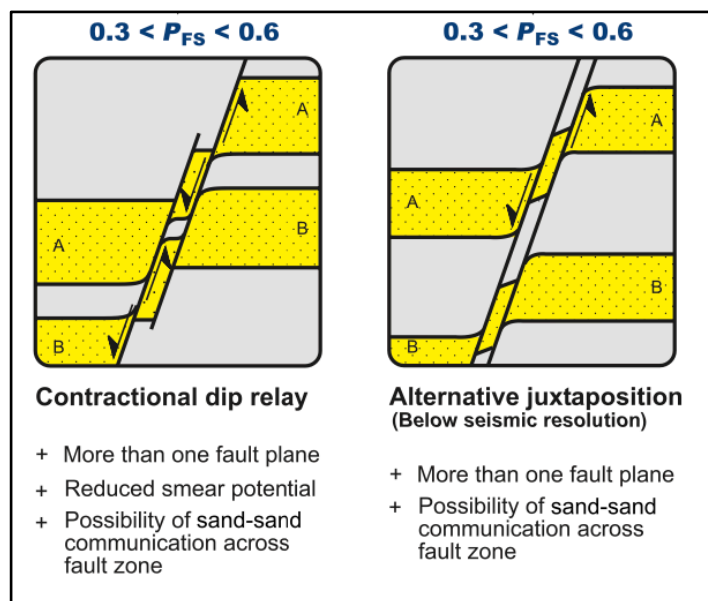


Figure 3.14 – Conceptual models of more complex structures within the fault core; multiple slip-planes and sand lenses. Figure to the left shows that sand lenses reduce smear potential and the sealing probability. Figure to the right shows a juxtaposition seal, but sand lens structures below seismic resolution can potentially lead to fluid migration across the fault. Figure from Færseth et al. (2007).

sand-sand communication across faults. Nevertheless, there is still a likelihood of sealing if the sand lenses are enclosed in a fine-grained fault-core material (e.g., gouges), where cross-fault migration becomes much less likely. Cementation, diagenesis and cataclasis in the fault zone will also increase the sealing probability (Færseth et al., 2007). This uncertainty can be further considered by detailed outcrop studies of faults, as is part of this thesis.

4 Methods and data

In this chapter I present the methods and data applied in this thesis. First, I explain the how we collected field data from the study area Floy Canyon of the lower Book Cliffs in Utah, USA, the processing of the field data and which software was used. Second, I present the data supporting the seismic interpretation of the Aurora storage site, and the methodology behind the seismic interpretation.

4.1 Fieldwork

This sub-chapter presents the methodology behind the obtained field data in Floy Canyon. The field data were collected from 30th August to 15th September 2022, partly with my supervisors and fellow UiO postdoctoral Sian Lianne Evans. My supervisor Nora Holden and I cooperated during every fault observation, drone photographing and data collection. My main supervisor Alvar Braathen guided me on how to interpret fault facies and structures. Rikke Bruhn and Alvar Braathen logged the stratigraphy of the study area. The temperature could reach up to and sometimes above 40 degrees Celsius in the middle of the day, and the clear sky was mainly during the stay. The temperature sank in the last few days of the field trip, and rainy weather followed.

4.1.1 Equipment

A Silva Expedition S compass was used to measure the orientation of planar and linear features in the core and damage zone of the fault outcrops. Since this fieldwork aimed to analyze the fault facies and not make geological maps, the compass was not adjusted for declination. The right-hand rule was applied when using the compass. The close-up photographs of the faults were taken with an iPhone SE (second generation). Overview and far-distant photos were taken with a DJI Mavic Mini drone. A foldable ruler was used to measure different parts of the faults, such as the fault offset, and ensure a scale for the drone photos. The coordinates positions of the faults were taken with an iPhone SE (second generation). However, because of the inaccuracy of using a cellphone, some of the coordinates had to be adjusted using FATMAP (fatmap.com) to get more precise positions.

4.1.2 Scan line data

In addition to taking several photos and doing detailed sketching of the faults, a one-dimensional line-intersection method, i.e., scanlines, was implemented to make a complex intersection of the fault core with measurements. Scanlines were measured on each fault, one upper and one lower. The scanline was placed perpendicular to the fault core covering approximately 10 cm of the hanging wall and the foot wall. Each boundary was measured and identified, such as membranes, lenses, breccias and slip planes. Where the sandstone was homogeneous enough to see throughgoing fractures and deformation bands, scanlines were used to count fractures on the damage zone of both sides of fault 3 in location 2.

4.1.3 Fault facies interpretation

As mentioned, fault facies can be classified into elements of discrete structures, membranes, and lenses (chapter 3.1.2 with classifications). All the studied faults consist of these elements with varied degrees of combinations. The interpreted lenses are classified as lozenge-shaped rock bodies, and in many cases host original structures (e.g., bedding structures). Four types of lens abbreviations are applied: LtA: sandstone lens, LtB: shale or mudstone lens, LtC: heterogenous mix of lens and LtD: Coal lens. Based on outcrop observations, lenses are always bounded by slip-planes and occasionally membranes. Usually, there are internal strain in the lenses, such as fractures in the LtA and some drag-shearing in LtB, LtC and LtD. The degree of fractures in LtA have been classified (according to Figure 3.6).

Membranes are present along the slip surfaces, in this study covering coal smears, gouges and breccias. Protobreccia refers to a type of breccia composed of a single lithology that has been comminuted into a mixture of small clasts with little matrix (Woodcock & Mort, 2008).

As mentioned, discrete structure classification (see sub-chapter 3.1.2) encompasses shear fractures, slip surfaces and deformation bands. Deformation bands (mainly mildly cataclastic shear compaction bands) occur in porous sandstones within damage zones and in some sandstone lenses. Fractures (joints and shear fractures) appear similarly, but in low-porosity units. Slip-surfaces exclusively locate in the fault core.

4.1.4 Processing field data

After analyzing and finished sketching of the faults, I made illustrative figures of the faults with the program Adobe Illustrator (2021). The lithostratigraphic logs was recorded by Rikke Bruhn, Alvar Braathen and shows the lithology of the Floy Canyon study area. The locations of the lithostratigraphic logs locations were chosen to obtain the lithology of the southern part of location 2 and the more northern part of the location 2, which cover the footwall and hanging wall of some of the studied faults.

4.1.5 Sealing assessment

I am utilizing the same sealing probability method Shale Gouge Ratio (SGR) on the physical analogue faults primarily used in seismic interpretation when estimating the sealing of faults (Holden et al., 2022). This is to compare the results with the F1 fault in the Aurora storage site (Figure 4.1). With the help of the logging sheets, I can calculate SGR with equation (3.5) and SFF more precisely, especially with the faults with larger throw values. I am able to calculate SFF and SGR with direct measurements from the hanging wall and the footwall in the faults with only a few meters throw. The internal fault core structures were analyzed to see if they contain sealing properties.

4.1.6 Field data limitations

Outcrop data provides information on details that is not resolvable in seismic data. However, there are some limitations. Vegetation is one problem many geologists face, which covers important structures and hinders us from getting the full picture of the geology in the area in question. Fortunately, Floy Canyon consists of mostly naked faults, where vegetation is not a problem. However, the Floy Canyon has been exposed to weather conditions which have weathered the outcrops. The faults in Floy Canyon have probably been exposed for a long time, which has led to weathering. We had to deal with weathered segments of the fault, which led to mud covering and eroding fault structures. Weathering can make it difficult to observe fractures in the damage zone area, for instance. In the fault core, removing any dirt, for the most part, was possible.

The temperature and weather can also impact the interpretation. During fieldwork in Floy Canyon, a minor heatwave led to increasing temperatures during most of our stay. For people

not used to heat can potentially increase the chance of human errors. Limited time during a stay will always be a negative factor that can reduce detailed observation. The road within the study area was drivable only in nice weather, and rain made it impossible to drive using normal cars. The last few days during our stay in Utah, we had moderate precipitation, which prevented us from driving.

The last-mentioned limitation of using physical outcrop data is the 2D view. In Floy Canyon, the faults were presented in a crossed cut 2D view, which did not allow us to observe the structures in 3D. For instance, we do not know how much of the membranes and lenses extend inwards on the fault plane. For all we know, the continuous membranes we observed in the outcrop, could be discontinuous along the strike of the fault plane. Lastly, no outcrop analogues are perfect, which means that two identical depositional environments do not exist. Therefore, expecting to achieve perfect results are not realistic (Howell et al., 2014).

4.2 Seismic interpretation data

The seismic method is the most widely used geophysical technique for surface mapping in hydrocarbon exploration and CO₂ storage. This section describes the data used for the seismic interpretation part. In three parts, we will explain the 3D seismic data, 31/5-7 well data and the velocity model, which was utilized to depth convert the data.

4.2.1 3D seismic data

Seismic reflection imaging provides subsurface mapping, which shows geological structures. The seismic data is gained by high-energy source (e.g., air guns) at the surface generating low-frequency sound waves that travel down through the earth and gets reflected at the boundaries between two different layers of rock properties (Bacon et al., 2003). The reflected sound waves travel back to the surface, and a receiver records the information. The receiver records information such as the time the sound waves travel from the source to the receiver. By knowing the travel times from the source to receivers, and the velocity of the seismic waves, the geophysicist endeavors to construct an image of the subsurface by reconstructing the pathways of the waves. The strength of the reflected signal gives us information about the change in rock properties. The travel time is measured in two-way time (TWT) expressed in milliseconds (ms) and is displayed on the vertical axis of a seismic reflection image. A reflection of a subsurface

interface shows a change in a quantity called acoustic impedance, which is the product of density and seismic velocity in the layer of a rock, the physical property of the layer. A layer unit must have a certain thickness to get distinguished as an individual reflection (i.e., resolution limit); therefore, not all interfaces are visible on seismic data (Bacon et al., 2003). Thus, a conventional seismic data set typically have a vertical resolution limit ranging from 15-25 m (Faleide et al., 2019).

The 3D seismic data provided for this study is the survey GN10M1 and was acquired from Gassnova in 2010, where the quality of data is considered good/very good at the target formations of the Lower Jurassic storage complex (Gassnova, 2012). The seismic resolution is roughly 15.75 m at the Sognefjord level (Michie et al., 2021). The seismic volume GN10M1 is merged with the seismic cubes GN1001, NPD-TW-08-4D-TROLLCO2 and NH0701 and covers approximately 1370 km² within the Horda platform (Figure 4.1). In the GN10M1 dataset, the inline traces trend E-W with 25 m spacing and the crossline traces trend N-S with 12.5 m spacing. The vertical axis of the GN10M1 seismic cube is displayed in TWT, which records down to 4000 ms TWT (Gassnova, 2012). The study area, which only includes the target fault F1, covers 69 km². This chosen area avoids covering the other fault in the Aurora storage site and only focuses on the target F1 fault.

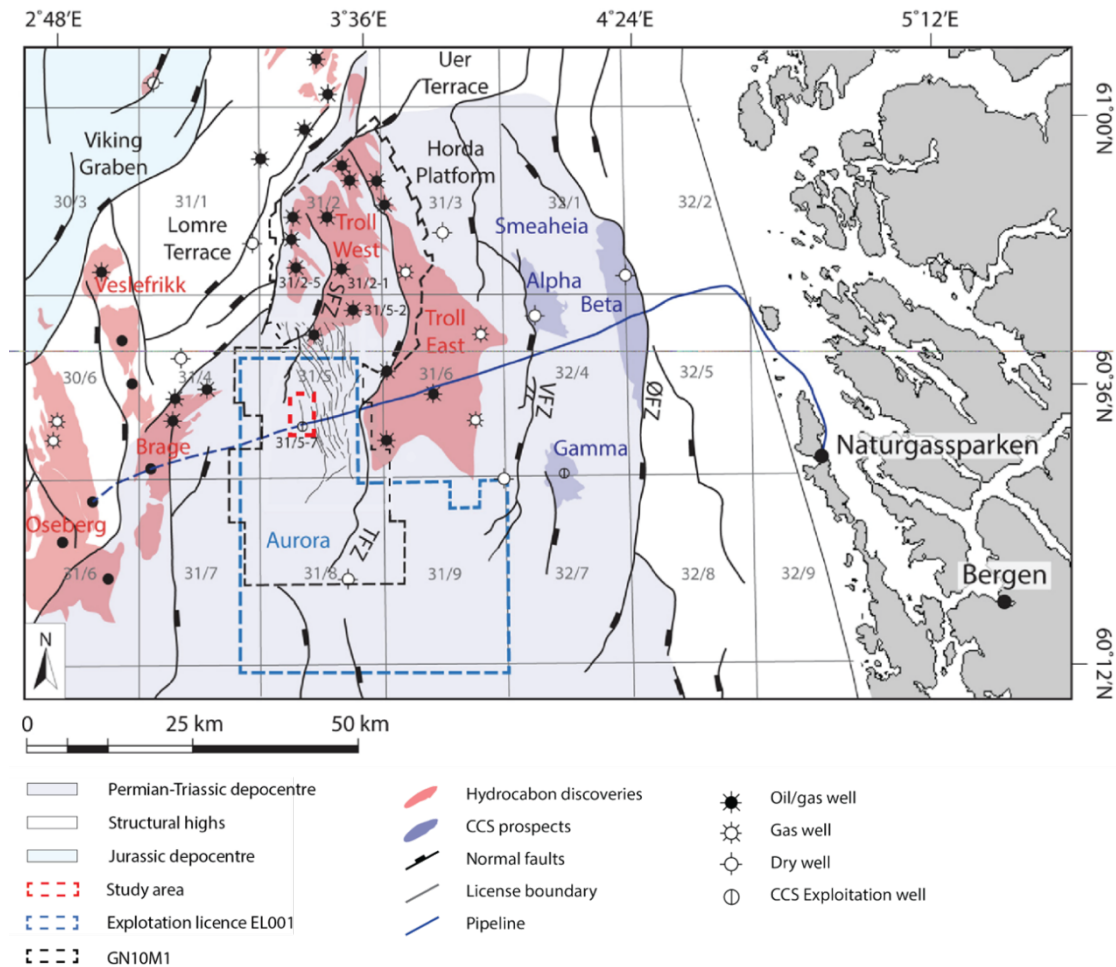


Figure 4.1 – Overview map of structural elements of northern Horda Platform. Map includes outline of exploitation license EL001, Hydrocarbon discoveries and CCS prospects. Black stippled outline GN10M1 merged 3D seismic survey and the red stippled is the study area. Figure modified from Holden et al. (2022).

The 3D seismic dataset GN10M1 is imaged using the Society of Exploration Geophysicists (SEG) normal polarity in seismic zero-phase polarity (Holden et al., 2022). To better understand the seismic dataset, we need to have knowledge of the two SEG polarity conventions, normal and reverse and phase signal (Herron, 2011). The polarity conventions define the wiggle line of acoustic impedance as a peak or a trough. Normal polarity is defined where the increase in acoustic impedance, displayed as a positive polarity (amplitude to the right), represents a peak, and a decrease in acoustic impedance shows negative polarity (amplitude to the left), representing a trough. Zero-phase polarity is most used by interpreters today and displays the maximum amplitude in the centre of the waveform and correlates with the time horizon (Brown, 2011). Since the phase and polarity convention is already known for the GN01M1 survey by a previous study (e.g., Holden et al., 2022), in normal circumstances, the polarity convention and phase can be found by the seabed reflection; however, it is often unreliable because it is not a

single interface (Brown, 2011). A better method to find the polarity convention and phase is to find a fluid contact reflection or a flat spot in the seismic data. In the figures and tables throughout this study, an increase in acoustic impedance (peak) is shown in red or black, while a decrease in acoustic impedance is shown in blue or white.

4.2.2 31/5-7 well data

The 31/5-7 well (Eos well) located in the Norwegian quadrant 31/5 (Figure 4.1) was drilled by Northern Lights project in 2019 and confirmed the presence of suitable CO₂ storage and seal and will be the injection well for the CCS project in Aurora storage site. The well confirmed 116-meter-thick Johansen Formation (primary storage), 57-meter-thick Cook Formation (secondary storage), and 128-meter-thick Drake Formation (Figure 4.2; NPD Factpages, 2023). The Lower Drake Formation is classified as the primary seal, which has a 53 m thickness (Rahman et al., 2022).

4.2.3 Velocity model

A velocity model made by Michie et al. (2021) was utilized to convert the time domain milliseconds TWT to the depth domain in meters. This velocity model was created using quality-controlled time–depth curves from 15 wells from the Troll and Smeaheia area. Depth conversion is necessary to get more accurate imaging and representation of the structures on the surfaces and the fault (Lyon et al., 2004).

4.2.4 Data Limitations

Seismic data can provide a fully 3D view when interpreting surfaces and faults, unlike physical analogue data. However, the limitations need to be addressed when interpreting seismic data to

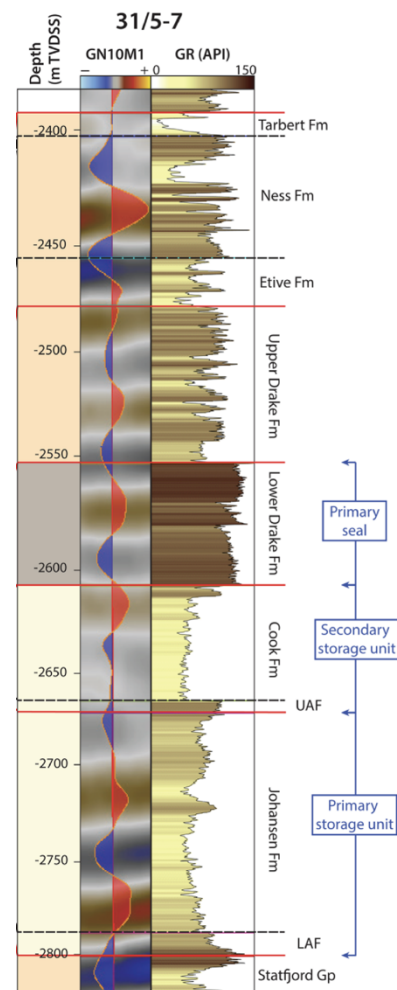


Figure 4.2 - Gamma-ray (GR) log from well 31/5-7 (Eos) together with a synthetic seismogram created using log data from well 31/5-7. Red continuous and stippled lines showing the interpret boundaries of the formations. Abbreviations: UAF, Upper Amundsen Formation. Figure from Holden (2022).

be aware of the uncertainties the results can give. As previously mentioned, the seismic resolution limit is a limitation we face when working with seismic data. In vertical and horizontal distances, the seismic resolution limit is the minimum distance to distinguish features from one another (Sheriff, 1977). The wavelength (λ) of the seismic signal controls when features can be distinguished, which increases in depth due to the attenuation, which also leads to a decrease in resolution. We can find the wavelength by measuring the distance between two amplitudes or dividing the seismic velocity (v) by the dominant frequency (f) of the seismic (Sheriff, 1977; Herron, 2011).

The vertical resolution is restrained by the interference thickness; the interference starts at $\lambda/2$ (Brown, 2011). Interference occurs when horizons with different geophysical properties are closely spaced together. This can cause overlapping of seismic waves, increasing or decreasing the seismic polarity. The vertical resolution is also the limit of separability ($\lambda/4$), in which the maximum interference occurs when the spacing is less than a quarter of the wavelength (Brown, 2011).

The horizontal resolution is constrained by the Fresnel zone, where a portion of the reflector from which the seismic energy is reflected reaches the detector within a one-half wavelength of the first reflected energy and interferes constructively (Sheriff, 2002). With 3D seismic data, we have the input of the waves in all directions; when a horizon pinches out in one direction, it could be visible for longer in another direction (Brown, 2011). The spacing between lines in a 3D seismic is typically closer than in a 2D seismic grid. Therefore, 3D seismic decreases the size of the Fresnel zone, which improves horizontal resolution (Brown, 2011).

4.3 Seismic interpretation methods

This section will explain the methodology process behind the seismic interpretation of the study area that covers the isolated F1 fault (Figure 4.1). In stage one of the process, the seismic interpretation was performed by using the software Petrel E&P Software Platform (v. 2022.1), and in stage 2, the fault modelling and analysis was done with Petroleum Experts (PETEX) Move suite (v. 2022.1). To reduce any visual misrepresentations, figures of fault surfaces are presented in a uniform color map ‘batlow’ created by Crameri et al. (2020). The workflow is illustrated in Figure 4.3.

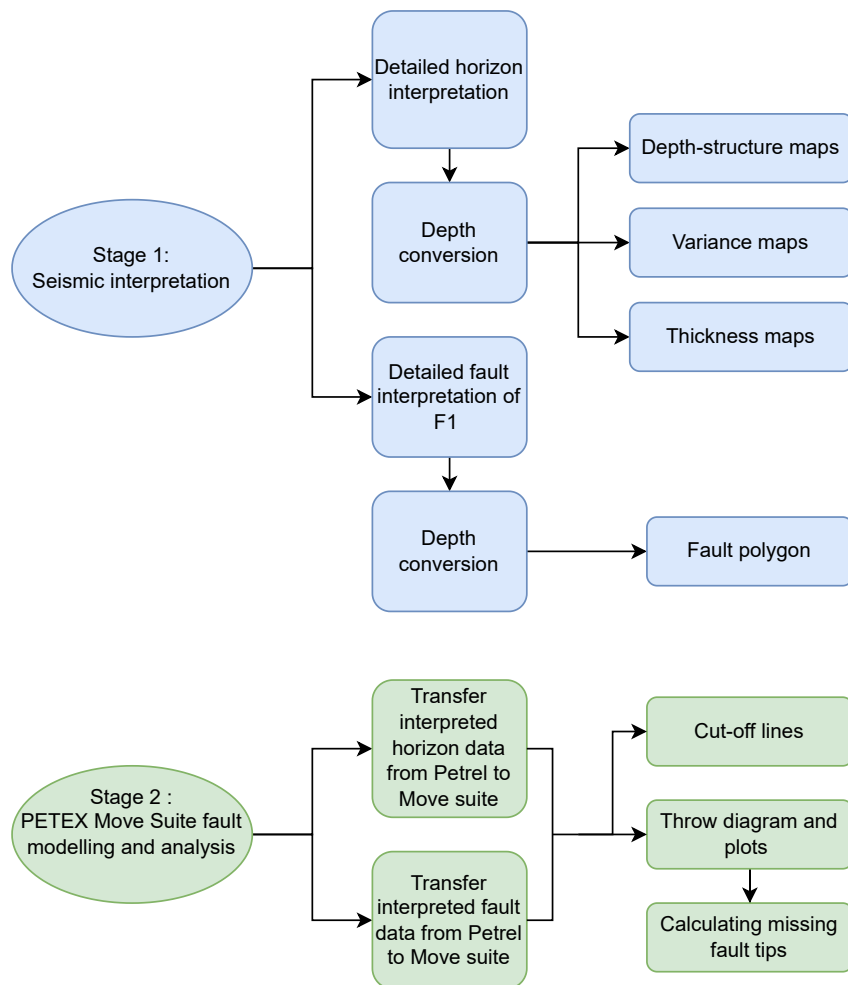


Figure 4.3 – Flowchart showing the seismic interpretation workflow in two stages. The results are illustrated as the boxes to the right. Figure made with Draw.io.

4.3.1 Eos well tie

The Eos well 31/5-7 is tied to the seismic data and utilized to pinpoint where the geological formations are placed in the seismic reflection. Wellbore data provide higher vertical seismic resolution and can establish a time-depth relationship between the wellbore data (depth) and the seismic data (time).

4.3.2 Horizon interpretation

In stage one of the seismic interpretation workflow, ten horizons were interpreted within an area of 69 km² that approximately only covers the F1 fault. The target formations for the CO₂ storage in the Aurora storage site of this study is within the Lower Jurassic Dunlin Group; Amundsen, Cook, Johansen, and Drake formations. In this study, intra-horizons, which are horizons between top and bottom boundaries-reflection in a formation, are included to get a more detailed inspection of the target formations. The Drake formation is the primary seal, where the lower portion contains most clay material, and therefore is assumed to inherently more sealing than the

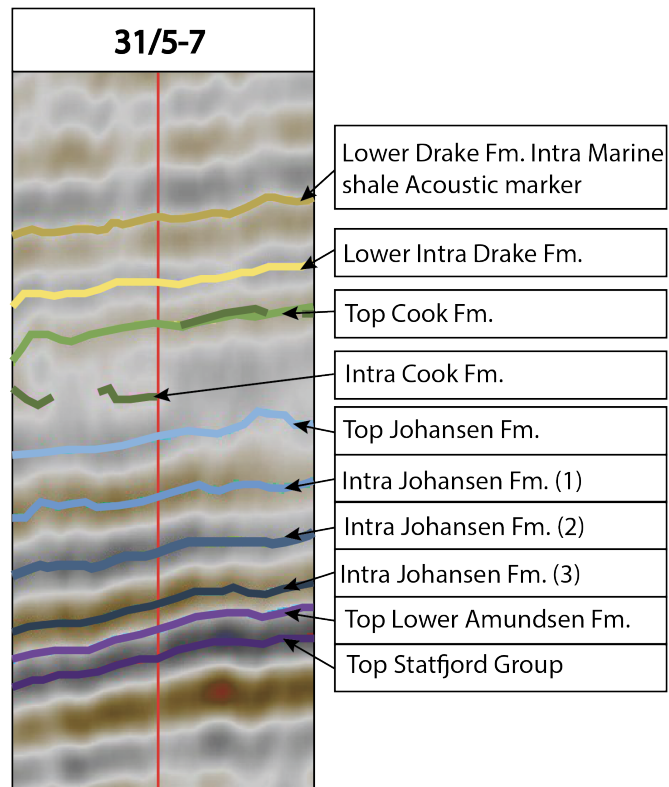


Figure 4.4 – Seismic section of the 31/5-7 (Eos) well and the interpret horizons.

upper portion of Drake Fm (described in sub-chapter 2.2.2) (Gassnova, 2012). Drake formation is interpreted in two horizons: Lower Drake Fm. Intra Marine shale, which is an acoustic marker from the 31/5-7 well, and Lower Intra Drake horizon (Figure 4.4).

The secondary storage unit consists of the Cook and Upper Amundsen formations, where in this study, we interpret two Cook horizons; Top Cook and Intra Cook (Figure 4.4). Upper Amundsen, which is located over Johansen formation, is considered too thin to be interpreted, 7m thick in 31/5-7 well, and therefore is not included (Gassnova, 2012; Sundal et al., 2015).

The primary storage consists of Lower Amundsen and Johansen formations, where the top Johansen horizon got interpreted along with three intra-Johansen horizons and one Lower Amundsen horizon (Figure 4.4). Top Staffjord Group is underlying the Lower Amundsen formation and is included because stratigraphy below and above can juxtapose on the storage complex because of the vertical movements of a fault. Brent Group, which is located over Drake Formation, was initially included in this study. However, the interpreted Brent horizon was

located too far from the other interpreted horizons along with fault modelling difficulties, where the cut-off lines had too many errors (see sub-chapter 4.3.4). Therefore, the Brent horizon got excluded from this study.

Table 4.1 shows the interpreted horizons along with the reflector pick and reflection quality. The reflector pick was chosen based on the 31/5-7 well, which pinpoints where the formations are placed more accurately than the seismic data. Lower Drake Fm. Acoustic marker and Top Lower Amundsen Fm. are picked herein in zero-crossing marker. Most of the horizons had strong and continuous reflection quality, except for Intra Cook Fm., which had very weak and highly disrupted reflection (Figure 4.4).

Table 4.1 – List of interpreted horizons within the GN10M1 3D seismic volume in this study, with the reflector pick and the quality of the reflection.

Seismic horizon	Reflector pick	Reflection quality
Lower Drake Intra Marine shale Fm. Acoustic marker	zero-crossing	Strong, continuous
Lower Intra Drake Fm.	Trough	Strong, disrupted
Top Cook Fm.	Peak	Strong, continuous
Intra Cook Fm.	Peak	Weak, very disrupted
Top Johansen Fm.	Trough	Weak, disrupted
Intra Johansen Fm. (1)	Peak	Strong, continuous
Intra Johansen Fm. (2)	Trough	Strong, disrupted
Intra Johansen Fm. (3)	Peak	Strong, continuous
Top Lower Amundsen Fm.	zero-crossing	Strong, continuous
Top Statfjord Group	Trough	Strong, continuous

The target horizons were interpreted from survey inlines and crosslines in every 50th increment spacing, which gave approximately a 625x1260 m grid resolution. Auto tracking was performed after the study area was filled with a grid that confidently crosscut each other in the same horizon reflector. Cases where areas had too many irregularities and auto tracking, tracked the wrong reflector, needed to be revised. Smoothing was operated to exclude any unnecessary irregularities on the surface. This is to avoid any difficulties in the fault modelling analysis, which will be explained further in sub-section 4.3.2. In the end, the interpreted horizons and F1 fault in the time domain got converted to depth-domain using the velocity model.

4.3.3 F1 – fault interpretation

The second part in stage one of seismic interpretation is to interpret the isolated fault F1. The seismic attribute map, called variance, was primarily used in the fault interpretation, which helps with highlighting structural discontinuities, such as faults. An attribute is a measurable property of the seismic data, such as amplitude, dip, frequency, phase, and polarity (Brown, 2011). The seismic variance map was generated for the entire 3D seismic cube, and the attribute variance computed the local variance along the traces of a given horizon, vertical slice or volume.

The interpretation of the F1 fault was made with an inline spacing of 75 m (increment 3) and simultaneously using the variance map to ensure there were no sudden jumps or edges on the fault surface. For instance, I inspected the variance map in time slices to ensure that the interpreted fault surface cuts where the variance is strongest. I used inline seismic sections to interpret along the fault, which is oriented perpendicular to the fault strike of F1. In this study, I only interpreted the fault where I saw an offset in the seismic reflection. As previously mentioned, the seismic resolution limit does not detect structures under the size of ca. 15 m, therefore resulting in missing fault tips in seismic fault interpretation (Kim & Sanderson, 2005). This will be further explained in the next subsection.

4.3.4 F1 – fault modelling and analysis

Stage 2 of the seismic interpretation workflow is the fault modelling and analysis (Figure 4.3). The first step was to transfer the depth-converted horizon and fault data to the PETEX Move (v.2022.1). The interpreted grids and auto-tracked horizons got transferred as points, and the fault got transferred as 2D fault sticks. The surfaces were transferred into meshes, 3D surfaces. To assess the throw variation along the fault, the cut-off method was applied. This method is often used to see the presence of fault juxtaposition and membrane seals, such as creating the Allan diagram (Mulrooney et al., 2020). The cut-off lines represent the intersection of the horizons and the fault surface. In normal faults, the stippled line is the hanging wall cut-off, which lies under the solid footwall cut-off line. The cut-off lines automatically created in Move PETEX were quality controlled by avoiding any difficulties and uncertainties with the program. For instance, if one notices that the hanging wall cut-off lines are placed above the footwall cut-off lines, the interpreted horizons are not of good quality (too many errors) and need to be

revised. In this study's case, there were only a few places where the hanging wall cut-off line lay above the footwall cut-off.

After interpreting the cut-off lines, the throw values are calculated for each target formation and then converted to an Excel sheet, where I calculated the “missing fault tips” (Kim & Sanderson, 2005).

As previously explained in the

theory chapter, the seismic data cannot detect structures that are smaller than 15 m. Therefore, the interpreted F1 fault in the Aurora storage site is missing the fault edges assuming that the throw of a fault should gradually decrease to zero on each side. In the Excel sheet, the throw values are increased by 15 m (seismic resolution limit); thereafter, I calculated the linear gradient between the edge and the closest critical point on each side of the throw-value curve. Figure 4.5 illustrates the idea of “missing fault tips”, where the fault we observe in seismic data lies above seismic resolution (r), while in reality, the fault extends further on each end.

To assess whether the length of the fault is controlled by mechanical properties I calculated the “missing fault tips” in each interpreted horizon's throw value curve to observe any correlation of varying displacement in sandstone and shale.

Finally, the results from both physical analogue data and seismic interpretation will be compared including the across-fault seal evaluation from Holden et al. (2022). We will look at across-fault seal assessment from Holden et al. (2022) match with the sealing evaluation of the physical analogue data from Floy Canyon.

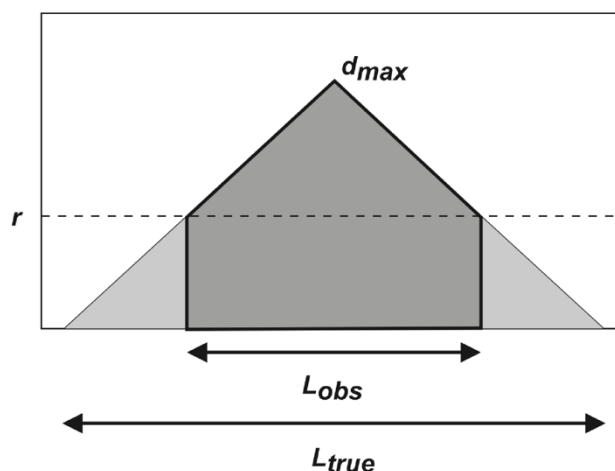


Figure 4.5 – Throw vs. Distance profile showing the concept of “missing fault tips”. Dark shaded area is seismically observed fault at resolution r . The observed fault length (L_{obs}) is much smaller than the true fault length (L_{true}). Figure from Kim & Sanderson (2005).

5 Results

This chapter presents the results of my findings and interpretations in two parts: (5.1) Floy Canyon as a case study of outcrop data and (5.2) seismic analysis of the F1 fault of the Aurora site. As mentioned, the overarching aim of this study is to compare the analogue fault dataset from the Floy Canyon with the F1 fault in the Aurora site: how well can these data forecast fluid migration?

5.1 Floy Canyon outcropping faults

In Floy Canyon, five faults were thoroughly studied: F1 in location 1 and four faults in location 2 (Figure 5.1). There are other normal faults in the study area, mapped in Figure 5.1; however, the studied faults are well exposed, allowing detailed analyses.

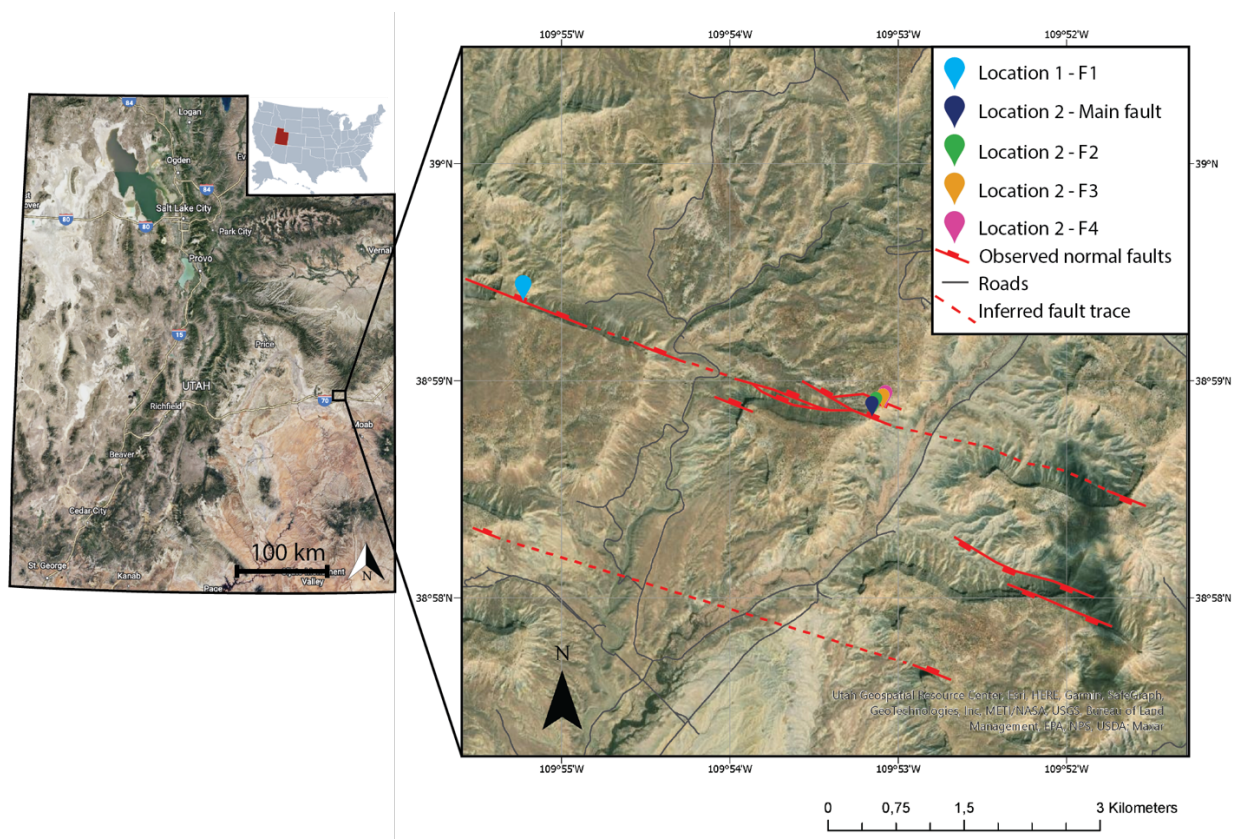


Figure 5.1 – Satellite image showing the Utah state (left), and a vertical view showing the study area of Floy Canyon (Utah, SW USA) with observed and inferred fault traces marked red. Locations of the studied faults are marked. Images are from Google Earth, 50states.com and ArcGIS Pro). Dirt-roads are indicated as dark grey lines.

Location 2 contains four of the studied faults: From south to north, the Main fault, F2, F3 and F4. They are displayed in the overview photograph of Figure 5.2. Logging of the sedimentary units also took place at Location 2 along marked trajectories A, B and C.

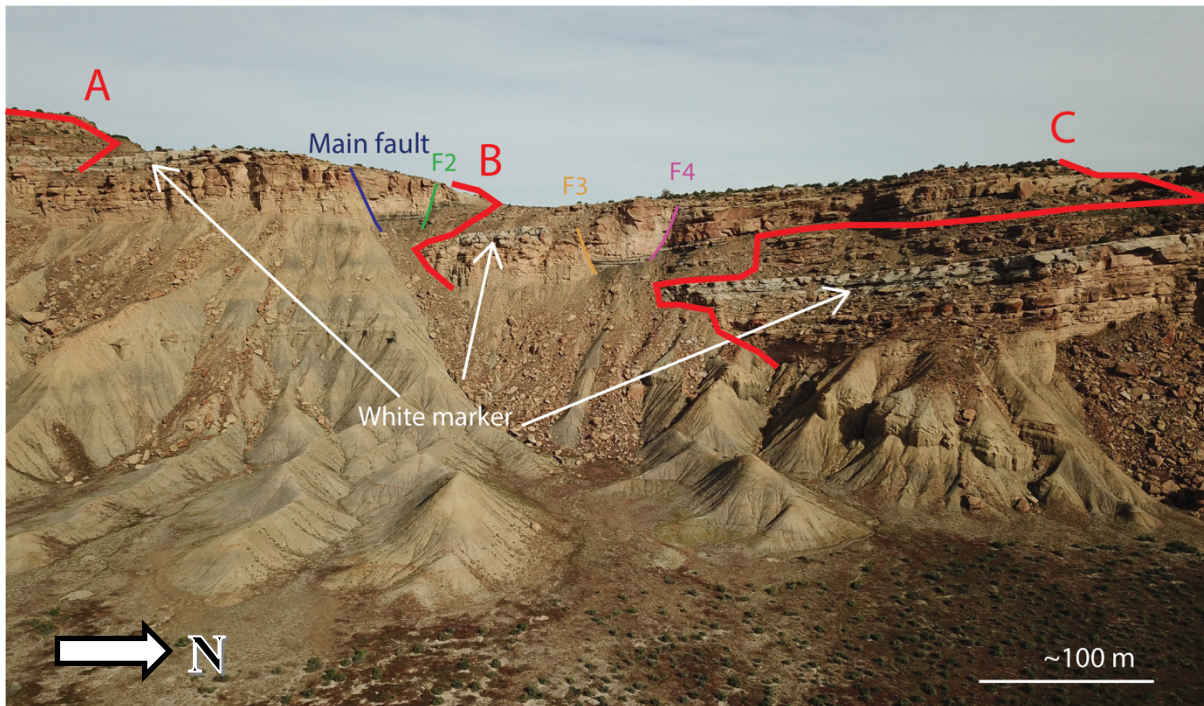


Figure 5.2 – Photograph showing the 4 faults of site 2 in the study area of Floy Canyon. Locations of stratigraphic logs are shown as red lines.

5.1.1 Facies description and interpretation

The sedimentary logging in Floy Canyon was conducted by supervisors Braathen and Bruhn. The logs display overall a prominent upward coarsening package overlain by an upward fining sequence, as part of the upper Cretaceous Blackhawk Formation. Detailed logs are presented in the Appendix, whereas a compilation figure 5.4 are included here.

The white bleached sandstone, referred to as the whitecap sandstone (see sub-chapter 2.1.2), is an important marker, which was used for across-fault correlation together with comparable stratigraphy, and hence allowed measurement of the throw of the larger faults (Main fault and F3). For each sequence and log, a net shale and mudstone/siltstone to gross sandstone have been calculated (shale content) to emphasize the percentage of sealing units relative to the succession. Throw and stratigraphy was used in the calculation of SGR.

All three logs (Figure 5.4 and Appendix) cover the whitecap sandstone marker. Logs display a variation of lithologies; most noticeably, on a larger scale there is much more coal in the Log

B trace than in Log A above the white sandstone marker, suggested to be related to growth-faulting (Braathen & Midtkandal, pers. comm. 2022). In the following, main units are described with an emphasis on sand-silt-clay distribution as a guide to fault facies descriptions, besides Net-to-Gross and SGR calculations. To simplify, the stratigraphy has been divided into four sequences that can be correlated in the area. They are termed Sequence I, II, III and IV, from base to top (Figure 5.4). With a focus on structural geology, each of these sequences are described as general facies belts. These facies belts are placed into a paleogeographic reconstruction, based in the detailed sedimentological work by Chan et al. (1991) and Walker (1984).

Sequence I: Upward coarsening succession (offshore to shoreface)

From 0-9 m in Log B and 0-28 m in Log C there are a prominent upward coarsening sequence (Figure 5.4 and Figure Appendix 2,3,4). The basal part of the sequence consists of laminated shale and mudstone, becoming siltier and sandier (very fine sandstone) upwards as the frequency and thickness of mostly massive siltstone to sandstone beds increase, some parts display extensive bioturbation. The upward coarsening sandstone beds with erosional surface at the base and cross-stratifications are interpreted as turbidite currents with indication of Bouma sequence (See Figure 2 and 3 in Appendix for better resolution). Figure 5.3, b illustrates how a turbidite can form, which is a gravity-based flow of amalgamated sediments that flows downwards on a slope (Chan et al., 1991). The presence of hummocky cross-stratification (HCS) (See Appendix) indicates episodic storm wave activity (Figure 5.3, b; Chan et al., 1991).

The lower part of the succession (Sedimentary log B; Figure 5.4; Figure Appendix 2) is interpreted as an offshore to shoreface prodelta unit (Figure 5.3, a) due to the combination of parallel-laminated siltstone and turbidites-style mudstone-sandstone bedding that become prominent upwards. A general shallowing into a lower shoreface environment is depicted by sandy beds hosting HCS, with diminishing signs of bioturbation. The succession is erosionally overlain by the previously mentioned mouth bar deposits.

The interpreted prodelta units are the most distal part of the delta, consisting primarily of mud settling out of suspension below the effect of waves and other types of currents (Allen & Chambers, 1998). Where there is an alternation of silt/mud and sandstone, thicker sandstone beds and hummocky cross-stratification illustrate shallowing upward in a middle shoreface environment, in which more wave energy occurs. The thick sandstone units of several meters

underneath the white sandstone marker have low angle trough cross-stratification and lateral, low-angle accretion observed at the Log A location, is interpreted as a mouth bar succession accumulated in front of a distributary channel (Figure 5.3, Appendix 1; Desjardins et al., 2012). I set the Net-to-Gross ratio (silt+shale vs. sand) for sequence I to be 30% because of the abundant sandstone beds. The NtG for shale in the prodelta unit in log B is 40 %, and for the prodelta – sequence II has a ratio of 5%.

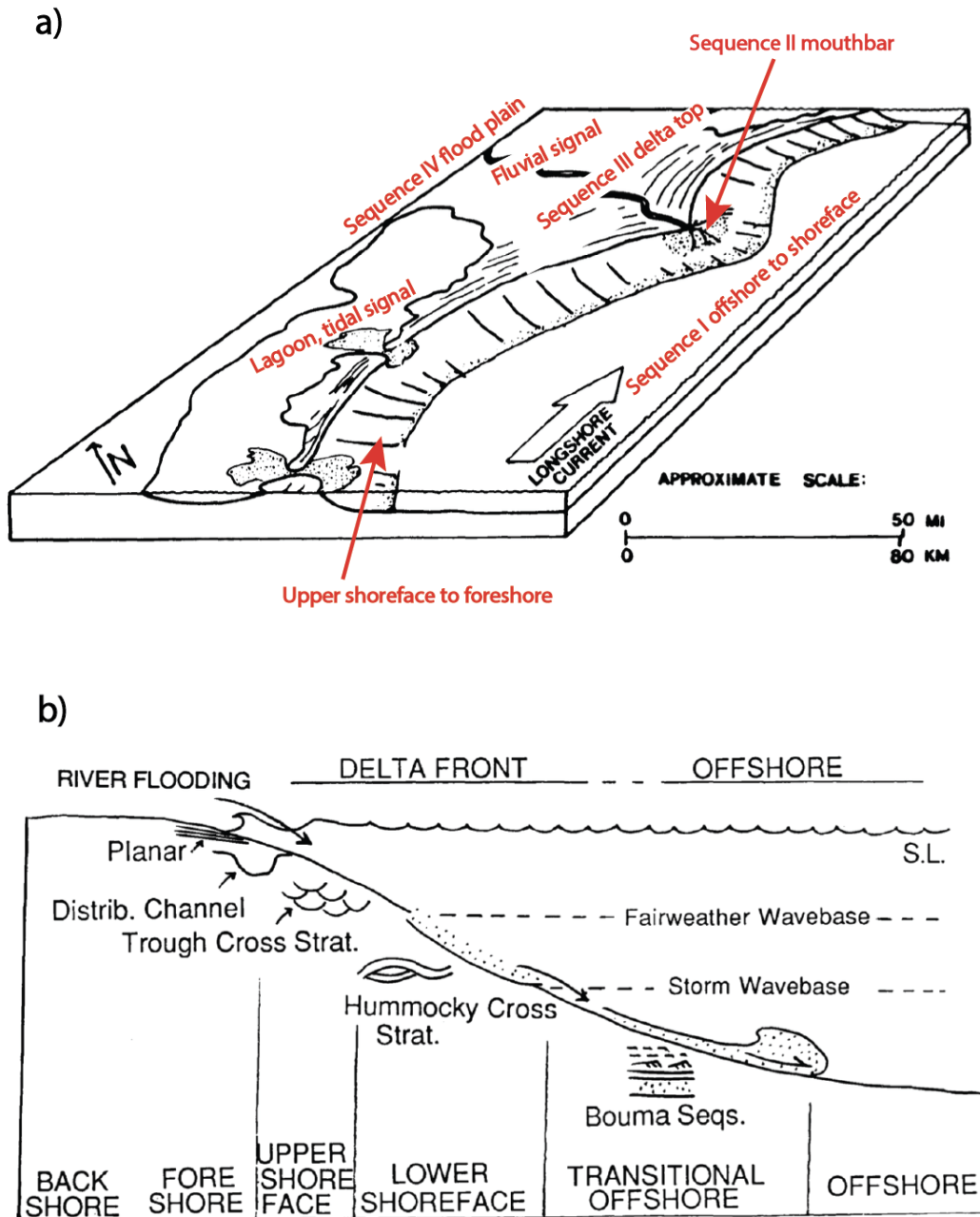


Figure 5.3 – (a) Paleogeographic reconstruction of Floy Canyon; Campanian regression (Grassy and Desert Members of the Blackhawk Formation). Illustrating the delta environment with labels. Figure modified from Chan et al. (1991). (b) Depositional environment showing sedimentology facies model

for the wave-dominated delta system of Blackhawk Formation. Figure from Chan et al. (1991) after Walker (1984).

Sequence II: Thick white sandstones and associated units (mouth bar)

The white sandstone marker displays low-angle trough cross-stratification in a well-sorted fine-medium sandstone sitting on an erosive base with more than 1-m relief in places (Figure 5.4). Bioturbation is rare. Some coal and clay drapes were observed on the foresets and bottom sets, as shown in logs A and B, which is interpreted as a tidal signal. The sandstone body thickness varies from 1 to 12 m, suggesting it holds a lenticular shape (channelized) and/or vary between foot- and hanging walls. The sandstone is located between plane-laminated siltstone and mudstone (sequences 3), or accretional sediment infill of sandstones or more heterolithic substrata (log C). Some of these units are significantly bioturbated, consistent with a shallow marine (sub-aquatic), protected environment with oxic bottom conditions (most likely a lagoon, low-energy periods in distributary channels, delta top sandy channel splays and other overbanks on the delta plain).

The white sandstone with its associated units is interpreted as a bleached mouth bar, a typical deltaic system element, which is most likely related to organic acid coming from the overlying coaly strata deposited on the deltatop (e.g. Bailey et al., 2022). In Figure 5.3, the delta environment is depicted and labelled, considered a viable case for the unit (mouth bars are elevated part over sea level, where sediments of a river enter a standing body of water and deposit, in this case the ocean (Edmonds & Slingerland, 2007). The Net-to-Gross ratio of shale is 0%; however, there are observed mudclast and coal drapes within sequence II.

Sequence III: Heterolithic fine-grained units (delta top or intertidal flat)

Above the white marker, the siltstone and coal alteration (shown in Logs A and B in Figure Appendix 1-2 and Figure 5.4) are interpreted in terms of deposition in a delta top environment, potentially an intertidal flat: the area between high- and low tide levels in a lagoon (Figure 5.3). Where there are coal-rich shale layers (heterogeneous mix of shale and coal) and root traces, these are interpreted to represent a coastal plain swamp or lagoonal environment (Chan et al., 1991). The uppermost section of Log A and B contains a thicker sandstone with bioturbation and siderite cemented nodules and some rip-up clasts at the bottomset, which are interpreted to represent a fluvial channel or point bar. The Net-to-Gross ratio (NtG) for shale in the sequence III deltatop above the white marker has a ratio of 73% in log B and 52% in log C.

Log C (Figure 5.4 and Appendix 3-4) further up in the stratigraphy, where Figure Appendix 4 shows several meter-thick sandstones with loads of rip-up mud clasts at the bottom sets. Large-scale high-angle bed sets and trough cross-stratification are present. This is interpreted as a river channel belt, similar to the uppermost portion in Log A and B.

Overall, the clean sandstone units consist of well-sorted fine to medium-sized grains and can be interpreted as a good reservoir rock. In the SGR calculation, the units coal, coal-rich shale, mudstone, coaly siltstone and siltstone will be counted as sealing units, contributing to the SGR sealing probability.

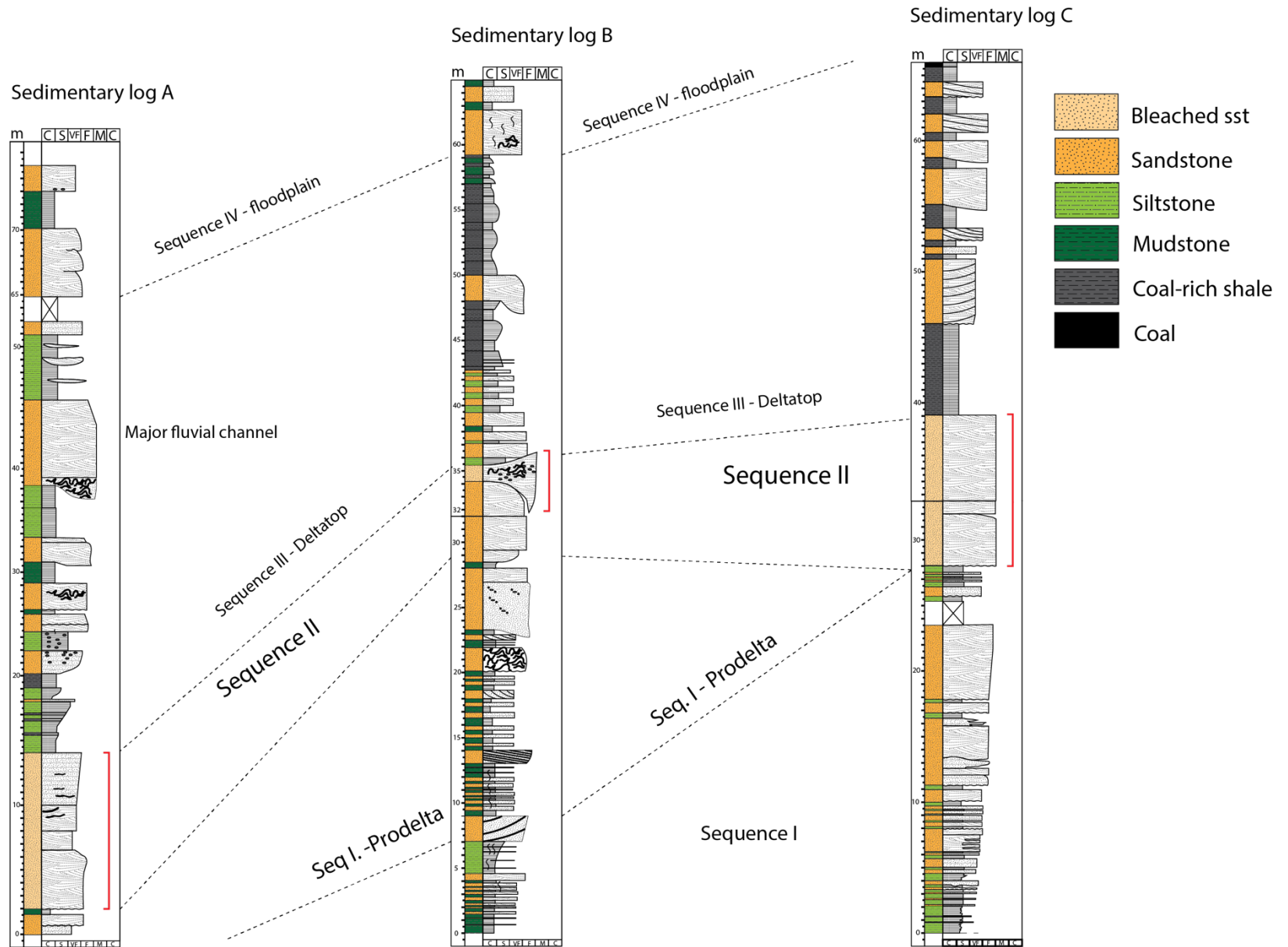


Figure 5.4 - Stratigraphy has been divided into four sequences that can be correlated in the area. They are termed Sequence I, II, III and IV. See Figures in Appendix for more details and better resolution in each log.

5.1.2 Fault facies descriptions and interpretations

This sub-chapter will present the interpreted fault facies structures in each of the studied faults in Floy Canyon. Table 5.1 summarize the hard data collected from the faults in Floy Canyon, which includes coordinates, throw measurements, observed membrane types (M-type), lens type (L-type) and the continuity of the principal slip surface. Sub-chapter 4.1.3 explains the methodology of the interpretation.

The burial depth for the faults in Floy Canyon cannot be extracted from the literature. However, if the postulated fault growth wedges (syn-rift) in the Floy Canyon system are real (Braathen & Midtkandal, pers. comm., 2022), they indicate that faulting took place while the burial depth was shallow, within meters to maximum 100 m from the earth's surface. Hence, the fault formed in poorly to un-consolidated sediments (Bhattacharya & Davies, 2004; Braathen et al. 2018). Burial depth influences enveloping stresses during deformation, and hence the style of deformation that can be expected (e.g., Fossen 2007; Braathen et al. 2013).

Table 5.1 – Summary of fault element data recorded from the five analyzed faults in Floy Canyon. Coordinates marked “Fat map” are coordinates measured with the help of Fat Map (fatmap.com) to get better precision. The throw values marked “physical” are measured physically on the fault, while the throw values marked “illustrator” is measured using drone pictures and measured scale on the fault. The fault core width marked with (*) is the core width that varies along the plane. Abbreviations: M type = membrane type; L type = lens type

Name	Coord	Units	Lithification	Throw (m)	Fault Core width	M type	M-type continuity	L type facies	Type of network shears	Principal slip-surface continuity	Juxtaposition	Strike/dip
Location 1 F1	38°59'23.0"N 109°55'14.2"W	Sandstone, coal, silt, mud (both HW and FW)	poor to medium	2.3 (physical)	15 cm*	Mt2, Mt3, Mt6	Semi continuous coal smear	LtC, LtD	Dragged	Not continuous	All units juxtapose against each other	259/60 260/52
Loc 2 main fault	38°58'50.0"N 109°53'09.3"W	FW: Mix of mud-silt and sst. HW: sst and mix of coal and mud	poor to medium	58 (illustrator)	50 cm	Mt1, Mt2, Mt3, Mt6	Ruptured	LtA, LtC	LtC: dragged LtA: not noticeable	Continuous	All units juxtapose against each other	278/64
Loc 2 F2	38°58'50.9"N 109°53'09.7"W	Mud-silt, mix of coal and mud and coal (both HW and FW)	poor to medium	6,5 (illustrator)	5 cm	Mt1, Mt2, Mt3, Mt6	Continuous	LtC, LtD	LtC3: Open network shears. LtD: Dragged	Continuous	Semi self juxtaposition	105/55
Loc 2 F3	Fatmap: 38°58'52.3"N 110°6'54.4"W	FW: Mix of mud-silt HW: mix of coal and mud	poor to medium	41.5 (illustrator)	10-30 cm*	Mt1, Mt2, Mt3, Mt6	Continuous	LtC	Dragged	Continuous	All units juxtapose against each other	272/59
Loc 2 F4	Fat map: 38°58'53.1"N 110°6'55.2"W	FW: sst, mud-silt, coal, mix of coal and mud. HW: sst, mix of coal and mud	medium	4.5 (illustrator)	20 cm*	Mt1, Mt3, Mt6	Patchy	LtA, LtC	Open network shears and dragging	Not continuous	Self juxtaposition and juxtaposition seal	100/68

Location 1: Fault 1 – Interpretation

Fault F1 has a calculated throw of 2.3 meters. Although there is some dirt cover, the gross geometry of the fault can be seen. Stippled lines likely represent the primary slip plane and appears well located. Accurate, touchable observations start from the middle half and downward of the fault, as shown in Figure 5.5, inset A2. Overall, the main fault plane is not continuous; it steps from the hanging wall to the footwall side downwards.

The fault core contains a mudstone lens (LtB) and a very sheared coal lens giving way to a silty lens (LtD) (Figure 5.5, A2). Especially coal lenses are disintegrated by swarms of small shear fractures, giving the appearance of ductile smearing along the main slip surface. There are however remnants of the original bedding structures.

For F1 in Figure 5.5, A2, most of the LtD could not be reached and other elements are partly covered by the dirt. Therefore, the coal smear was observed along lower part of the fault (red line), with an unknown continuity upwards.

The F1 fault appears in several windows of outcrops, displayed in inset figures A1, A2, B1 of Figure 5.7, situated at lower stratigraphic levels. In Figure 5.5, B2, a continuous coal smear, a non-continuous silt gouge and a sand gouge are identified. This outcrop allows a 3D view of the bounding wall rock sandstones, showing a sand gouge membrane bounding the wall rock; this membrane is characterized by a very fine grain size (silty) and besides discoloration, and appears continuous. There is also a discontinuous silt-gouge membrane that could be interpreted as a disintegrated sandstone fault rock (gouge), or alternatively as a silt smear. This membrane has greyish color and locally some bleached silt, seen along the slip plane. A black membrane (3cm thick) lies on top of the silt gouge and consists of very fine coaly shale gouge.

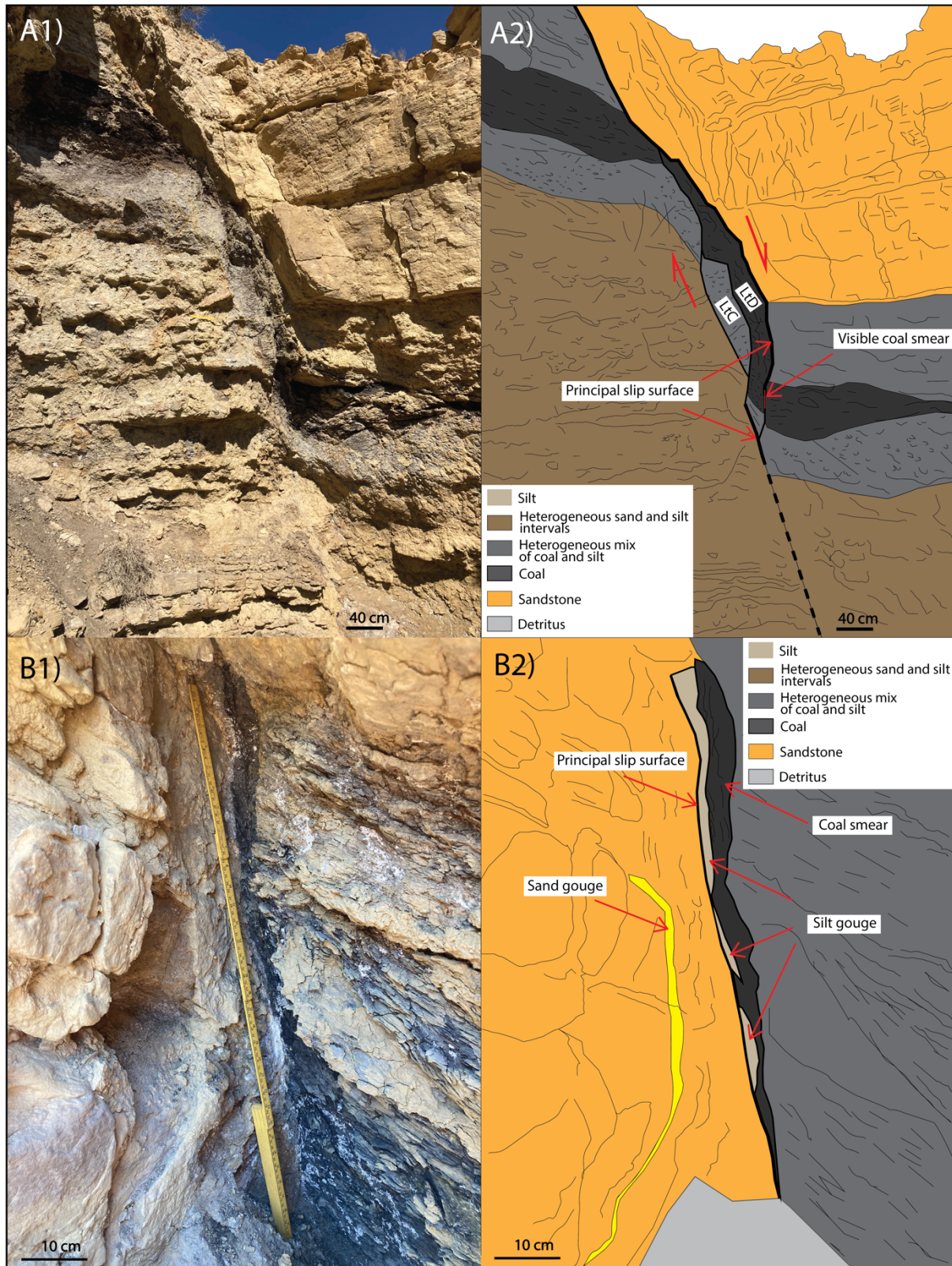


Figure 5.5 – Photographs and fault facies interpretation sketches of the F1 fault in location 1; see Figure 5.1 and table 5.1 - for location and coordinates (A1) Photograph of F1, with the physically measured throw of 2.3 m. (A2) Sketch of picture A1 of the interpreted fault facies. Principal fault plane is not continuous. Red movement arrows show the relative fault movement. The interpretation is most accurate at the lower half of the illustration. (B1) Photograph of F1 in location 1 lower down in the stratigraphy. (B2) Sketch of B1 with more visible membranes. Continuous coal smear, silt gouge and sand gouge are

present. Code used on lenses: LtC= lens type consisting of a mix of coal and silt, LtD = coal lens (Photographs and illustrations by Victoria Kjeldstad, September 2022).

Main fault (MF)

The Main fault, MF, is location 2's southernmost fault. Offset stratigraphy allows calculation of throw to 58 meters. Outcrops show a maximum fault core width of 50 centimeters. Fault MF is illustrated in Figure 5.6. The interpretation of the fault is most accurate in the lower portion, where the fault was touchable.

The principal slip surface is continuously bounded to the hanging wall. The black stippled line represents a slip surface but is not visible because of the dirt cover; uncertain where precisely the slip surface is located.

The fault core contains pulverized, very damaged yellow and bleached (white) sandstone lenses with very little original structure left to observe, such as the yellow sandstone lens and the lowest bleached lens (Figure 5.6, A2). The dark interpreted lens is made of a heterogeneous mix of coal and mud, but mostly coal dragged and sheared but still containing some of the original bedding structure.

Thin coal smears are observed at the interfaces of lithologies and slip lines in multiple instances. However, due to the presence of dirt cover, it remains unclear as to the extent of continuity of the coal smear. The blue boxes show close-up photographs of more detailed structures of the fault core.

Figure 5.6, B is a close-up photo of the breccia mix of sandstone and coal silt with continuous coal smear along the slip surface at the boundary between the breccia mix and coal-silt lens. Figure 5.6, C provides a close-up view of three distinct slip lines, each separated by a membrane of either coal smear or two gouge layers, occurring at the boundaries of lithologies that vary significantly from each other. The continuity of the interpreted membranes is unknown because of the dirt layer covering the outcrop. Figure 5.6, D show a close-up of a more complex area of slip surfaces merging and the occurrence of smaller slip lines we could not trace. Coal smears are visible with displacements, and the upper portion of the photograph shows silt-coal and sand gouge.

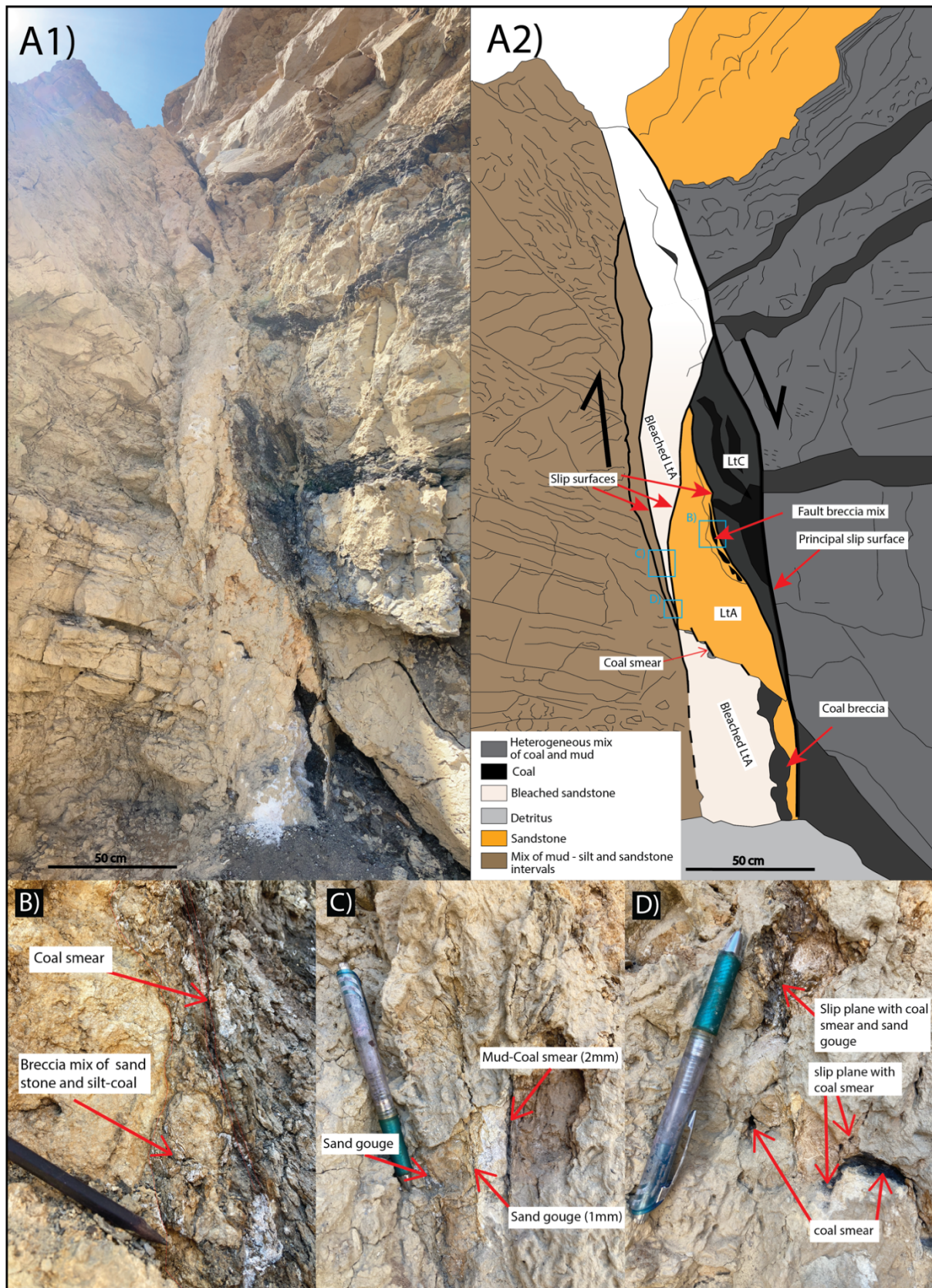


Figure 5.6 - Photographs and fault facies interpretation sketches of Main fault in location 2; see Figure 5.1 and table 5.1 for location and coordinates (A1) Overview Photograph of the southernmost fault in location 3, the main fault strand with the largest throw of 58 m. (A2) An illustration sketch of picture A1. Be aware that the picture is taken from the ground facing up, and the scale only counts the lower

half of the illustration. The interpretation of the fault is most accurate lower portion of the illustration, where the fault was touchable. Black arrows show the relative fault movement. The principal slip surface is continuous and located on the hanging wall of the fault. Box B, C and D are close up photographs of different small-scale membrane structures of the fault, where location of the boxes is shown in A2. Code used on lenses: LtA= lens type consisting of sandstone; LtC= lens type consisting of a mix of mud and coal (Photographs and illustrations by Victoria Kjeldstad, September 2022)

Fault F2 – Overview and box B

Figure 5.7 depicts photographs and fault facies interpretation sketches of the second southernmost fault F2 in location 2, with a throw of 6.5 m. In Figure 5.7, A2, a sketch of Picture A1 is presented, wherein the fault core of this fault appears to be comparatively thinner than the fault cores of other faults examined. The principal slip-plane is continuous, bounded to the footwall.

There is one prominent lens on the lower part made of a heterogenous mix of mud and coal, where the differences in lithology in the hanging wall on the left side to the lens is noticeable enough to see the shape of the lens. This lens is noticeable despite the lack of distinct slip surfaces on the boundaries of the lens and the dirt cover that cover a wide area on the hanging wall. There are two very elongated and sheared coal lenses (LtD) and a mix of coal and mud lens (LtC). Although observed in the field, the membrane represented by the red line is too small to be depicted in the figure. The B and C boxes are chosen close-ups photographs of the fault to show more details of the fault core and the lenses.

Figure 5.7, B1 features a close-up photograph of the fault core, which corresponds to box B in the overview illustration presented in A2. Figure 5.7, B2 presents an illustrative sketch of Picture B1, wherein the fault core depicted in this close-up view is composed of the aforementioned, heterogeneous mixture of mud and coal lens, which displays bookshelf shear slip planes. This lens could also be interpreted as individual smaller LtCs because of the displacement of the dextral bookshelf shears, which also can be interpreted as slip-planes. A smaller lens was also observed on the right-side corner of Figure 5.7, B2, which is interpreted as an oxidized silt lens. The LtB lens had a more intact structure, with rusty colour and fractures, but was not inherently crushed.

The red polygon in Figure 5.7, B2 represents an interpreted silt gouge because of the comminuted material and its very small grain size. The interpreted proto breccia had a high degree of crushed mud-silt material compared to the adjacent LtC, which led to the conclusion that this membrane is closer to being a breccia.

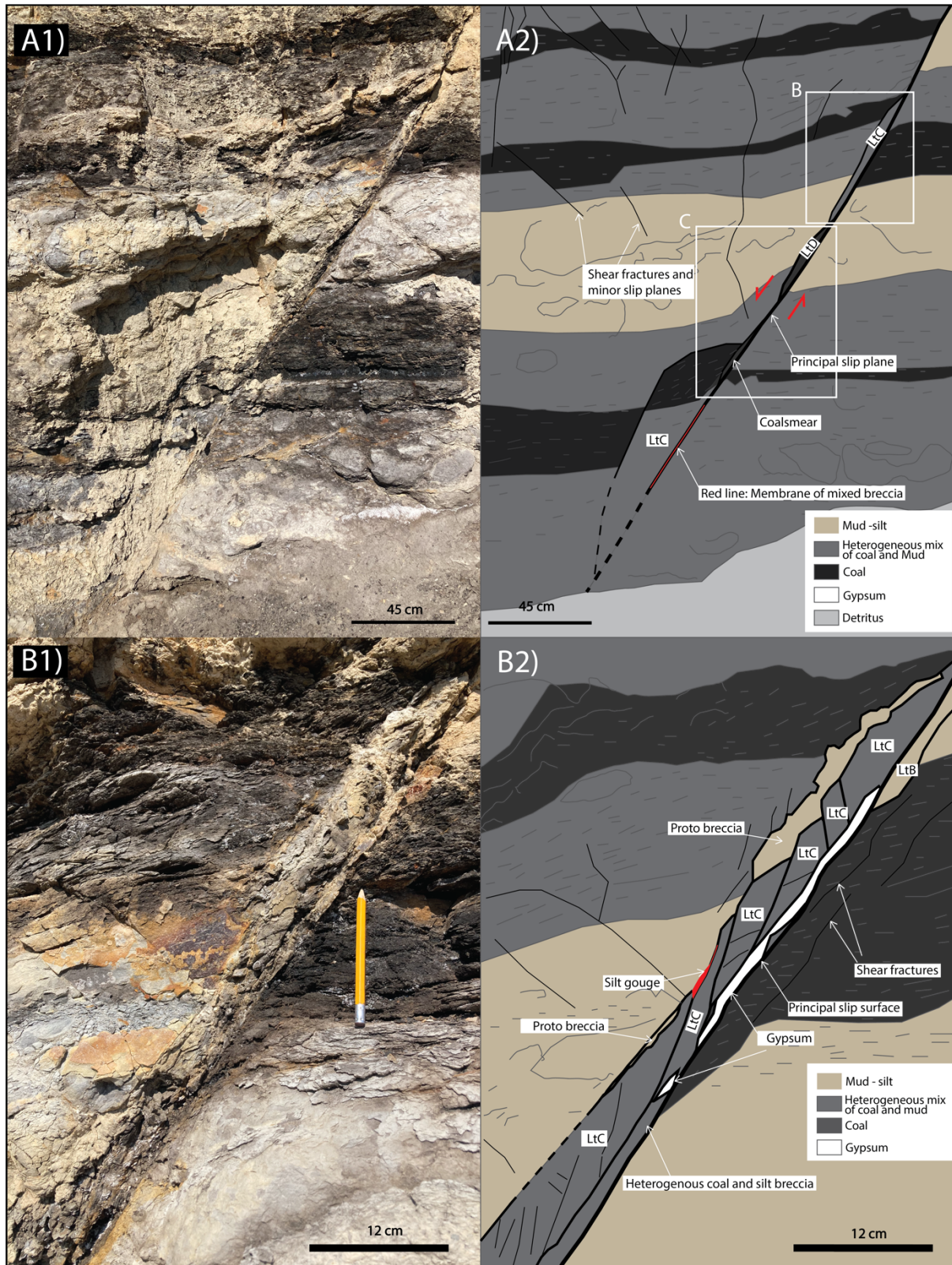


Figure 5.7 - Photographs and fault facies interpretation sketches of F2 in location 2; see Figure 5.1 and table 5.1 for location and coordinates. (A1) Overview Photograph of F2 (A2) Illustration sketch of picture A1, illustrating continuous principal slip-plane, self-juxtaposition, three lenses; 2 LtC and LtD. Red arrows illustrate the sense of fault movement. Shear fractures with displacement are observed in the hanging wall. (B1) Close-up photograph of the F2. Location is shown in A2. The LtC lens is made up of heterogeneous mix of coal and mud and is separated by bookshelf shears with displacement.

Gypsum and silt gouge were observed. Code used on lenses: LtC= lens type consisting of a mix of mud and coal; LtD= coal lens (Photographs and illustrations by Victoria Kjeldstad, September 2022).

Fault 2 – Lower part – Box C

Figure 5.8, C1 features a close-up photograph of the fault core, which was captured at the location depicted in Figure 5.7, A2.

The coal lens (LtD), on the contrary, is interpreted as having some of the original bedding structure, although the lens is heavily sheared and dragged, which is not far away from being interpreted as a smear.

Figure 5.8, C2 presents an illustrative sketch of Picture C1, depicting the fault core composed of interpreted coal smears and very fine, ductilely dragged textures with no original bedding structure to be seen.

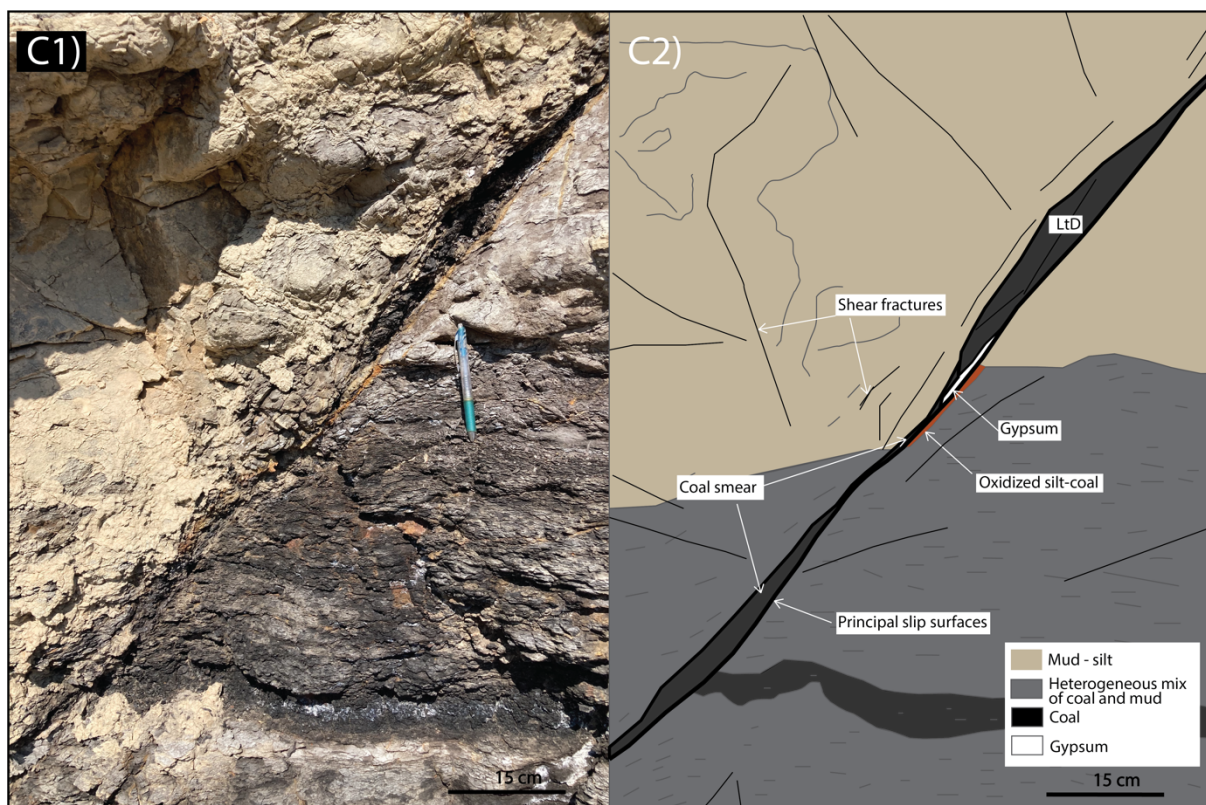


Figure 5.8 – Close- up photograph and fault facies interpretation sketch of F2 in location 2; see Figure 5.1 and table 5.1 for location and coordinates. (C1) Close-up photograph of F2 (Box C in Figure 5.7, A2). (C2) Fault facies interpretation of C1. The principal slip-plane is continuous and there are observed and interpreted lower coal smear and upper LtD. Code used on lenses: LtD= coal lens (Photographs and illustrations by Victoria Kjeldstad, September 2022).

Fault F3 – upper part

Figure 5.9, A1 shows a photograph of F3 in location 2. Figure 5.9, A2 is a fault facies interpretation sketch of picture A1, where we can observe a continuous principal slip surface on the footwall of the fault.

The F3 fault in Figure 5.9, A2 consists of a prominent upper LtC lens with dragged layers of coal and a heterogenous mix of coal and mud. The lower LtC lens is mainly made of coal, though there are silt pieces within, which make the lens partly heterogeneous.

This fault consists of throughgoing continuous membranes along the principal slip surface. The continuously connected membranes are composed of heterogenous breccia in the lower part (shown in Figure 5.10, C2) and an upper coal smear (shown in Figure 5.10, B2).

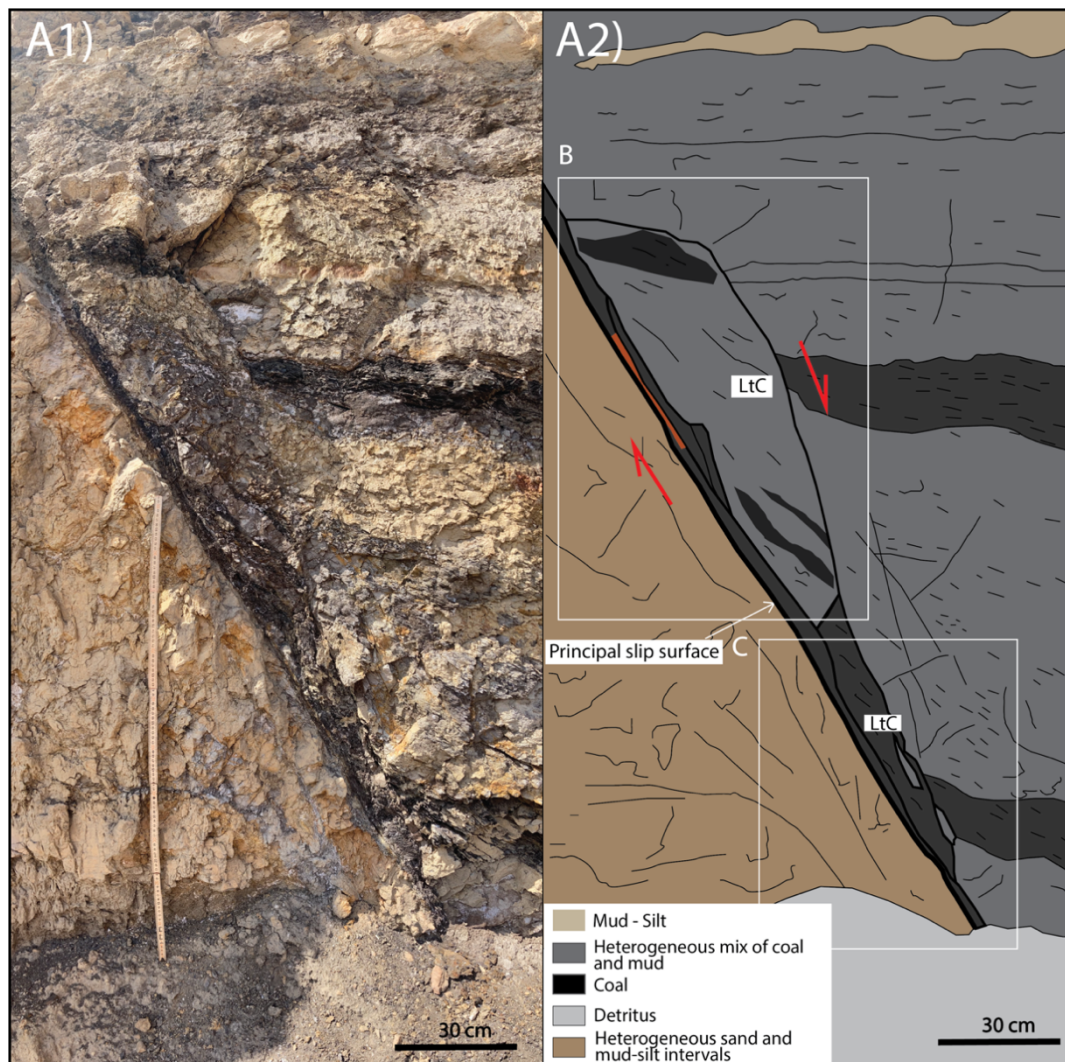


Figure 5.9 - Photographs and fault facies interpretation sketches of F3 in location 2; see Figure 5.1 and table 5.1 for location and coordinates. (A1) Overview Photograph of F2 (A2) Illustration sketch of picture A1. Red arrows illustrate the sense of fault movement. The principal slip-plane is continuous with continuous membranes on top. There are two prominent LtCs, where the lower one is mainly made of coal. Code used on lenses: LtC= lens type consisting of a mix of mud and coal (Photographs and illustrations by Victoria Kjeldstad, September 2022).

Fault F3 – Box B and C

The LtC lens in Figure 5.10, B1 is made of layers of coal and a heterogenous mix of coal and mud. Figure 5.10, C1 shows a photograph of the lower part of the fault, which is shown in Figure 5.9, A2, box C. The LtC lens is made of coal and contains silt pieces, which can be interpreted as individual smaller silt lenses. Since the coal lens is heavily ductile and deformed, fragment pieces such as the smaller silt lenses can be dragged in.

Figure 5.10, B1 shows a close-up photograph of box B in illustration A2 in Figure 5.9. Figure 5.10, B2 depicts an interpretation sketch of Photograph B1, providing a more detailed view of observed structures, such as the silt-sand breccia containing grain clasts and unevenly comminuted material. A heterogenous breccia is also observed, which has parts of brown oxidized coal silt. The illustration presented in Figure 5.10, B2, displays a membrane of a heterogeneous breccia overlaying the coal smear. Initially, these structures were thought to be part of the LtC lens, but upon observing slip planes and comminution structures within the breccia, they were distinguished as separate structures.

Figure 5.10, C2 shows an illustration sketch of photograph C1 where the continuous heterogenous breccia on top of the principal slip surface contain distinct silt clasts and oxidized coal-silt layers. Two oxidized coal-silt gouges were observed, and another heterogenous breccia was on top of the oxidized gauges.

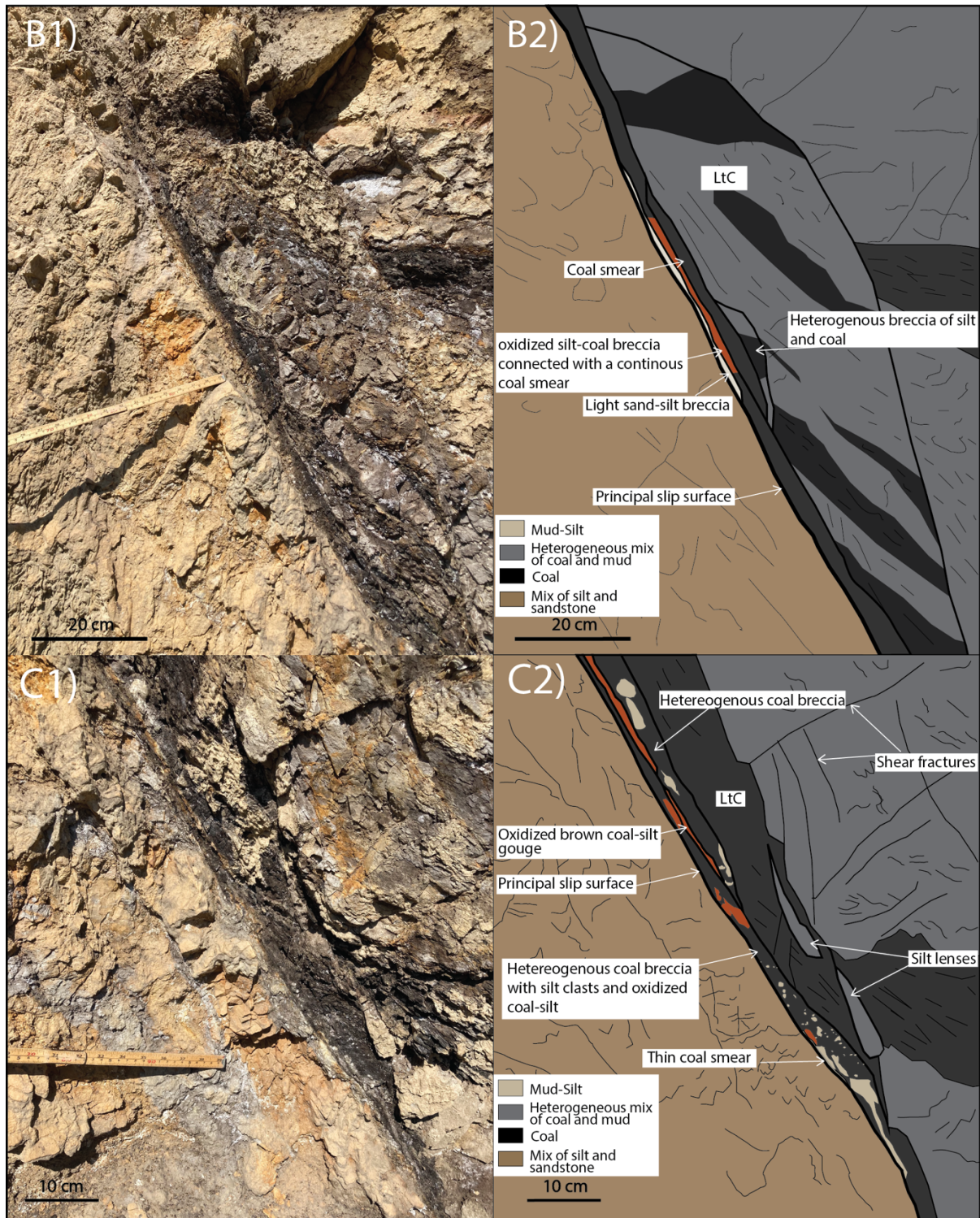


Figure 5.10 – Close up photographs and fault facies interpretation sketches of F3 in location 2; see Figure 5.1 and table 5.1 for location and coordinates. (B1) Close-up photograph of F2 (Box B in Figure 5.9, A2). (B2) Illustration sketch of photograph B1. Close up of the stacked membranes underlying LtC lens. The continuous coal smear is connected with the oxidized silt-coal breccia and transition to coal smear on the way up along the fault plane. (C1) Close-up photograph of F2 (Box C in Figure 5.9, A2). (C2) Illustration sketch of photograph C1. Close up of the continuous stacked membranes with coal breccia with silt clasts. Code used on lenses: LtC= lens type consisting of a mix of mud and coal (Photographs and illustrations by Victoria Kjeldstad, September 2022).

Fault F4 – Overview

Fault 4 is the northernmost fault in location 2 with a 4.5 m throw and contains the most complex fault facies structures out of all the studied faults in Floy Canyon. An overview picture of F4 is depicted in Figure 5.11, A1, while an illustrated sketch of the same image is presented in A2. All the interpretations from box B and downwards in the fault are the most accurate and detailed because of the possibility of getting close and touching the outcrop. Above box B are interpretations based on observations from a distance and pictures from the drone.

The mentioned fault contains a noncontinuous principal slip surface, which jumps from HW contact to the right side of the lowest sand lens. The area between where the principal slip surface jumps from the hanging wall to the yellow proto breccia was very hard to trace, therefore leaving a gap of no traced principal slip plane. The complexities of the fault with sand and silt-shale lenses and mixed breccias are shown where the principal slip surface starts to jump, making it chaotic to distinguish all the structural elements, making this fault the hardest to interpret of all five studied faults in Floy Canyon. The position of the fault core's detailed photographs and illustrations can be observed in Figure 5.12, which are represented by boxes B and C in Figure 5.11, A2.

There are six lenses observed in total, where the lower lenses LtA and LtC contain prominent fracture shears, and the upper LtC seems to display more ductile shear. We can also observe a drag in the lower heterogeneous mix of coal and mud unit in the hanging wall.

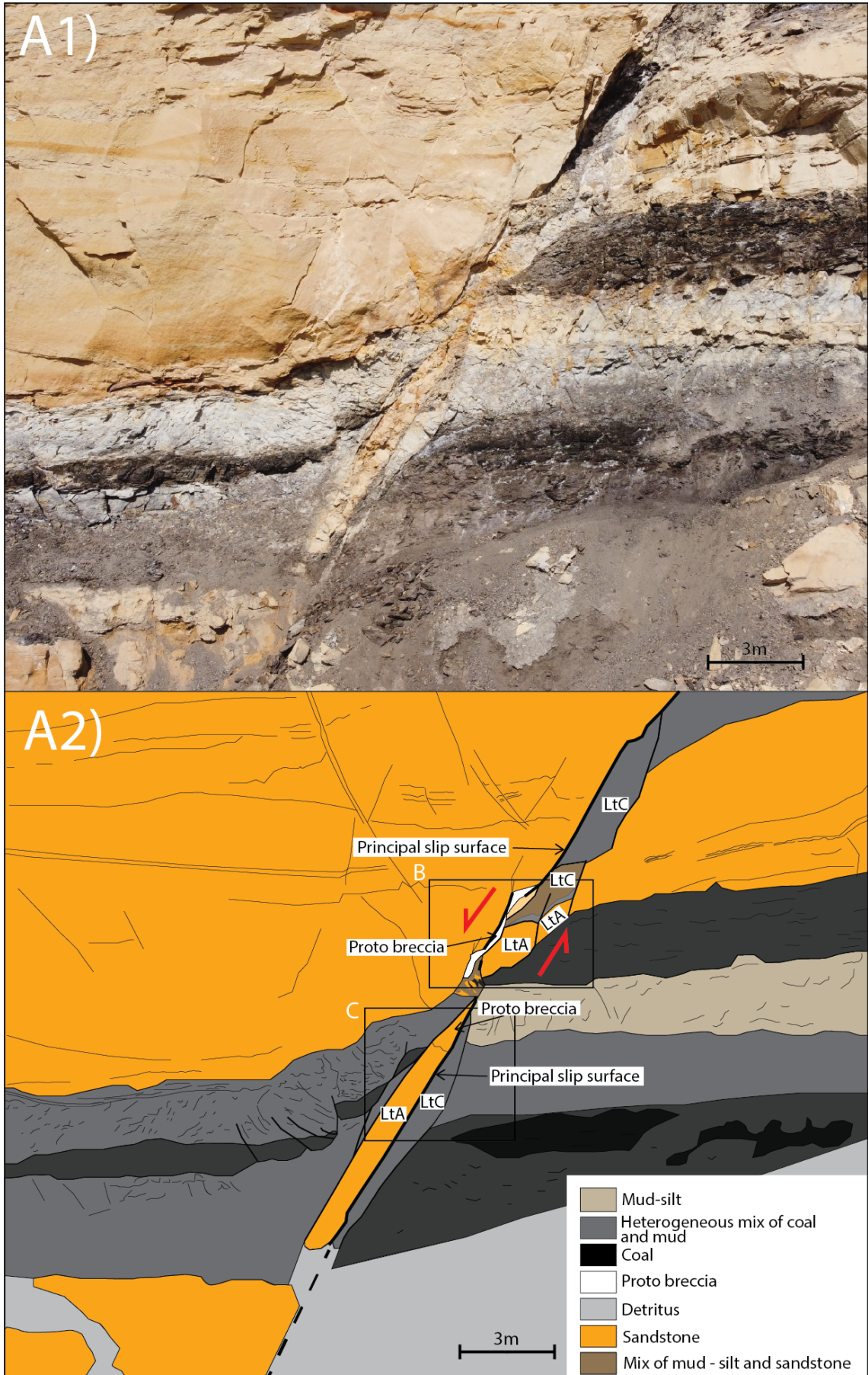


Figure 5.11 - (A1) Photograph of the northernmost fault with a throw of 4.8 m. (F4) in location 2. (A2) An illustration sketch of picture A1 shows a noncontinuous principal slip surface, which jumps from HW contact to the right side of the lowest sand lens. All the interpretations from box B and downwards in the fault are the most accurate and detailed because of the possibility of getting up close. Above box B are interpretations based on observations from a distance and pictures from the drone. Code used on lenses: LtA= lens type consisting of sandstone; LtC= lens type consisting of a mix of silt and sandstone (Photographs and illustrations by Victoria Kjeldstad, September 2022).

Fault F4 – Box B and C

Figure 5.12 portrait close-up photographs and fault facies interpretations of F4 fault, where the location of the where the pictures were taken are shown in Figure 5.11, A2 (Box B and C). Figure 5.12, B2 illustrate the fault facies sketch of photograph B1, the upper close-up photo of F4. The photograph in Figure 5.12, C1 shows the lower portion of the F4 fault, and an illustration sketch of photograph C1 is depicted in Figure 5.12, C2.

The damage zone of the sandstone in the Hanging wall shows a dense network of mild shear compaction cataclastic and disaggregation bands. Shear mild compaction cataclastic bands form by shear grain grinding, which crushes the grains into smaller pieces, while disaggregation bands form by shear grain rolling and rearrangement of the grains (Fossen et al., 2007). The coal bed in the Footwall is heavily dragged and thinning close to the fault core (drag fold).

The LtC lens in B2 is heavily dragged and fractured as well as the bedding is almost vertical and parallel to the fault plane. The upper portion of the LtA sand lens in C2 consists of proto breccia, which is made of comminuted sandstone. We can clearly see the distinctive bookshelf shears in the sand lens formed by the dextral shearing from the fault parallel slip surfaces on both sides of the fault lens.

The lower breccia in B2 is made of a mix of loose fragments of coal and sandstone, while the white proto breccia is made of bleached comminuted sandstone. The upper red line in C2 on the right side represents a visible part of a white 2 mm gouge most likely made of silt, while the lower and the upper left red line is a visible coal smear membrane.

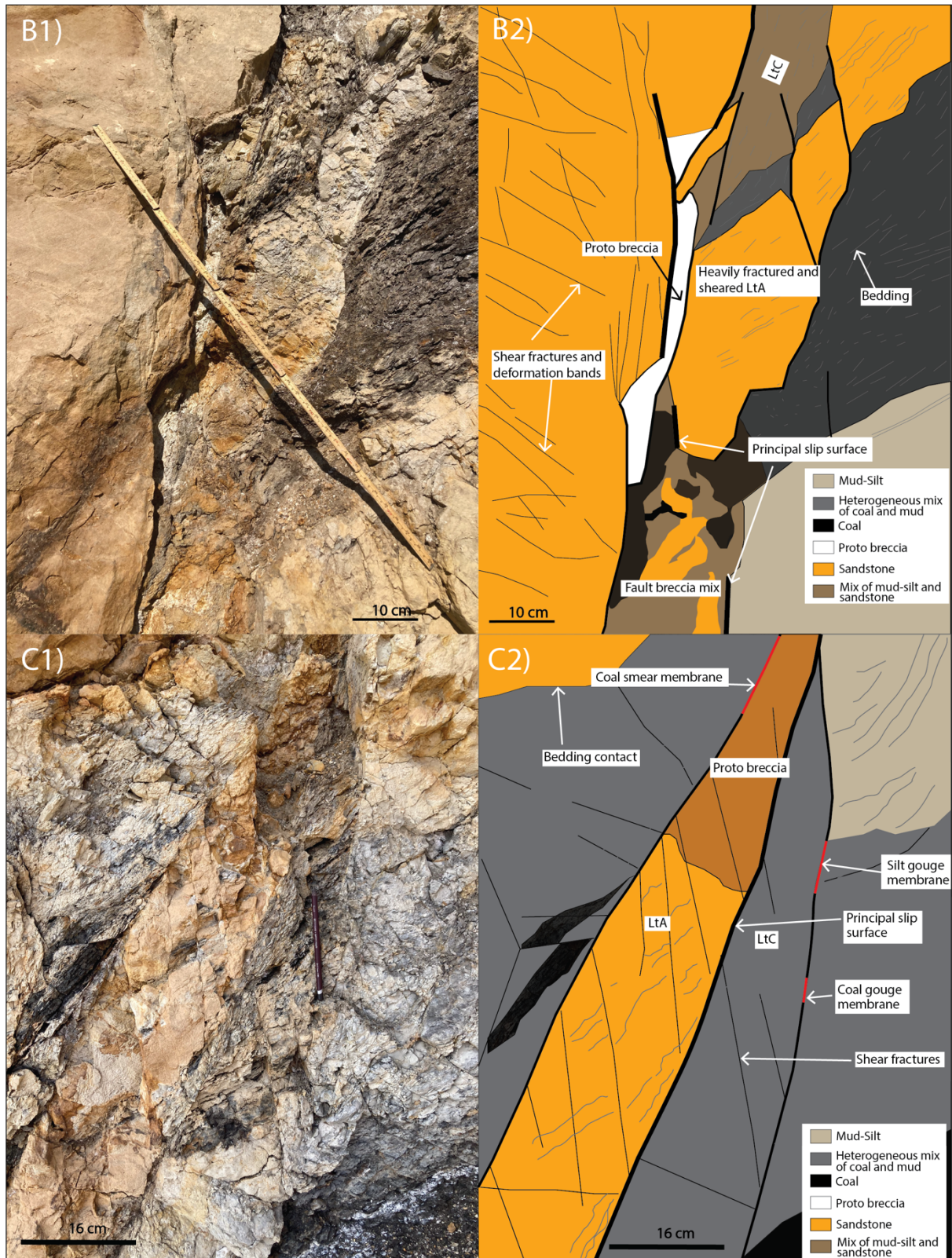


Figure 5.12 – Close up photographs and fault facies interpretation of the northernmost fault (F4) in location 2. See Figure 5.11, A2 for locations of where the photos were taken (Box B and C). (B1) Close-up photograph of upper portion of the fault (Box B). (B2) An illustration sketch of picture B1. Heterogeneous breccia is made up of sandstone, mud-silt and coal. The proto breccia is made up of bleached sandstone. Notice the big gap between the principal slip plane on the HW and the lower

principal slip on the lower part adjacent to the fault breccia mix, although there is an interpreted short slip plane in between that indicate the trace of the principal slip plane. (C1) Close-up photograph of lower portion of the fault (Box C). (C2) An illustration sketch of picture C1. Open network shears in LtA and LtC. The principal slip plane is interpreted in between the two lenses. The upper portion of the LtA was very crushed and deformed, which led to be interpreted as a proto breccia. Few observations of thinner membranes along the slip-surfaces, which were not continuous. LtA= lens type consisting of sandstone; LtC= lens type consisting of a mix of silt and sandstone (Photographs and illustrations by Victoria Kjeldstad, September 2022).

5.1.3 Net-to-Gross and SGR calculations

The NtG ratio (shale content) varies laterally in sequences I, II, III and IV and will, therefore, also vary in each of the fault sections, depending on where the fault is cutting. As previously stated, the NtG ratio for sequence I is 30%, II is 0%, and sequence III deltatop, fluvial signal has 40 %, and for the deltatop, tidal signal has 5%. The sequence III above the white marker has an average NtG ratio of 63%.

The Shale Gouge Ratio were calculated for on one point in each of the studied faults in Floy Canyon (Table 5.2), in accordance with methods of chapter 3.3.2 (Equation 3.5). The sedimentary logs, A, B and C, were crucial when calculating the SGR value for the faults with the largest throw (i.e. Main Fault and F3). The calculation covers the sum-thickness of all the units that count as sealing (i.e. coal, coal-rich shale, mudstone, coaly siltstone and siltstone). The measured SGR point is approximately located on the fault plane. The results show SGR values varying between 0,4 and 1, with larger throw offering the lowest values. In the Discussion (Chapter 6), SGR values and sealing considerations are further addressed.

Table 5.2 – The last row of the table shows the calculated SGR values of each of the studied faults in Floy Canyon. The measured thickness of all the shale units combined is listed in the second row. The throw values are listed in the third row. The equation 3.5 is utilized to measure the SGR.

Name	Loc1 F1	Loc2 Main fault	Loc 2 F2	Loc 2 F3	Loc 2 F4
shale (m)	2	28	6.5	15	2.8
throw (m)	2.3	58	6.5	41.5	4.5
SGR	0.9	0.5	1.0	0.4	0.6

5.2 Seismic fault interpretation of F1 in Aurora storage site

The isolated normal fault F1 in the Aurora storage site is located closest to the injection well 31/5-7, and as previously mentioned. Due to the southerly dip of the storage unit, this fault will

be the first fault to be encountered by the CO₂ plume (Figure 5.13). According to Holden et al. (2022), the F1 fault is north-south striking (352 degrees), dipping to the east and is classified as a second-order fault. Information about the data and methodology behind the fault and horizon interpretation of this study is in Chapter 4.2. In the seismic interpretation, the visible part of the F1 fault is located approximately 700 m away from the injection well 31/5-7. Maximum seismically observed fault length of 3612 m is measured along the two Intra Drake Formation surfaces (Table 5.3).

Ten horizons were interpreted for the target formations: Lower Drake (target seal), Cook (secondary storage), Johansen Formation, Lower Amundsen Formation (primary storage) and an additional Statfjord Group (Figure 5.14, a). The interpreted horizons have an overall even surface, where very little smoothness operation was needed, except for the intra-Cook Fm., which had the poorest reflection quality out of the chosen horizons. The F1 fault extends to the Cretaceous successions and overall has no prominent corrugations on the fault plane. In a detailed analysis 3D view in the MOVE suite, the F1 fault has not a straight fault plane but displays a soft S-shape geometry.

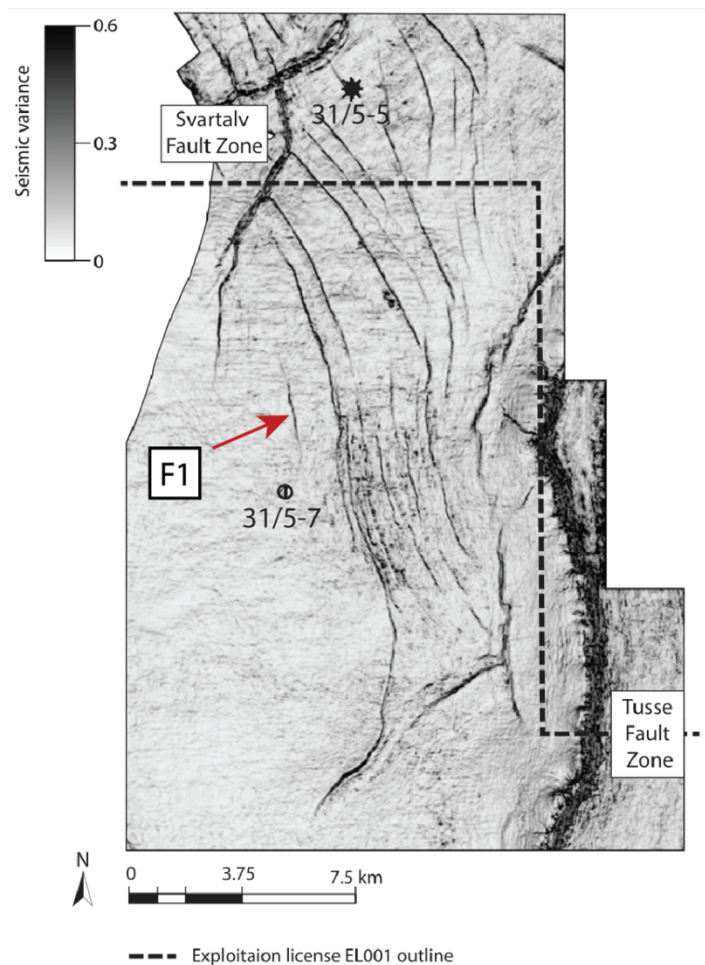


Figure 5.13 – Seismic variance map displaying the faults in Aurora storage site. A red arrow indicates the location of the target fault F1. Figure modified from Holden (2022).

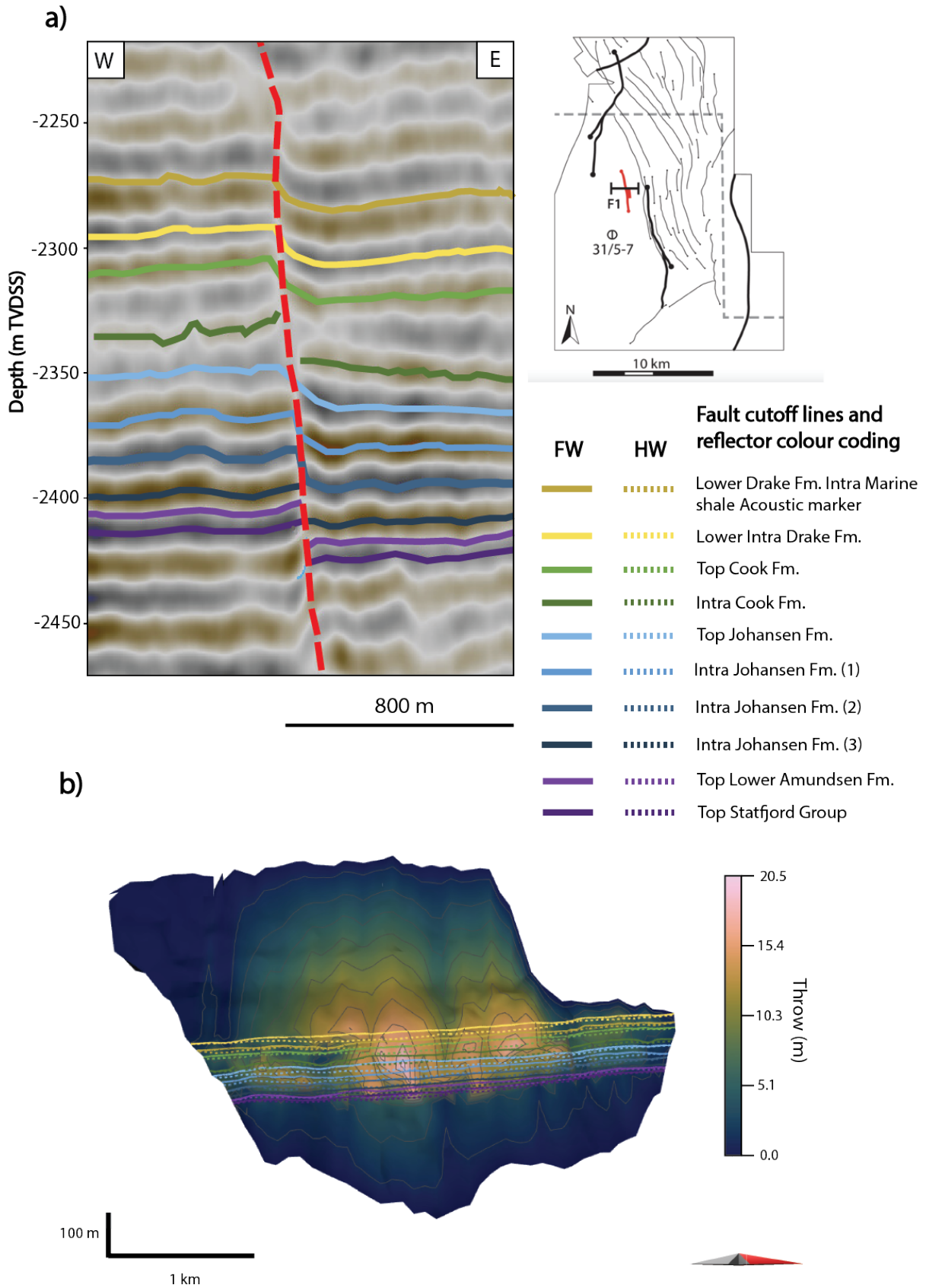


Figure 5.14 (a) Seismic cross section of F1 fault and the interpreted horizons. Cross-section's location is shown in the upper right corner map over Aurora storage site (from Holden 2022). (b) Three-dimensional seismic derived fault-throw diagram of F1. Viewed from the hanging-wall side, showing

horizon–fault intersection (cutoff) lines. Made with MOVE (2022). The scientific colour bar (version 7.0.1) is sourced from Cramer et al. (2020).

The cut-off of Figure 5.16b represent horizons termination on the fault, with the footwall truncation given by a solid line. Hanging wall cutoff lines are stippled. The cut-off lines allow measure of throw for each fault stick based in horizon offset, which can be summarized and contoured for the entire fault surface. The color coding (colour bar) of the 3D fault plane (Figure 5.14, b) represents the plane's throw values, with high accuracy for parts the cut-off lines cover. More uncertainty attached to upper and lower portion of the fault plane with contours based on the cut-off lines in the middle.

The throw vs length values of each horizon are presented in Figure 5.15. Larger throw values reach more than 20 m on the Intra Cook Fm. Considering the minimum vertical resolution (c. 15 m) near the center of the fault, this suggests that the largest throw on F1 is c. 35 m within the interpreted horizons. Noticeable, individual throw vs length lines are curved on different wavelengths. Many of the throws vs length curves display similar patterns, e.g., similar location of highs and lows, which suggest the position of fault-segment linkage areas. However, the overall highest throw values in the middle of the fault and throw gradually decline towards both ends.

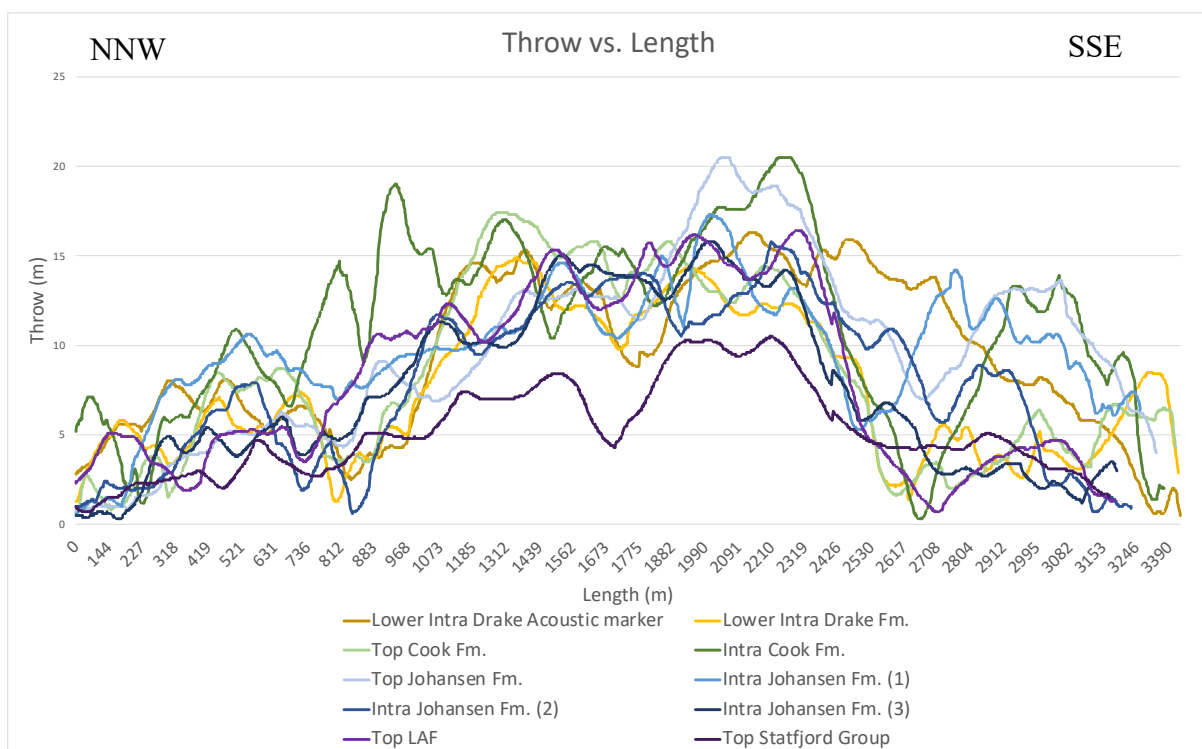


Figure 5.15 - Throw vs. length profile for F1, showing vertical displacement for the lower- middle Jurassic horizons. Zero (0 m) throw equals seismic resolution of ca 15 m. Note that the horizons with “intra” are interpreted horizons inside the belonging formation/group.

More detailed analysis of the curves highlights certain observations. Sites along the fault with similar horizon throw patterns were extracted to expose the unified trends (Figure 5.16). For this instance, the convex patterns were looked for in Figure 5.16, where three prominent structural lows were observed, marked in red stippled circles. The Intra Cook curve (Figure 5.15) displays a very different pattern on the NNW side of the graph, showing peaks whereas most of the other throw vs length curves show decreasing values. This can indicate error during seismic interpretation, where the seismic reflection quality is too low, as mentioned earlier.

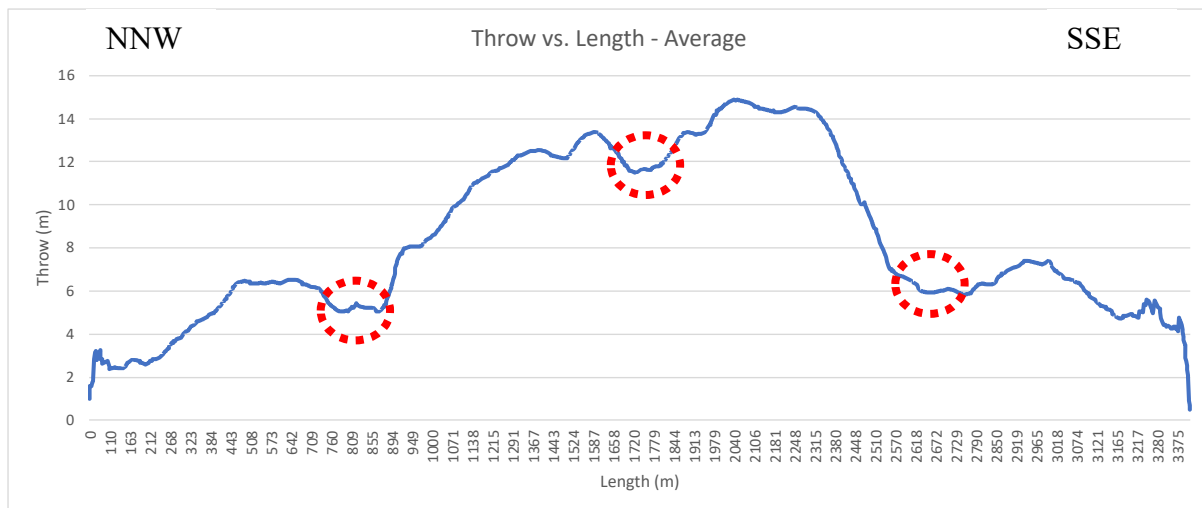


Figure 5.16 – The average Throw vs. length profile for F1. Average value for all the interpreted horizons, showing vertical displacement for the lower- middle Jurassic horizons. Three convex curves were observed marked in red stippled circles. Zero (0 m) throw equals seismic resolution of ca 15 m.

Due to the limit of seismic resolution (c. 15 m), extracts of throw from seismic mapping contain restrictions on the actual length on faults, and hence the curves created for throw (see concept of “missing fault tips” in chapter 4.3.4). Table 5.3 shows the calculation of the total missing fault tip length on each of the target horizons of this study. The calculated, hence suggested true fault length is displayed in the third column of Table 5.3, along with the seismically observed fault length in the fourth column. Values of Table 5.3 shows that the true fault length varies for each horizon. On the contrary, values of observed fault length are approximately the same.

Table 5.3 – List of calculated total missing fault tip length, which is the sum of the extended length of both ends of the throw vs. length curve in each of the horizons. True fault length and the seismically fault length are listed in third and fourth column.

Name	Total missing fault tip length (m)	True fault length (m)	Observed fault length (m)
Drake Intra Marine shale Acoustic marker	2072	5684	3612
Intra Drake Fm	2630	6242	3612
TopCook Fm.	2186	5796	3610
Intra Cook Fm.	1705	5272	3567
Top Johansen Fm.	1969	5520	3551
Intra Johansen Fm. 1	2035	5552	3517
Intra Johansen Fm. 2	2376	5888	3512
Intra Johansen Fm. 3	2782	6269	3487
Top Lower Amundsen	1531	5021	3490
Statfjord Gp.	3300	6784	3484
Average	2259	5803	3544

True fault length can be compared to the lithology succession represented by the mapped horizon. In Figure 5.17, each target horizon's total missing fault tips is placed in the lithological position, hence fit with the Gamma-Ray (GR) log from well 31/5-7 (Eos) together with a synthetic seismogram on the left side. Overall, there appear to be limited differences for fault length is in the sandstones (storage units) versus shales (sealing units). There is, however, signs of a change in trend for major lithological boundaries, or major successions. Between the Lower Amundsen Formation (LAF) and the Johansen Formation, there is a sudden large decrease in length in Lower Amundsen Formation (LAF). There is also a change in the boundary of Drake Formation and Cook Fm., which shows increasing values in Drake succession but decreasing values in Cook succession. The Statfjord Formation is also showing a prominent change in fault length, correlating to the change in lithology from LAF to Statfjord Fm.

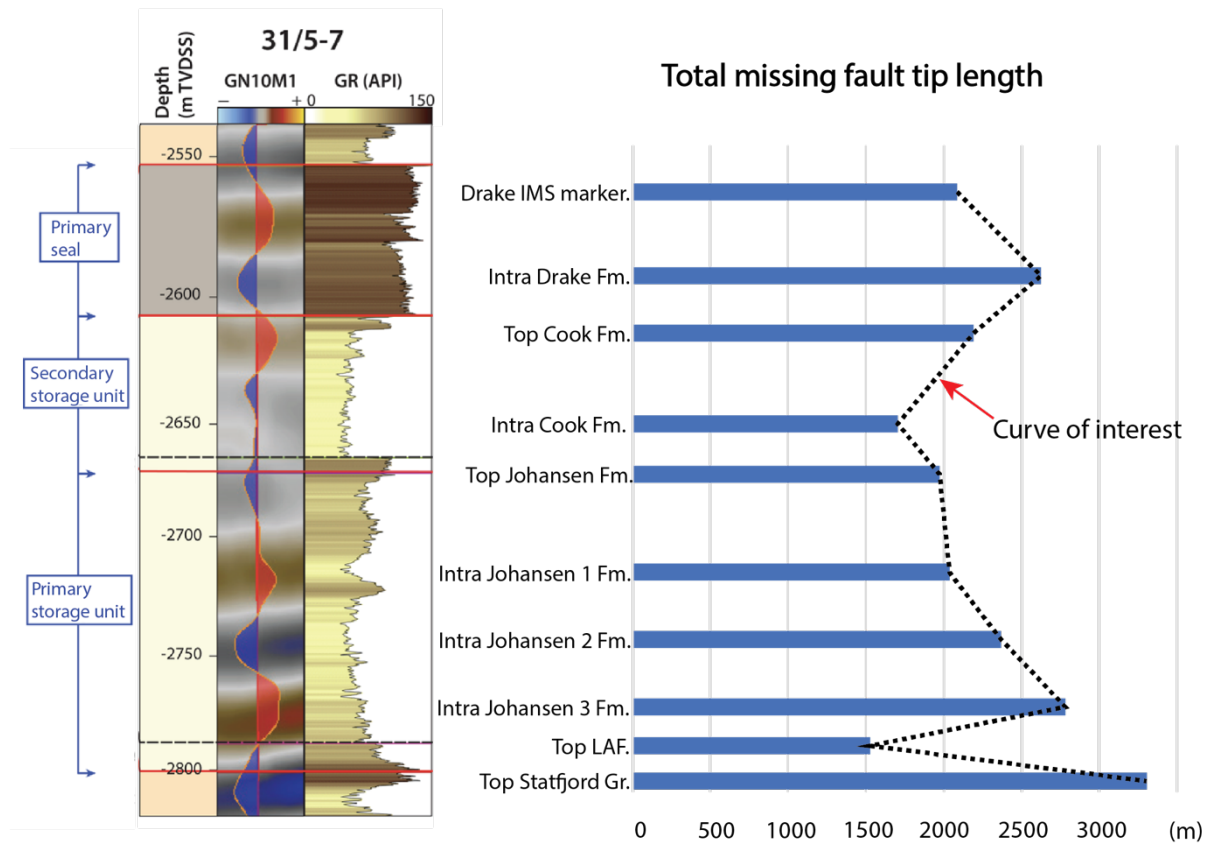


Figure 5.17 – Visually illustrating the total missing fault tip length of each target horizon and a gamma-ray (GR) log from well 31/5-7 (Eos) together with a synthetic seismogram to the left side. The stippled line represents the curve of interest. Gamma-ray (GR) log together with the synthetic seismogram is modified from Holden et al. (2022)

The overall shape of the F1 from true fault length values challenges an elliptical fault geometry that is commonly advocated as a viable model (Figure 5.18, a; Barnett et al., 1987; Nicol et al., 1996; Marchal et al., 2003; Torabi et al., 2019). The "true" fault geometry in Figure 5.18, b does not resemble the three-dimensional fault surface (see also Fig. 5.14, b). In the discussion chapter, implications of this observation are further entertained.

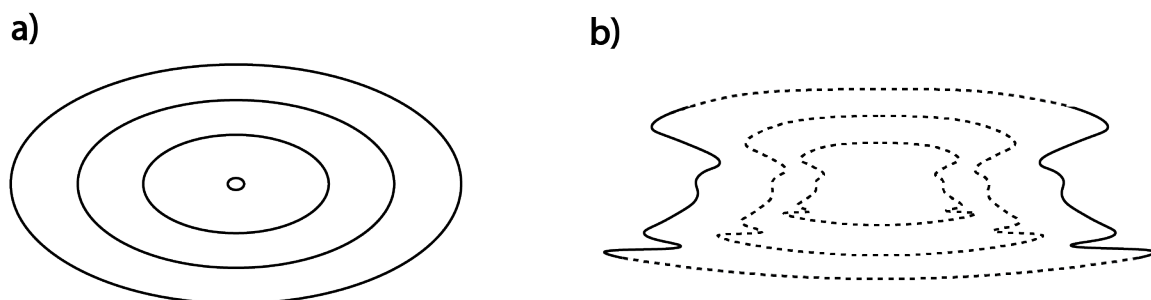


Figure 5.18 - (a) Schematic illustration of an elliptical fault model, where throw values increase to the centre. (b) Figure illustrating the "true" fault shape of F1.

Lastly, the average true fault length as shown in Table 5.3 is visually displayed in Figure 5.19. The seismically observed F1 fault is marked in black, while the missing fault edges are added on each side of the F1 fault, marked in red. The true fault length makes the F1 fault-tip located around 160 m away from the injection well 31/5-7.

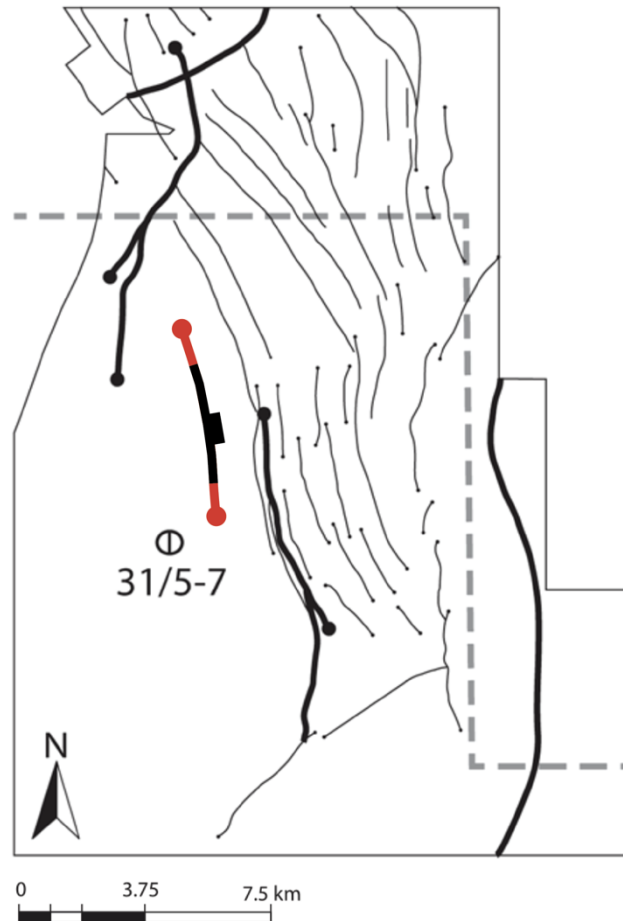


Figure 5.19 – Illustrative structural map displaying faults in the Aurora storage site. The seismically observed fault length of F1 is marked with black. The “missing fault tips” are marked with red. The scaling is not precise in this Figure. Figure modified from Holden et al. (2022)

6 Discussion

This chapter focus on answering several scientific questions outlined in Chapter 1.5, based on the results gained from: i) the outcrops analogues from Floy Canyon, ii) the seismic interpretation on the F1 fault in the Aurora storage site and iii) information provided in the article by Holden et al. (2022) for the larger Aurora site. Holden et al. (2022) assessed the sealing potential of the F1 fault (1D triangle diagrams, 3D Allan diagrams, and SGR calculations). This work expands on these technical study results, testing the same methods in greater detail for a single fault (F1). To increase insight, results are compared to physical analogues of faults, in ways validating or falsifying the outcome of standard fault analysis techniques for the subsurface. As for all type of studies, there are limitations and uncertainties that require discussion. In the end, there are suggestions for further research.

6.1 Geological comparison of the North Sea and the Book Cliffs

There is no such thing as the perfect outcrop analogue since two identical geological systems do not exist, as stated by Howell et al. (2014). When looking for a usable outcrop analogue, determining what aspect the analogue should be used for is recommended. Therefore, combining different analogues and extracting the target information from each analogue may be necessary. A physical outcrop analogue study from Bauer et al. (2017) did not achieve the desired results and concluded that their outcrop analogue was unsuitable for their target reservoir. Bauer et al. (2017) also concluded that it is recommended that the study areas should have similar tectonic history and avoidance of complex settings. Since the study by Bauer et al. (2017) focuses on specific quantitative results, such as petrophysics results in porosity and cementation, the range of what is considered acceptable results is limited. Thus, there is a strict list of criteria that the outcrop analogue must fulfil to achieve specific results (Howell et al., 2014).

The 300-km-long Book Cliffs provides an excellent field laboratory for studying prograding marine to paralic depositional systems. The region is famous for its sequence stratigraphy studies, based in visible clinofolds of many scales, providing a grand physical outcrop analogue for sandstone-shale distribution (reservoir-seal systems) that provide insight applied in hydrocarbon prospecting worldwide (e.g., O'Byrne & Flint, 1996; Flint et al., 1997; Pattison

et al., 2008; Howell et al., 2014). This insight is equally valid for CO₂ storage because of similar requirements: i.e., permeable reservoir, cap rock, and non-leaking faults. Floy Canyon has already been used as a sequence stratigraphic analogue for the Brent Group in the North Sea. There is added value in that the Book Cliffs with the Floy Canyon area offers similar depositional environments as identified for the lower-middle Jurassic formations in the Aurora storage site (e.g., Flint et al., 1997; Pattison et al., 2008).

Both study areas contain normal faults. Noticeable, the Aurora F1 fault offers a maximum throw of 35 m that diminishes towards the tips (see chapter 5.2). Likewise, in the Floy Canyon, faults have throws ranging from 2.3 m to 58 m.

6.1.1 Stratigraphic similarities

In a broad sense, the Book Cliffs region offers high-quality outcrops that are large enough to understand the sandstone-shale distribution with appropriate scale comparable to the entire UK Brent province, as advocated in Howell et al. (2014). This comparison appears valid for the upper Jurassic successions of the northern Horda Platform as well. In the Book Cliffs, the shallow marine to continental, fluvial Blackhawk Formation is prograding into and above the offshore facies of the Mancos Shale. Sandstones of the former formation offer a variety of wave-dominated to fluvial-influenced deltaic and shallow shelf facies (Chan et al., 1991). Likewise, the formations and groups in the Horda Platform are made up of units of continental and fluvial-deltaic to shallow-marine affinity (Deegan, C. & Scull., 1977). Hence, both study areas offer a similar prograding shoreline to deltaic depositional environment overlain by fluvial deposits of the coastal and flood plains. In both cases, the coastline was impacted by wave action in addition to fluvial impact.

As previously outlined (chapter 2.2), the Lower Jurassic Dunlin Group in the northern North Sea comprises the Johansen and Cook formations separated by the sealing Drake Formation (Marjanac & Steel, 1997). The two former units are the target for storage injection in the Aurora storage site. The Dunlin Group developed during humid climate conditions, similar to the upper Cretaceous Blackhawk Formation of the Book Cliffs, where the climate during deposition was warm to sub-tropical (Balsley, 1982, cited in Chan et al., 1991). The shaly dark marine Amundsen Formation interfingers with the sandy Johansen Formation in the North Sea, which is similar to the intertonguing Mancos shale and upper Blackhawk Formation sandstones. The deltaic shoreline sandstones of the Johansen Formation contain sedimentary geometries

indicating deposition during a sea-level fall (Marjanac & Steel, 1997). This is similar to the upper Blackhawk Formation, which has a prominent regressive set of upward coarsening sequences (Chan et al., 1991; O’Byrne & Flint, 1996).

The Cook Formation contain interbedded sandstone and shale with abundant bioturbation and also records a fall in sea level. Again, this is comparable to the Blackhawk Formation, which has interbedded fine sandstone and organic-rich or silty shale with abundant bioturbation (Chan et al., 1991). This is documented in the sedimentary logs of the Floy Canyon (chapter 5.1.1 and Appendix), where sandstones are interbedded with siltstone, organic-rich shale, and mudstone.

A main difference between the two study areas is the thickness of the units. As mentioned, the sedimentary logging conducted in Floy Canyon displays smaller sequences in the interbedding than in the target formations of the Aurora storage site. The difference is found in thicknesses. The primary storage unit, the Johansen Formation, is 116 m thick in well 31/5-7, comprising sandstones and siltstones. The thickest continuous sandstone-silt succession in the Floy Canyon is 39 m, including amalgamated clean sandstone packages that reach 20 m. The primary seal, the Lower Drake Formation, offers shale and silty shale in a 53 m thick assemblage. On the contrary, the thickest sealing unit of the Floy Canyon is approximately 9 m thick. In conclusion, the Aurora storage site comprises both thicker primary storage complex and primary sealing unit than similar units in the Floy Canyon.

Descriptions of the target formation in the Aurora storage site are not mentioned coal beds or coal seams. On the contrary, the Blackhawk Formation hosts multiple coal beds, coal seams and heterolithic mixes of mud and coal beds. Færseth (2006) points to the fact that there are many lithologies in addition to shale and clay that can offer sealing properties, such as coal, silt and carbonate. Therefore, coal can positively influence the sealing probability between layers. Smearred or emplaced along faults, coal may offer fault-seal potential.

6.1.2 Comparison of faults

Both study areas Floy Canyon and Aurora storage site contain upper-crustal, brittle normal faults of similar throw in comparable stratigraphy. As previously explained (chapter 2.1), the faults in the Floy Canyon can be traced to the salt-tectonic fault systems further SE (in the Arches Park). Possible growth-packages in the hanging-wall of the faults suggest latest Cretaceous activity. This period experienced foredeep subsidence of the Colorado Plateau in

front of the Sevier Orogeny developing in the west. In addition, a west to east prograding coastline enforced differential loading. The dynamics of differential subsidence and loading likely triggered salt tectonics prior to the Laramide Orogeny (Kauffman, 1977 and Stokes, 1986, as cited in Chan et al., 1991; Hecker, 1993, as cited in Shipton et al., 2004).

The tectonic setting of Utah is different to the tectonic history of the North Sea, where two large-scale rift events dominate. The lower-middle Jurassic stratigraphy in the northern North Sea appears between two rift periods, during general quiescence and subsidence. Many of the initial faults of the Permo-Triassic event were reactivated in latest Jurassic to Early Cretaceous rifting (Whipp et al., 2014). For the Troll-Aurora region, encountered growth-packages of early Cretaceous age (mainly Cromer Knoll Formation) postdate the storage formations. Therefore, the burial depths of the target formations in the Aurora storage site and the Blackhawk Formation in Floy Canyon are different. Since the highest throw in F1 is located in the Cook Fm (Lower Jurassic period), it indicates that the burial depth during the fault nucleation was less than 1 km (Holden et al., 2022). There would however be differences in burial depth depending on positions in foot- and hanging-walls as the faults evolved. As previously mentioned, when the faults in Floy Canyon were initiated, the burial depth was shallow, within meters to a maximum of 50 m from the earth's surface (Braathen & Midtkandal, pers. comm., 2022).

This difference in burial highlights considerations around lithification besides enveloping stress (both increasing with burial), which expectedly could influence fault architecture, or rather deformation mechanisms, as for instance discussed by Braathen et al. (2013) (See also Fossen et al., 2007, Torabi, 2014). Following this reasoning, the Floy Canyon deformation in faults was to a large degree by granular flow in poorly lithified sediments, with most deformation concentrated to the fault core and with narrow damage zones made up of disaggregation deformation bands. With more prominent lithification in Aurora, overall deformation by cataclasis (crushing) could be expected for the faults, probably more pronounced in the deeper buried hanging-walls. Accordingly, there could be wider damage zones with cataclastic deformation bands of low permeability (Torabi et al. 2021). Such general reasoning must however be applied with care, as lithification also enhances with cementation, not only burial, as for instance shown for the Ferron delta faulting of Utah that facilitate both disaggregation and cataclastic deformation bands in a near-surface position (Braathen et al. 2018).

6.2 Field data uncertainties

Outcrop analogues have been important tools for better understanding subsurface reservoir architecture (Howell et al., 2014). Data of the Floy Canyon contain both qualitative and quantitative information, such as the intrinsic distribution of fault elements and their shapes, allowing quantification of dimensions for elements. Besides, there is detailed stratigraphic information. Fault core architecture and fault element descriptions were observable down to mm resolution. On the challenging side, limited outcrop size, and scree cover, offer a small window of observation into relatively large faults, a consideration outlined by Braathen et al. (2009): questioning the general validity of individual fault datasets, and promoting statistical patterns when applying such data in forecasting the architecture of subsurface faults.

6.3 Seismic interpretation uncertainties

The seismic interpretation of fault F1 was accomplished within an area of 69 km². Horizons were interpreted in 625x1260 m grid resolution, which is every 50th increment spacing (chapter 4.3.2 for methodology). Cunningham et al. (2021) recommend the densest horizon interpretations of 50 m inline and crossline spacing of 12.5 m, with the densest increments revealing the most accurate results. However, such detailed work requires significant time. These authors also tested a less dense spacing of 32 inlines and 32 crosslines, in a 400 m grid, where they concluded the results gave inaccurate horizon interpretations. Besides, less dense spacing impacted the fault interpretation, resulting in underdeveloped relay morphologies and throw profiles. While Cunningham et al. (2021) suggest that a denser grid spacing is recommended for detailed geological analysis, I observed that a 50 x 50 grid increment spacing of 625x1260 m was sufficient to detect important features in the Aurora storage site.

The fault interpretation of this study inline spacing of 75 m, which has an increment of 3 (chapter 4.3.3). An increment spacing of 75 m fits well with the recommended fault interpretation spacing of Michie et al. (2021), recommending optimum spacing of 100 m, while less than 50 m spacing revealed more complexity associated with human error. Hence, these authors concluded that dense interpretation spacing is unnecessary and can produce rough fault surfaces that can negatively impact the fault analysis. On the other hand, over 100 m spacing in fault interpretation can lead to overly smooth fault surfaces that miss details that can be important for fault growth models and fault seal analysis (Michie et al., 2021). Cunningham et

al. (2021) recommend the fault interpretation with 50 m spacing, which is on the limit of maximum density spacing that Michie et al. (2021) believes is unnecessary.

The fault interpretation process of the F1 fault in the Aurora storage site had no trouble during horizon interpretation, as there were very few irregularities in each of the horizons after the auto-tracking process. The fault interpretation was the most time-consuming part due to the dense increment spacing, combined with very careful picking of the fault. When creating the cut-off lines in PETEX Move, very little error had to be corrected, which points to a trustworthy result. One exception was the top Brent horizon, which had too many errors to be included. Therefore, I would recommend a denser increment spacing to interpret the Top Brent horizon in the Aurora storage site. This is highlighted in the average throw vs length of all the interpreted horizons (Figure 5.16), which show prominent patterns of highs and lows in the curve. With striking unified trends, data quality is convincing, allowing better analysis of, for instance, fault growth patterns and segment linkages. As previously mentioned in chapter 5.2, the Intra Cook throw vs length plot partly deviates from the unified pattern. With the poorest reflector quality out of all the chosen horizons (chapter 4.3.2 and Table 4.1), this stress that quality suffers in poorer datasets.

The highest throw in the F1 fault of the Aurora storage site is 35 m. Notably, Holden et al. (2022) achieved 40 m as throw maximum on F1. This difference can be ascribed to differences in inline and crossline spacing when interpreting key horizons, Holden et al. (2022) applied a 25 and 12.5 m interpretation spacing, which is a much denser than what is used in this work. Time invested on quality control with a denser interpretation spacing could have minimized the differences in throw seen herein compared with Holden et al. (2022). Furthermore, two geologists who interpret the same dataset can likely have a margin of error of 5 m caused by interpretation differences in horizons, faults and cut-off lines.

6.4 Floy Canyon; Fault facies and sealing capabilities

Fluid flow in brittle fault zones of the upper crust depends on the fault zone architecture and the overall permeability structure (Caine et al., 1996). A reoccurring challenge for the industry is the risk attached to fault seal capacity: how much of a fault can seal a specific CO₂ or hydrocarbon column? The fault zone architecture can be highly variable, with many factors influencing fluid migration. When analyzing the fault seal capacity, risk depends on the location

of the fault. The sealing capacity varies along the length and height of the fault because of the fault geometry and its variable fault core architecture (Færseth et al., 2007).

In the following, the geometry and fault facies of faults in the Floy Canyon are analyzed, with an emphasis on a few cases illustrating the importance of fault architecture by combinations of elements, guiding a discussion of sealing vs non-sealing capability. Pathways for possible across- and along-fault fluid migration will be illustrated where available.

6.4.1 Presence of fault seal

If there is a presence of a coal smear and if continuous smears will act as barriers for across-fault flow within the fault core, were two of the scientific questions expressed at the end of the introduction chapter (sub-chapter 1.5). Several coal smears were observed, and the sealing capabilities will be further discussed in this sub-chapter.

Fault F1

Fault 1 (Floy Canyon) with a small throw of 2.3 m, shown in Figure 5.5, is interpreted to have a semi-continuous coal smear membrane along the interlinked but overstepping principal slip surfaces (Chapter 5.1.2). Farther down section, a continuous coal membrane with 3 cm thickness appears. A membrane seal has a sealing probability of 50-70%, following Færseth et al. (2007). Regardless of whether this fault offers a fully continuous coal smear membrane, or a gap between two membranes, there is no well-positioned sand lens that can contribute to sand-sand communication across the fault zone (chapter 3.3.3). Rather, two lenses made up of coal and heterogenous coal and silt (LtC and LtD) contribute to the sealing probability of the fault. Overall, the fault zone holds a high shale/mud/coal content, which promotes higher sealing capacity.

The sand gouge shown in Figure 5.5.B2 appears to be composed of grain size reduced sandy material, which may offer some permeability for the Floy Canyon case of near-surface faulting. Detailed analysis of thin sections needs to be performed in order to determine the grain size reduction. However, brittle deformation of clean sandstone at depth, similar to the Aurora case, would expectedly create a highly crushed impermeable rock. This principle follows that of disaggregation vs cataclastic deformation bands with related deformation mechanisms, in general ascribed to burial depth (Loosveld & Franssen, 1992; Fulljames et al., 1996; Fossen et

al., 2007). As mentioned, Braathen et al. (2018) study of the Ferron delta (Utah) document co-existence of cataclastic and disaggregation bands, in a setting where maximum burial is less than 15 m, challenging the general rule of thumb. For this case, however, carbonate cement locates cataclastic deformation bands, hence cementation promotes permeability loss of both the host rock and superimposed deformation structures (Fossen et al., 2007).

Fault F2

Fault 2 of Floy Canyon, shown in Figure 5.7, B2, offers a throw of 6,5 meters. Its location is next to the Main fault. This fault mainly consists of sealing lithology (including silt). A LtC lens is dissected by several bookshelf-style shear fractures, without membranes, which can behave as a conduit to fluid flow. According to Faulkner et al. (2010), open fractures and slip planes in the fault core can be permeable depending on their distribution, connectivity and if they cross-cut lower permeable units. The bookshelf shear fractures in the LtC lens do not crosscut other structural elements, but rather tips in the protobreccia, which could be permeable, following Woodcock & Mort (2008) and Bense et al. (2013). Since the protobreccia in question is made up of mud and silt, it is considered basically sealing.

Gypsum veins were observed along and parallel to the principal slip plane in fault F2 (Figure 5.7, B2; Figure 5.8, C2). This gypsum is participated in open fractures from migrating fluids, with a likely source in the underlying Jurassic Summerville Formation (Warren, 2006; Rustichelli et al., 2016). Gypsum can act as a barrier to flow depending on the physical and chemical alteration and the veins' dimensions and distribution. In conclusion Fault F2 contains continuous coal smears, overall contributing to the sealing probability. The coal smears connect with the LtC lens and a gypsum fracture fill, which in sum offer a continuous membrane.

Fault F3

Fault 3 (location 2 in Figure 5.9) has a throw of 41.5 m. Host lithologies in the hanging wall and footwall are low-permeability units. This fault holds a continuous coal smear along the principal slip plane, and in addition two LtC lenses. All contributes to the sealing capacity. In Figure 5.10, a close-up of a silt breccia, hypothetically permeable, is bound by underlying and overlying coal smears, removing leakage risks. A heterogenous fault breccia displayed in Figure 5.10, C2 would not likely be permeable because of the abundant coal matrix that surrounds the silt clasts. In conclusion, this fault has a significant sealing potential.

6.4.2 Implications for fluid migration

One of the four research questions defined in this thesis was to identify whether there will be an indication of across- or up-fault fluid migration based on the fault facies architecture. Based on the observation in Floy Canyon, clear structures of potential non-sealing faults are discussed below.

Main fault

The Main fault of location 2 (Floy Canyon), seen in Figure 5.6, has the largest throw of 58 m, and accordingly the widest fault core. This fault also contains the largest lenses, where three sand lenses (LtA) are in proximity to each other. A LtC lens could contribute to the sealing probability, but this lens sits in isolation in otherwise permeable elements. Thereby, sand-sand communication across the fault zone is likely (Færseth et al., 2007; Bond, 2015). Figure 6.1 shows the concept of sand-sand communication from connected sand lenses, illustrating a fluid pathway for CO₂ from lower stratigraphy in the fault's footwall, into sandstone lenses interconnected in the fault core, and upwards reaching a hanging-wall sand layer. For this fault, the scarcity of flow-blocking shale/coal membranes could relate to two factors; the offset lithologies do not contain a thick source layer of shale or coal, and the large throw leads to discontinuous smear from thinner shale/coal layers (Færseth et al., 2007).

In addition to sand lenses, a thoroughgoing slip-surface represent a fault-parallel fracture that could allow fluid flow. Without membrane continuity along the slip-surface or between lenses, this fault is interpreted as overall permeable.

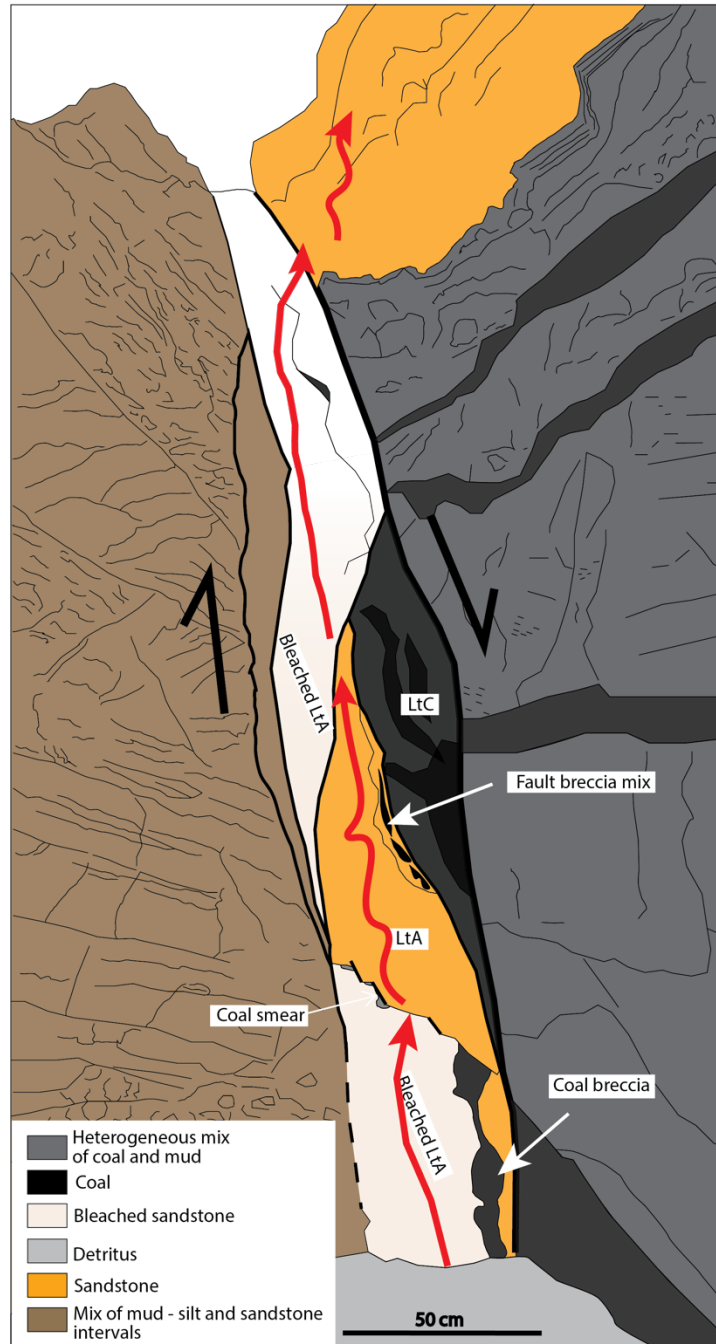


Figure 6.1 – Conceptual illustration showing sand-sand communication across fault. The sand lenses (LtA) are adjacent to each other, forming a fluid migration bridge. Figure is modified from Figure 5.6, A2.

Fault F4

Fault 4 (location 2 in Figure 5.11), with a throw of 4.5 m, offset two clean sandstone units, on the hanging wall and one in the footwall. The fault core contains an intricate fault core architecture, offering interesting discussion points. Figure 6.2 illustrates possible fluid migration pathways through sand-sand communication across the fault. In addition, the upper

part of the elongated sand lens consists of a protobreccia, which likely further enhances the permeability (Woodcock & Mort, K., 2008; Bense et al., 2013). A prominent smear-like drag-fold of coal from the hanging wall almost cut off the upper tip of the sand lens. However, the sand lens is in contact with the heterogeneous breccia in between the two LtA lenses. The breccia mix has portions of coal and mud within and is less permeable than the sandstone breccia underneath. In conclusion, there is a juxtaposition seal for the fault, but the fault core may allow along-fault fluid flow that connect host sandstones through sandstone lenses and breccias.

The membranes in fault four are scattered, and there were no visible continuous clay or coal smear along the slip planes. The white proto sand breccia is placed adjacent to the sandstone hanging wall, which can open for second fluid migration pathways. Although, the breccia is heavily thinned and dragged along the slip plane, which can reduce the permeability (Woodcock & Mort, K., 2008; Bense et al., 2013).

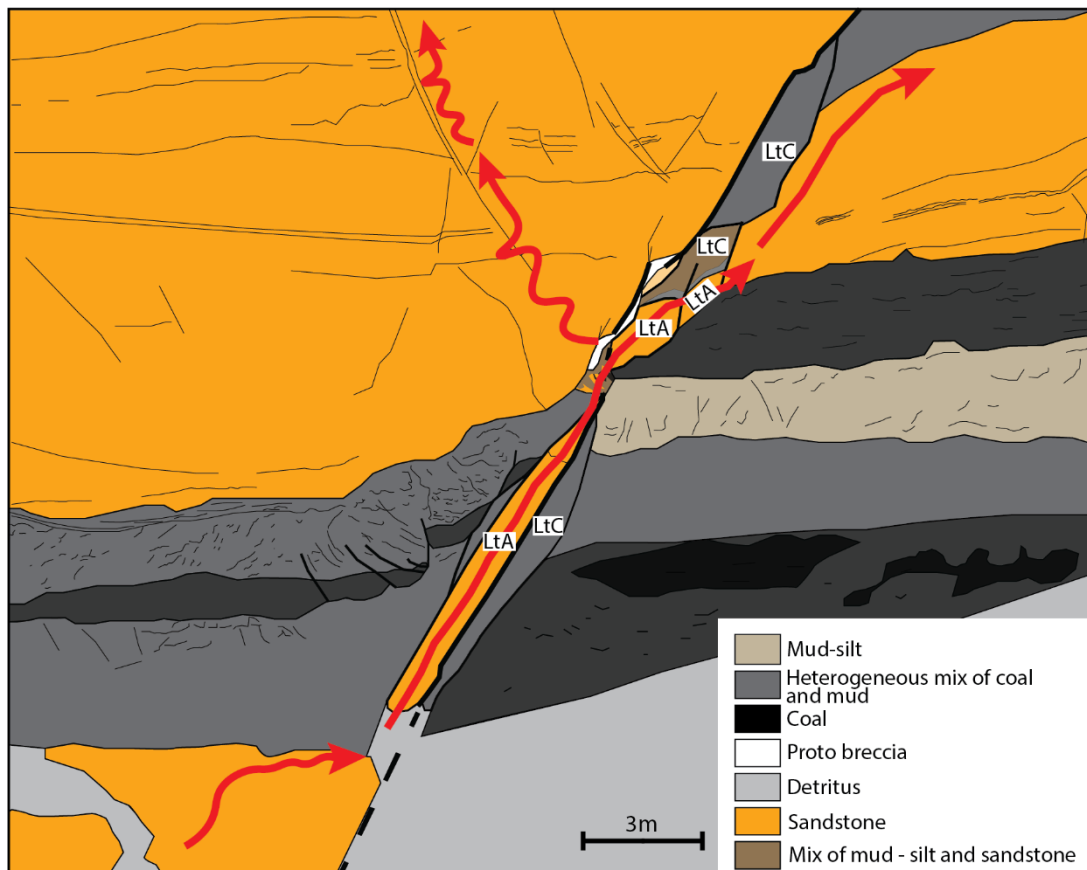


Figure 6.2 - Conceptual illustration showing sand-sand communication across fault. Figure is modified from Figure 5.11, A2.

6.5 SGR calculation – Floy Canyon

As previously stated in the chapter 3.3.2, the Shale Gouge Ratio (SGR) calculates the percentage of shale or clay content in a slipped interval (throw) at any given point on the fault surface (Yielding et al., 1997). SGR calculations of equation 3.5 are displayed in Table 5.2.

For the faults in Floy Canyon, the SGR is calculated for one point in the fault plane, which is different from the way the algorithm commonly is applied in subsurface data. SGR models the sealing probability along a fault plane offsetting a given stratigraphy, using a drill-hole gamma-log curve, predefined as sealing vs non-sealing lithologies, like a V-shale curve. With this input, the analysis is performed by software's that calculate SGR for numerous points of 3D fault surfaces. SGR for outcrop faults offers a single point in a fault that is much larger than the actual outcrop. Another challenge is the consideration of silt as a sealing or non-sealing lithology, rather than using well-log values. Clay material in the silt units is unknown. In this study silt is considered as 100% sealing and, by using the simplified SGR equation, the SGR values of the faults in Floy Canyon are likely to overestimate the sealing probability.

Yielding (2002) states that SGR values range from 0 to 100%: SGR values less than 15% are 'leaking', 15–20% represents a boundary between 'leaking' and 'sealing', and SGR >20% are 'sealing'. Based on conclusions by Yielding (2002), all the studied faults in Floy Canyon are categorized as 'sealing'. As dwelled on above, the faults in Floy Canyon contain complex fault core architecture challenging the general SGR assumption of perfect mixing in the fault core (Færseth et al., 2007). In brief, the SGR calculations seen in light of fault architecture (fault facies) are summarized as:

- (i) Fault 1 with an SGR value of 90% (Table 5.2) is regarded as very sealing, almost maxing in sealing probability. The fault facies observations on fault 1 overall conforms with this calculated SGR value.
- (ii) For the Main fault, an SGR value of 50% is classified as sealing. There, the fault facies observations suggest the contrary, with scattered membranes and abundant sand lenses (Figure 5.6). Hence, the SGR value does not fit with the fault facies description.
- (iii) For Fault 2, the SGR value is 100% with 6.5 m throw in a succession with mostly silt, mud and coal. Consistently, the fault facies observations suggest continuous membrane seals in this fault.

- (iv) Fault 3 offers an SGR value of 40%, which still counts as sealing. Interestingly the SGR value for this fault is less than for the Main fault (50%). In this case, the fault facies observations suggest continuous fault smears.
- (v) Fault 4 has an SGR value of 60%, which counts as highly sealing. On the contrary, the fault facies observations suggest the fault is open to fluid flow.

One of the scientific questions at the end of the introduction chapter expressed if there is a relationship between calculated SGR values for faults and the presence of clay membranes in the faults. This summary shows that there is some match between SGR implications and fault facies distribution in faults, when the later are considered as sealing or non-sealing architecture. However, with five observations of which two contradicts the SGR conclusion, there are concerns around the precision of SGR predictions in a general sense. The implication of comparing the SGR values and fault core architecture shows that evaluating the sealing probability can be more complex than precipitated. The two contradicting SGR results cannot alone conclude that the SGR method is unreliable; therefore, more research is needed. Further implications of SGR and fault facies geometry will be discussed in sub-chapter 6.7.

6.6 F1 – Aurora storage site interpretation

The F1 fault of the Aurora site (Figures 4.1 and 5.13) in seismic reflection data is depicted as a uniform 3D fault surface (chapter 5.2). The average throw vs distance curve (Figure 5.16) shows a fairly symmetrical concave curve, peaking in the middle, which, according to fault growth theory (Walsh & Watterson, 1988; Rotevatn et al., 2018), suggests the F1 fault was growing in isolation rather than interacting with nearby faults during its evolution. This waveform of the displacement curve also shows three distinct structural lows, which point to segment linkage areas during fault growth. This suggests that four fault segments are hard linked in the development of the F1 fault (theory in chapter 3.2.1).

Where soft-linked relay zones occur, an increase in fluid flow has been observed that results in acting as a conduit. (Trudgill and Cartwright, 1994; Rotevatn et al., 2009; Fossen and Rotevatn, 2016). The interpreted hard-linked areas are proposed to be breached relays and hence can possibly be a high-risk area for CO₂ fluid migration across- or up-fault fluid flow due to relict relay zones that are no longer visible in seismic fault interpretation (Michie et al., 2021). As previously mentioned, limited seismic resolution masks the identification of more than one slip

plane (Færseth et al., 2007). Therefore, the interpreted fault surface represents a simplified version of the fault zone. In seismic fault interpretation, human errors also need to be considered besides the details of the interpretation work (Bond, 2015; Faleide et al., 2022).

6.6.1 Extended fault tips

Sub-seismic structures, such as small-scale faults or fractures, are below the seismic resolution limit (see sub-chapter 4.2.1 and 4.2.4). Power-law distributions suggest there are significantly more smaller-scale (sub-seismic) structures than larger-scale structures that are seismically detectable (e.g. Hatton et al., 1994; Vermilye & Scholz, 1995; Renshaw & Park, 1997). Because of large numbers of sub-seismic structures, they influence permeability and flow routes in the sub-surface (e.g., Walsh et al., 1998; Mitchell & Faulkner, 2012).

Seismic resolution limits the mapping of the F1 fault, as mapping depicts that both ends of the faults ends at c. 15 m stratigraphic offset, as shown in Figure 5.19 (see sub-chapter 4.3.4). To extend the fault out to zero displacement, to the tip, each of the interpreted horizons within the target formations had missing fault length that was calculated. Fault length differences are shown in Figure 5.17 and Table 5.3. Overall, the average mapped F1 fault length needs additional 2259 m to reach the tips.

A linear displacement gradient was used on each end of the displacement graph of mapped horizons to calculate the missing fault tips, following Kim & Sanderson (2005). Note that Pickering et al. (1997) argue that the gradient should be logarithmic, not linear. In any case, fault lengths commonly are underestimated by 250–1000 m; hence, smaller faults, such as F1, are probably longer than illustrated in Figure 5.19.

Figure 5.17 shows the missing fault tips of each interpreted horizons. Noticeably, there are signs of a change in tip position on a scale of major lithological boundaries. This indicates that significant litho-mechanical interfaces impact tip propagation, seen as the time-glass appearance of the fault tip in the studied stratigraphy. The fault appears to have propagated farther out in parts where overall sandy sections meets domineering muddy-silty sections, such as Intra Johansen 3 Fm, and Top Statfjord Gr (Figure 5.17). As seen in the Gamma-Ray log in Figure 5.17, Top Cook Fm consist of some muddy-silty lithology that explains this section did not propagate farther out.

6.7 Fault seal assessment of Aurora F1 fault in light of outcrop analogues of Floy Canyon

The F1 fault of the Aurora Storage site with the added sub-seismic part tips out approximately 160 m north of the injection well 31/5-7. Accordingly, F1 will be the first fault to encounter the CO₂ plume. Holden et al. (2022) analyzed the sealing probability for F1 fault by various sealing methods, such as a 1D triangle adjoined with SGR values and an Allan diagram. Their results show that the F1 fault has juxtaposition seals on the low throws of the fault that is replaced by a sand-sand juxtaposition for the primary storage (Johansen Fm.) in middle parts of the fault where the throw is higher (Figure 6.3, a; Holden et al., 2022). Upper Amundsen Formation (UAF) is present across the F1 fault - this unit is mostly made up of marine siltstone and can act as a sealing unit. Although UAF has sealing capabilities, the unit is too thin to be interpreted in the seismic dataset, where Holden et al. (2022) calculated the average thickness from three well data in the Aurora storage site. Therefore, UAF is not regarded as a regional seal, while recent studies suggest it would likely act as a baffle between the primary and secondary storage units (Meneguolo et al., 2022).

The juxtaposition seal is regarded as the seal with the largest sealing probability, while the second-best sealing method is membrane seals (see sub-chapter 3.3.1 and 3.3.2). However, the SGR diagram in Figure 6.3, b from Holden et al. (2022) shows that the area with no juxtaposition seal contains an SGR value of less than 20%, which means that there is a low probability of membrane seal. The SGR values for the secondary storage juxtaposition seal are above 40%, which gives a high membrane seal probability.

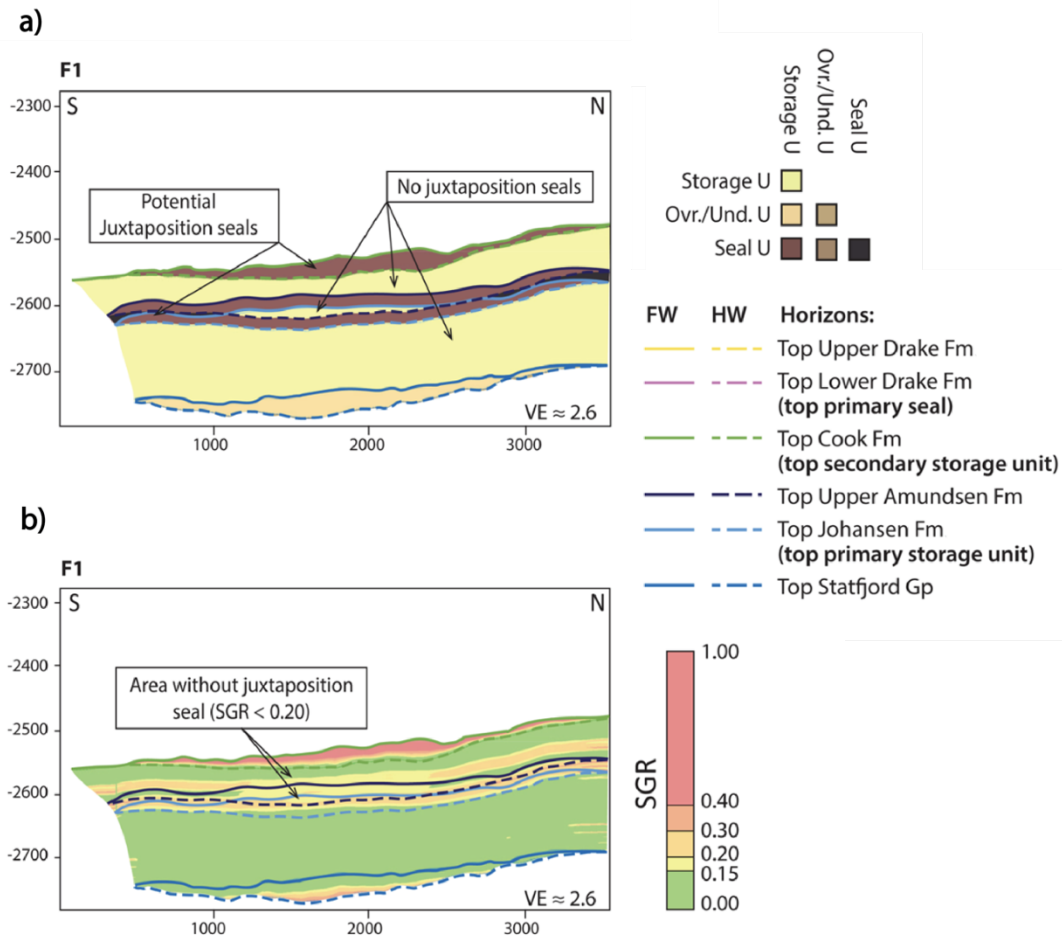


Figure 6.3 – (a) Allan diagram of F1 fault in Aurora storage site showing a close-up of storage-complex horizon cutoff lines and fault intersections. (b) SGR diagram of same close-up as in a). Figures from Holden et al. (2022)

In summary, Holden et al. (2022) predict that most of the CO₂ will be channelized along the footwall side of the F1 fault and migrate northwestward. For the primary storage, F1 will allow across-fault migration (Fig. 6.3) in the central part of the fault because of the presence of a non-juxtaposition seal and the lack of a membrane seal. However, due to the dip of the primary storage unit, the CO₂ will migrate northwards, perpendicular to the contour lines, therefore, migrating parallel to the strike of the fault. It is unlikely that there will be pressure buildup due to the accumulation of CO₂ near the F1 fault as the structure is isolated. Another implication of the across-seal assessment of F1, in a scenario with upwards flow along F1 into the secondary storage, CO₂ will likely be channelized along the footwall side of F1 and migrate northwestwards, as for the underlying primary storage unit. Scenarios for fluid flow along and across the F1 fault are further discussed below.

Fluid migration paths must be considered with the added fault tips, not included in Holden et al. (2022). These sub-seismic parts of the fault as analyzed herein (chapter 5.2) will impact fluid migration by potentially further channelizing the CO₂ migration along foot- and hanging-wall sides of the fault, overall placing the fault as a baffle that separates the plume into two bodies. Especially the location of the southern fault tip some 100 m from the injector well could split the flow paths more significantly than hereunto envisioned.

The results from Floy Canyon show herein that the SGR calculation should be used cautiously, even though only one point was calculated within each Fault in Floy Canyon. SGR values are more reliable if the offset lithologies do contain a thick source layer (Færseth et al., 2007). Discontinuous fault smears are often due to either scattered source layers and/or the fault throw being too large, such as the Main Fault with 58 m throw. As for this case, the Floy Canyon perhaps had too scattered source layers for the SGR to be trusted, or perhaps the silt layers should be excluded in the SGR evaluations. The secondary storage juxtaposition seal on the F1 fault has the 53 m thick Lower Drake seal included in the offset lithologies, which along with the juxtaposition seal, makes the SGR values likely more accurate.

In contrast, the juxtaposition seal in the primary storage along the F1 fault has predictable low SGR values, but as we observed in Floy Canyon where the two faults that contain sand units in the offset lithologies, undependable of high SGR value had prominent sand lenses. Since the primary storage (Johansen Fm.) has a thinner overlying source layer (Upper Amundsen Fm) and the secondary storage on top, there could likely be sand lenses within the fault core adjacent to the primary storage juxtaposition seal, which potentially creates across fault migration (Figure 6.4). Due to the seismic resolution limit, we cannot observe any structures under the size of 15 m (Figure 6.4, A); therefore, only suspect the presence of sand lenses within (Figure 6.4, B).

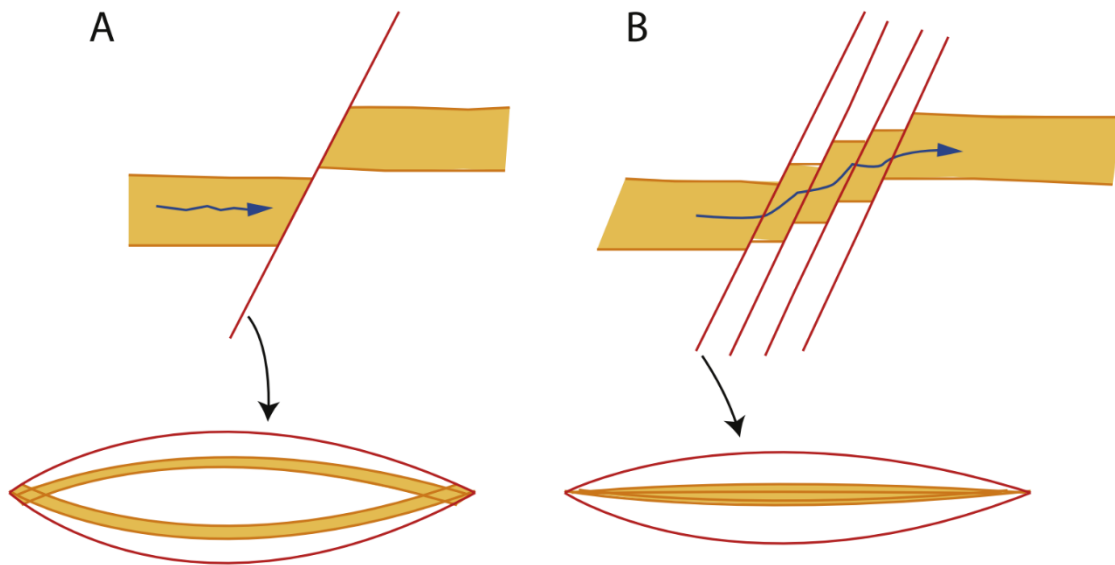


Figure 6.4 – Hypothetical figure showing fault off-sets and their associated Allan diagrams. (A) With seismic resolution limit, figure illustrates juxtaposition seal and a single slip-plane. (B) Hypothetical the same fault as A without seismic resolution limit, showing the true fault core structure; several slip planes with sand lenses in between creating migration pathway. Figure from Bond (2015).

Obviously, the results from Floy Canyon cannot directly forecast the fault seal assessment of the F1 fault of the Aurora storage site. However, these analyses build understanding around complex architecture of a general fault zone at a high resolution, with higher validity if faulting impact similar sedimentary facies belts. There are, as mentioned, limitations in both seismic interpretation and outcrop analogue models. In the following, all work in the thesis is synthesized into a conceptual figure, in an attempt to shed more light on the fault analysis. By that Fly Canyon information is placed on top of the Aurora F1 fault – this allows an interesting discussion of the expected fault-seal status.

Figure 6.5 summarizes the potential across fault fluid migration in the F1 fault at the Aurora storage site based on the results from the fault outcrop analogues in Floy Canyon (FC) and seismic interpretation of F1 and fault. Four potential across-fault fluid migration scenarios are shown. Figure 6.5 a and b shows the conceptual F1 fault surface with an integrated “true” fault shape from Figure 5.18. Figure 6.5 a) displays the seismically derived fault-throw diagram from Figure 5.14, b, and Figure 6.5 b) shows the Allan diagram compiled from the F1 fault assessment from Holden et al. (2022) and the herein F1 fault interpretation. The three vertical breached relict relay zones are placed in the F1 fault surface, considered high-risk areas for across- or up-fault fluid migration despite the present juxtaposition seal (Michie et al., 2021).

The stippled throw lines of 8 m and 23 m follow a conceptual fault model of where the throw increases towards the center of the fault plane. These combined data, for instance where the 8 m throw contour meets the breached relay as located with dots, visually points to zones of higher risk for fluid mobility in the F4 fault. The seismically derived fault-throw diagram of Figure 5.14 shows a visible bullseye with the highest throw of 35 m, which are considered of similarity to the Main fault in Floy Canyon (Figure 6.5, a).

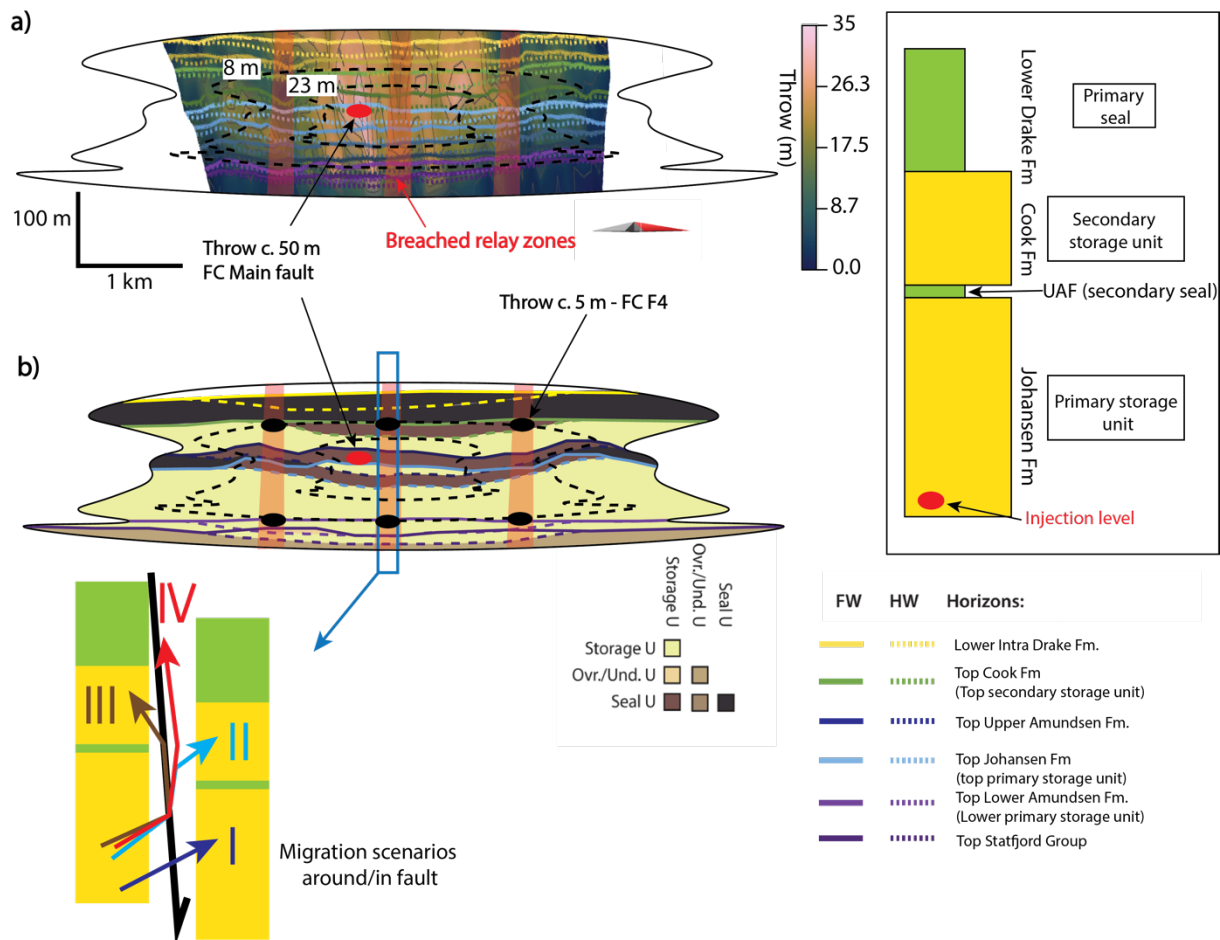


Figure 6.5 – Summary figure displaying illustrative F1 fault surface. (a) seismic derived fault-throw diagram with illustrative throw contour lines. (b) Assembled Allan diagram of F1 of fault seal assessment from Holden et al. (2022) and F1 fault assessment from this study. Four suggested migration scenarios are shown in lower left. It is suggested that the Main Fault and F4 in Floy Canyon (FC) are potential fault core assimilation to the pointed areas on the F1 fault surface.

The following discussion centres around four scenarios for migration routes:

- (i) Across-fault migration
- (ii) Up- and across fault migration into the secondary storage in the hanging wall
- (iii) Up-fault migration into the secondary storage in the footwall
- (iv) Up-fault migration bypassing the top-seal and escaping the targeted storage units

For the smaller faults in Floy Canyon (< 5 m throw), a sealing status is predicted. This would coincide with larger parts of the Aurora F1 surface. However, the 8 m fault in Floy Canyon hosts numerous sandstone lenses, offering a likely fluid bypass system. These lenses points to breached relay zones (see below), suggesting this would be the more likely locations for fluid migration similar to scenarios I-III.

For the The Main Fault of Floy Canyon, which has a throw of c. 50 m, there is similarity found for the centre of F1 fault in Aurora (35 m throw). Numerous sandstone lenses in the Main fault besides a through-going slip-plane (the latter common for larger faults; e.g., Braathen et al. 2009), are considered crucial for possible across- or up-fault fluid migration (migration scenarios II-IV, Figure 6.5). As outlined for instance in Childs et al. (2009), such lenses relate to fault growth of individual segments that link, implicitly pointing to more or less breached relay zones for higher lens frequency. Similarly, Michie and Braathen (in press) emphasize the importance of higher risk in breached, relict relay zones. They detect such zones by utilizing Throw-Distance plots, similar to this study (Figure 5.16). Further, they highlight the importance of knowing the fault linkage history, which can hypothetically influence whether fluids can flow across- or up-fault.

In the end, the observation of lenses and through-going slip-plane for larger fault throw, suggest larger offset parts of the Aurora F1 compared to bed thickness have lower sealing probability. This would be especially valid for the Upper Amundsen Formation. Besides the likelihood of large sand lenses, as encountered in Main Fault, this suggests enhanced likelihood of fluid mobility near the fault centre, particularly near relay zones. Following Færseth et al. (2007), the probability for a breached seal is around 40-60% when calibrated towards for the Aurora F1 setting. On a different note, this setting also forwards scenario IV, as fluids may access the through-going slip surface and thereby be able to bypass the top-seal.

6.8 Further research

This study evaluated methods used to assess across-fault juxtaposition and membrane seal in the context of seismic data using fault F1 of the Aurora CO₂ storage site as a base case. By thoroughly analyzing and categorizing fault facies of outcrop faults in similar sedimentary units (faults in Floy Canyon, Utah), various methods assessing sealing capability can be compared

and evaluated. Several avenues of research could strengthen the learning value of combined fault data applied in subsurface analysis:

1. Find ways to use fault outcrop analogue data in fault reservoir models and simulations. For instance, by collecting a large database of faults facies with architecture, and upload this information as input to a machine learning program, one would generate best-fit models of fault cores by that could feed into reservoir and seismic fault interpretation etc. This approach has similarities to an Artificial Intelligence (AI) Image Generator (Goodfellow et al., 2016).
2. Calibrate deformation band permeabilities of cataclastic and disaggregation bands with bands cored in drill holes of the Aurora sandstone, to find the expected impact of these bands. This may require additional coring as new wells are drilled in the area. How do they affect the fluid migration emphasizing on deformation bands in cluster? Will clusters of cataclastic bands act as a baffle for fluid flow?
3. To strengthen the value of the analogue of the Floy Canyon faults, one could analyse the percentage of clay material in the layers made up of silt and heterolithic mixture of silt and mud in Floy Canyon (volumetric shale fraction). This would guide better constrained, new SGR values more similar to those established from drill hole logging.
4. Design and test a 3D geomodel of the F1 fault of the Aurora storage site in dynamic pressure and fluid simulations. Model designs could vary from simple SGR-type faults to complex fault architecture like ones observed in Floy Canyon. This would allow detailed comparison of differences in fluid flow as well as assessments of the impacts by the elements included in various models.

7 Conclusion

This study investigates fault outcrop analogues to analyze the fault facies architecture of faults with minimal resolution limits. This allows novel analyses of smaller-scale fault, F1 in the Aurora storage site, which will be the first fault the migrating CO₂ plume will encounter in the scheduled CCS operation, commencing in 2024 using the 31/5-7 well as an injector. The findings from this multidisciplinary study show that fault interpretation can be vastly different when comparing outcrop and seismic data.

- The study areas of the Aurora storage site and Floy Canyon have similar depositional environments. In the Book cliffs, the prograding Blackhawk Formation into the Mancos shale illustrates wave-dominated to fluvial-influenced deltaic to shelf facies. Likewise, the upper Jurassic target formations and groups in the Horda Platform contain continental and fluvial-deltaic to shallow-marine deposits.
- The most significant differences in the stratigraphy and the faults in Floy Canyon compared to the F1 fault of the Aurora storage site are (i) smaller sequences in the interbedding from the logging in Floy Canyon than in the target formations in the Aurora storage site. (ii) Presence of coal is prominent in the Blackhawk Formation, unlike the Aurora storage site that is without coal in the stratigraphy. (iii) During fault activity, the burial depth in the Floy Canyon is less than 100 m, while the F1 fault in the Aurora storage was buried to near 1 km.
- The seismic interpretation of the F1 fault in the Aurora storage site shows a continuous and fairly uniform fault plane, likely hosting 3 vertical breached relay zones. The largest throw is 35 m in the center of the fault plane.
- Due to the limit of seismic resolution, extracts of the throw from seismic mapping contain restrictions on the actual length of faults. The total missing fault tip length that has been calculated must be considered in reservoir model simulations.
- The missing fault length was calculated for each target horizon. Adding to the fault length creates a more realistic fault geometry that does not follow the Schematic illustration of an elliptical fault model.
- The average true fault length for the F1 fault in the Aurora storage site is 5803 m, while the observed fault length from seismic interpretation is 3544 m. This leaves a distance between the F1 fault and the injection well 31/5-7 to 160 m.

- Five faults in Floy Canyon (FC) with throw that ranges from 2 to 58 m were thoroughly studied. Fault cores classify into three types of fault facies elements: discrete structures, membranes and lenses. Two faults with the smallest throw sizes (FC faults F1 and F4) have no continuous principal slip plane, while the other three with larger throws are fully connected. Each fault contains one or more lenses. F2 and F3 contain continuous membranes along the principal slip plane, while F1 is semi-continuous. The other three faults have discontinuous membranes. Lower shear-strength lithologies (coal and mud) from the hanging wall and footwall tend to drag.
- The deformation bands seen in the hanging wall of F4 in Floy Canyon are mainly mildly cataclastic shear compaction bands, which goes against the thumb-of-rule that cataclasis dominates deeper than 1 km (burial < 100 m).
- The SGR values for the faults in Floy Canyon were calculated for a point in the outcrop. While the SGR method is commonly applied for a 3D surface in seismic data, these SGR values suggest a high likelihood for seal. In contrast, two out of the five faults studied in Floy Canyon appear open to fluid flow. Besides, only two of the studied faults in Floy Canyon are considered to have continuous membranes along the principal fault plane.
- Results show that the SGR method appear valid when the source layer with sealing lithology is thick instead of smaller scattered units.
- The fault seal assessment of the faults in Floy Canyon shows possible sand-sand communication in the fault core, where sand lenses act as a migration bridge for a cross-fault migration. Similarly, this could exist within the primary storage unit in the F1 fault, Aurora storage site, in terms of the thinner overlying source layer and the abundant sandstone layers in the offset lithologies.
- A general learning is that several sites and/or zones of across- and up-fault fluid migration can be identified when outcrop and seismic data on faults are combined, challenging the viability of the SGR predictions without deeper assessments of the fault in question.

Reference list

- Allan, U. S. (1989) Model for hydrocarbon migration and entrapment within faulted structures. *AAPG Bulletin*, 73 (7), pp 803-811.
- Allen, G. P. & Chambers, J. L. C. (1998) Sedimentation in the Modern and Miocene Mahakam Delta. In G. P. Allen & J. L. C. Chambers (Eds.), *Sedimentation in the modern and Miocene Mahakam delta* (pp 79-89). Indonesian Petroleum Association.
- Bachu, S. (2000). Sequestration of CO₂ in geological media: criteria and approach for site selection in response to climate change. *Energy Conversion & Management*, 41 (9), pp 953-970.
- Bacon, M., Simm, R., & Redshaw, T. (2003) 3-D Seismic Interpretation. *Cambridge University Press*, pp 1-225.
- Bailey, L., Drake, H., Whitehouse, M. & Reiners, P. (2022) Characteristics of red bed bleaching by hydrocarbon migration: A natural example from the Entrada sandstone, southern Utah. *Geochemistry, Geophysics, Geosystems*, 23 (8).
- Balsley, J. K. (1982) Cretaceous wave dominated delta systems: Book Cliffs, east central Utah. *Unpublished American Association of Petroleum Geologists Guidebook*.
- Barnett, J. A. M., Mortimer, J., Rippon, J. H., Walsh, J. J., Watterson, J. (1987) Displacement Geometry in the Volume Containing a Single Normal Fault. *AAPG Bulletin*, 71 (8), pp 925–937.
- Bastesen, E. & Braathen, A. (2010). Facies composition and scaling relationships of extensional faults in carbonates. *Journal of Structural Geology*, 32, pp 1609-1628.
- Bauer, J.F., Krumbholz, M., Meier, S. & Tanner, D. C. (2017) Predictability of properties of a fractured geothermal reservoir: the opportunities and limitations of an outcrop analogue study. *Geotherm Energy*, 5, pp 1-27
- Bhattacharya, J. & Davies, R. K. (2004). Sedimentology and Structure of Growth Faults at the Base of the Ferron Sandstone Member Along Muddy Creek, Utah. *AAPG Studies in Geology*, 50, pp 279-304.
- Bense, V. F., Gleeson, T., Loveless, S. E., Bour, O. & Scibek, J. (2013) Fault zone hydrogeology. *Earth-Science Reviews*, 127, pp 171-192.
- Bjørlykke, K. (1993) Fluid flow in sedimentary basins. *Sedimentary Geology*, 86 (1-2), pp 137-158.
- Bjørlykke, K. & Høeg, K. (1997), Effects of burial diagenesis on stresses, compaction and fluid flow in sedimentary basins. *Marine and Petroleum Geology*, 14, pp 267–276.
- Bond, C.E. (2015). Uncertainty in Structural Interpretation: Lessons to be learnt. *Journal of Structural Geology*, 74, 185-200.

- Botter, C. D. (2016) Seismic Imaging of Fault Zones: A synthetic workflow to study the impact of faults on seismic images (Publication No. 293) [PhD thesis, The University of Stavanger, Norway].
- Bouvier, J., Kaars-Sijpesteijn, C., Kluesner, D., Onyejekwe, C. & Van der Pal, R. (1989) Three- dimensional seismic interpretation and fault sealing investigations, Nun River Field, Nigeria. *AAPG bulletin*, 73 (11), pp 1397-1414.
- Braathen, A., Tveranger, J., Fossen, H., Skar, T., Cardozo, N., Semshaug, S.E., Bastesen, E., & Sverdrup, E. (2009). Fault facies and its application to sandstone reservoirs. *AAPG Bulletin*, 93, 891-917.
- Braathen, A., Osmundsen, P. T., Hauso, H., Semshaug, S., Fredman, N. & Buckley, S. (2013) Fault-induced deformation in a poorly consolidated, siliciclastic growth basin: A study from the Devonian in Norway. *Tectonophysics*, 586, pp 112–129.
- Braathen, A., Midtkandal, I., Mulrooney, M.J., Appleyard, T.R., Haile, B.G. & Yperen, A.E. (2018) Growth-faults from delta collapse – structural and sedimentological investigation of the Last Chance delta, Ferron Sandstone, Utah. *Basin Research*, 30 (4), pp 688–707.
- Braathen, A., Petrie, E., Nystuen, T., Sundal, A., Skurtveit, E., Zuchuat, V., Gutierrez, M. & Midtkandal, I. (2020) Interaction of deformation bands and fractures during progressive strain in monocline -San Rafael Swell, Central Utah, USA. *Journal of Structural Geology*, 141.
- Brekke, H., Sjulstad, H., Magnus, C. & Williams, R. (2001) Sedimentary Environments Offshore Norway–Palaeozoic to Recent. *Norwegian Petroleum Society Special Publications*, 10 pp 7-37.
- Bretan, P., Yielding, G. & Jones, H. (2003) Using calibrated shale gouge ratio to estimate hydrocarbon column heights. *American Association of Petroleum Geologists Bulletin*, 87 (3), pp 397-413.
- Bretan, P., Yielding, G., Mathiassen, O. M. and Thorsnes, T. (2011) Fault-seal analysis for CO₂ storage: an example from the Troll area, Norwegian Continental Shelf. *Petroleum Geoscience*, 17 (2), pp 181-192.
- Brown, A. R. (2011) *Interpretation of three-dimensional seismic data*. 7 ed. Tulsa: The AAPG and the Society of Exploration Geophysicists.
- Bump, A. P. & Davis, G. H. (2003) Late Cretaceous–early Tertiary Laramide deformation of the northern Colorado Plateau, Utah and Colorado. *Journal of Structural Geology*, 25 (3), pp 421-440.
- Caine, J. S. & Forster, C. B. (1999) Fault Zone Architecture and Fluid Flow: Insights from Field Data and Numerical Modeling. *Geophysical Monograph Series*, 113, pp 101-127.
- Caine, J. S., Evans, J. P & Forster, C. B. (1996) Fault zone architecture and permeability structure. *Geology*, 24 (11), pp 1025–1028.

- Chan, M. A., Newman, S. L. & May, F. E. (1991) Deltaic and shelf deposits in the Cretaceous Blackhawk Formation and Mancos Shale, Grand County, Utah. *Utah Geological Survey, Miscellaneous Publication*, 91(6).
- Childs, C., Manzocchi, T., Walsh, J. J., Bonson, C. G., Nicol, A. & Schöpfer, M. P. J. (2009) A geometric model of fault zone and fault rock thickness variations. *Journal of Structural Geology*, 31, pp 117-127.
- Cramer, F., Shephard, G. E. and Heron, P. J. (2020) The misuse of colour in science communication. *Nature communications*, 11 (1), pp 1-10.
- Cross, W. (1899) Telluride quadrangle, Colorado: U.S. *Geological Survey Geological Atlas, Folio 57*, p. 18.
- Cunningham, J. E., Cardozo, N., Townsend, C. & Callow, R. H. T. (2021) The impact of seismic interpretation methods on the analysis of faults: a case study from the Snøhvit field, Barents Sea. *Solid Earth*, 12, pp 741–764.
- Currie, B. S. (1997) Sequence stratigraphy of nonmarine Jurassic–Cretaceous rocks, central Cordilleran foreland-basin system. *Geological Society of America Bulletin*, 109 (9), pp 1206-1222.
- Currie, B. S. (2002) Structural configuration of the Early Cretaceous Cordilleran foreland-basin system and Sevier thrust belt, Utah and Colorado. *The Journal of Geology*, 110, 697-718.
- Davis, G. H. 1978. Monocline fold pattern of the Colorado Plateau. In Vincent Matthews (Ed.), *Laramide folding associated with basement block faulting in the western United States*: Geological Society of America Memoir, 151, 215-233.
- Davis, G.H., & Bump, A.P. (2009) Structural geologic evolution of the Colorado Plateau. In S.M. Kay, V.A. Ramos & W.R. Dickinson (Eds.), *Backbone of the Americas: Shallow Subduction, Plateau Uplift, and Ridge and Terrane Collision* (204, pp 99–124). Geological Society of America Memoir.
- Davies, R.C., Howell, J.A., Boyd, R., Flint, S.S., & Diessel, C.F. (2006). High-resolution sequence-stratigraphic correlation between shallow-marine and terrestrial strata: Examples from the Sunnyside Member of the Cretaceous Blackhawk Formation, Book Cliffs, eastern Utah. *AAPG Bulletin*, 90, 1121-1140.
- Davies, R. J., Turner, J. & Underhill, J. R. (2001) Sequential dip-slip fault movement during rifting: a new model for the evolution of the Jurassic trilete North Sea rift system. *Petroleum Geoscience*, 7 (4), pp 371-388.
- DeCelles, P.G., & Coogan, J.C. (2006). Regional structure and kinematic history of the Sevier fold-and-thrust belt, central Utah. *Geological Society of America Bulletin*, 118, pp 841-864.
- Deegan, C. & Scull, B. (1977) *A standard lithostratigraphic nomenclature for the central*

- and the northern North Sea*. Norwegian Petroleum Directorate Bulletin 1. Available: <https://www.npd.no/globalassets/1-mpd/publikasjoner/mpd-bulletins/mpd-bulletin-1-1977.pdf> [Accessed 03.04.2023].
- Dennis, J. G. (1967) *International tectonic dictionary: English terminology*. 1 ed. Tulsa: American Association of Petroleum Geologists.
- Desjardins, P., Buatois, L. & Mangano, M. (2012). Tidal Flats and Subtidal Sand Bodies. In D. Knaust, R. G. Bromley (Eds.) *Trace Fossils as Indicators of Sedimentary Environments* (64 pp. 529-561) *Developments in Sedimentology*.
- Dickinson, W. R., Klute, M. A., Hayes, M. J., Janecke, S. U., Lundin, E. R., Mckittrick, M. A. & Olivares, M. D. (1988) Paleogeographic and paleotectonic setting of Laramide sedimentary basins in the central Rocky Mountain region. *Geological Society of America Bulletin*, 100 (7), pp 1023-1039.
- Edmonds, D. A. & Slingerland, R. L. (2007) Mechanics of river mouth bar formation: Implications for the morphodynamics of delta distributary networks. *Journal of Geophysical Research*, 112
- Equinor (2019) Northern Lights Project Concept report. Equinor. Available: <https://northernlightsccs.com/wp-content/uploads/2021/03/Northern-Lights-Project-Conceptreport.pdf> [Accessed 07.03.2022].
- Færseth, R. (1996) Interaction of Permo-Triassic and Jurassic extensional fault-blocks during the development of the northern North Sea. *Journal of Geological Society*, 153 pp 931-944.
- Færseth, R. B., Gabrielsen, R. H. & Hurich, C. A. (1995) Influence of basement in structuring of the North Sea basin, offshore southwest Norway. *Norwegian Journal of Geology*, 75 (2-3), pp 105- 119.
- Færseth, R. B. (2006) Shale smear along large faults: Continuity of smear and the fault seal capacity. *Journal of the Geological Society (London)*, 163, pp 741–751.
- Færseth, R. B., Johnsen, E. & Sperrevik, S. (2007). Methodology for risking fault seal capacity: Implications of fault zone architecture. *AAPG bulletin* 91(9), pp 1231-1246.
- Faleide, J. I., Bjørlykke, K. & Gabrielsen, R. H. (2010) Geology of the Norwegian continental shelf, In K. Bjørlykke (Ed.) *Petroleum Geoscience: From Sedimentary Environments to Rock Physics* (pp 467-499). Heidelberg: Springer.
- Faleide, J. I., Kyrkjebø, R., Kjennerud, T., Gabrielsen, R. H., Jordt, H., Fanavoll, S. & Bjerke, M. D. (2002) Tectonic impact on sedimentary processes during Cenozoic evolution of the northern North Sea and surrounding areas. *Special Publication- Geological Society of London*, 196 pp 235-270.
- Faleide, T. S., Braathen, A., Lecomte, I. C., Mulrooney, M. J., Midtkandal, I., Bugge, A. J. & Planke, S. (2021) Impacts of seismic resolution on fault interpretation: Insights from seismic modelling. *Tectonophysics*, 816, pp 1-19.

- Faleide, T. S., Midtkandal, I., Planke, S., Corseri, R., Faleide, J. I., Serck, C. & Nystuen, J. (2019) Characterisation and development of Early Cretaceous shelf platform deposition and faulting in the Hoop area, southwestern Barents Sea—constrained by high-resolution seismic data. *Norwegian Journal of Geology*, 99 (3), pp 1-20.
- Faulkner, D.R., Jackson, C.A., Lunn, R.J., Schlische, R.W., Shipton, Z.K., Wibberley, C., & Withjack, M.O. (2010) A review of recent developments concerning the structure, mechanics and fluid flow properties of fault zones. *Journal of Structural Geology*, 32 (11), pp 1557-1575.
- Fazlikhani, H., Fossen, H., Gawthorpe, R. L., Faleide, J. I., & Bell, R. E. (2017) Basement structure and its influence on the structural configuration of the northern North Sea rift, *Tectonics*, 36 (6), pp 1151– 1177.
- Fisher, Q. J. & Knipe, R. J. (1998) Fault sealing processes in siliciclastic sediments. *Geological Society, London, Special Publications*, 147 (1), pp 117-134.
- Flint, S., J. Howell, S. Knight & Tilbrook, A. (1997). *Incised valley-fills from the Brent Group, Northwest Hutton field, North Sea; a comparison of geometries and fill characteristics with those of the Cretaceous Blackhawk Formation, Book Cliffs, Utah*. Proceedings of the 18th GCSEPM Research Conference, Houston, pp 107-116.
- Fossen, H. (2016) *Structural Geology* (2th ed). Cambridge University Press, Cambridge.
- Fossen, H. (2020) Fault classification, fault growth and displacement. In N. Scarselli, J. Adam, D. Chiarella, D. G. Roberts & A. W. Bally (Eds.), *Regional Geology and Tectonics: Principles of Geologic Analysis* (pp.119-147). Elsevier.
- Fossen, H., Schultz, R., Shipton, Z. & Mair, K. (2007) Deformation bands in sandstone – a review. *Journal of the Geological Society, London*, 164, pp 755-769.
- Fossen, H. & Rotevatn, A. (2016). Fault linkage and relay structures in extensional settings-A review. *Earth-Science Reviews*, 154.
- Fossen, H., Soliva, R., Ballas, G., Trzaskos, B., Cavalcante, C. & Schultz, R. A. (2017) A review of deformation bands in reservoir sandstones: geometries, mechanisms and distribution. *Geological Society, London, Special Publications*, 459, pp 9-33.
- Freund, P., & Ormerod, W. G. (1997) PROGRESS TOWARD STORAGE OF CARBON DIOXIDE. *Energy conversion and management*, 38, pp 199-204.
- Fristad, T., Groth, A., Yielding, G. & Freeman, B. (1997) Quantitative fault seal prediction: a case study from Oseberg Syd, In Møller-Pedersen, P. and Koestler, A. G. (ed.) *Hydrocarbon Seals: Importance for Exploration and Production*. Singapore: Norwegian Petroleum Society Special Publications, Elsevier, pp 107-124.
- Fulljames, J. R., Zijerveld, L. J. J, Franssen, C., Ingram, G. & Richard, P. (1996) Fault seal

- processes: systematic analyses of fault seals over geological and production timescales, *In* Møller- Pedersen, P. and Koestler, A. G. (ed.) *Hydrocarbons Seals: Importance for Exploration and Production*. Singapore: Norwegian Petroleum Society Special Publication, Elsevier, pp 51-59.
- Furre, A. K., Meneguolo, R., Pinturier, L. & Bakke, K. (2020) Planning deep subsurface CO₂ storage monitoring for the Norwegian full-scale CCS project. *First Break*, 38 (10), pp 55-60.
- Gabrielsen, R. H., Kyrkjebø, R., Faleide, J. I., Fjeldskaar, W. & Kjennerud, T. (2001) The Cretaceous post-rift basin configuration of the northern North Sea. *Petroleum Geoscience*, 7 (2), pp 137- 154.
- Garzanti, E., Radeff, G. & Malusà, M. G. (2018) Slab breakoff: A critical appraisal of a geological theory as applied in space and time. *Earth-Science Reviews*, 177, pp 303-319.
- Gassnova (2012) *Geological storage of CO₂ from Mongstad. Interim report Johansen Formation*. Report TL02-GTL-Z-RA-0001. Gassnova and Ross Offshore. Available: <https://ccsnorway.com/earlier-norwegian-ccs-projects/> [Accessed 04.04.2023].
- Global CCS institute (2021) Global status of CCS 2021. Available: <https://www.globalccsinstitute.com/resources/global-status-report/download/> [Accessed 08.04.2022].
- Goodfellow, I. J., Bengio, Y. & Courville, A (2016). *Deep learning*. MIT Press
- Hampson, G. J. & Howell, J. A. (2005) Sedimentologic and Geomorphic Characterization of Ancient Wave-Dominated Deltaic Shorelines: Upper Cretaceous Blackhawk Formation, Book Cliffs, Utah, U.S.A. In L. Giosan & J. P. Bhattacharya (Eds.), *River Deltas—Concepts, Models, and Examples* (83, pp 133-154). SEPM Society for Sedimentary Geology.
- Hatton, C. G, Main, I. G., Meredith, P. G. (1994) Non-universal scaling of fracture length and opening displacement. *Nature*, 367, pp 160–162.
- Heath, J.E., Lachmar, T.E., Evans, J.P., Kolesar, P.T. & Williams, A.P. (2009). Hydrogeochemical Characterization of Leaking, Carbon Dioxide-Charged Fault Zones in East-Central Utah, With Implications for Geologic Carbon Storage. In B.J. McPherson & E.T. Sundquist (Eds.), *Carbon Sequestration and Its Role in the Global Carbon Cycle* (183, pp 147-158). American Geophysical Union.
- Hecker, S. (1993) Quaternary tectonics of Utah with emphasis on earthquake-hazard characterization. *Utah Geological Survey Bulletin*, 127, pp 157.
- Herron, D. A. (2011) *First steps in seismic interpretation*. 1 ed. Tulsa: Society of Exploration Geophysicists.
- Hettinger, R.D., & Kirschbaum, M.A. (2002). *Stratigraphy of the Upper Cretaceous Mancos*

- Shale (upper part) and Mesaverde Group in the southern part of the Uinta and Piceance basins, Utah and Colorado*. IMAP 2764. USGS Numbered Series. Available: <https://pubs.er.usgs.gov/publication/i2764> [Accessed 05.05.2023].
- Hintze, L. F. (1988) *Geological History of Utah*. Brigham Young University Geology Studies, Special Publication 7.
- Holden, N. (2021). *Structural characterization and acrossfault seal assessment of the Aurora CO2 storage site, northern North Sea* [Masteroppgave, Universitetet i Oslo]. DUO – Digitale Utgivelser ved UiO, pp 1-161.
- Holden, N., Osmond, J. L., Mulrooney M. J., Braathen, A., Skurtveit E., & Sundal, A. (2022) Structural characterization and across-fault seal assessment of the Aurora CO2 storage site, northern North Sea. *Petroleum Geoscience*, 28 (4).
- Hospers, J. & Ediriweera, K. K. (1991) Depth and configuration of the crystalline basement in the Viking Graben area, northern North Sea. *Journal of the Geological Society of London* 148, pp 261-265.
- Howell, J., Martinius, A. & Good, T. (2014) The application of outcrop analogues in geological modelling: a review, present status and future outlook. *Geological Society, London, Special Publications*, 387, pp 1-25.
- Humphreys, E. D. (1995) Post-Laramide removal of the Farallon slab, western United States. *Geology*, 23 (11), pp 987–990.
- IEA (2021) *Net Zero by 2050*. International Energy Agency. Available: <https://www.iea.org/reports/net-zero-by-2050> [Accessed 06.03.2022].
- IPCC (2005) *IPCC Special Report on Carbon Dioxide Capture and Storage*. B. Metz, O. Davidson, H. Coninck, M. Loos & L. Meyer (Eds.) Cambridge University Press, UK.
- IPCC (2018) *Global warming of 1.5 C*. An IPCC Special Report. Intergovernmental Panel on Climate Change Special Report. Available: <https://www.ipcc.ch/sr15/> [Accessed 08.04.2022].
- Kauffman, E. G. (1977) Geological and biological overview: Western Interior Cretaceous Basin, in Cretaceous facies, faunas, and paleoenvironments across the Western Interior Basin. *The Mountain Geologist*, 14, pp 75-99.
- Kim, Y.-S. & Sanderson, D. J. (2005) The relationship between displacement and length of faults: a review. *Earth-Science Reviews*, 68 (3-4), pp 317-334.
- Knipe, R. J. (1997) Juxtaposition and seal diagrams to help analyze fault seals in hydrocarbon reservoirs. *AAPG Bulletin*, 81 (2), pp 187-195.
- Knipe, R. J., Q. J. Fisher, G. Jones, M. R. Clennell, A. B. Farmer, A. Harrison, B. Kidd, E. McAllister, J. R. Porter, & E. A. White. (1997) Fault seal analysis: Successful methodologies, application and future directions. In A. G. Koestler and R. Hunsdale (Eds.), *Hydrocarbon seal quantification: Norwegian Petroleum Society (NPF Special Publication)* (7, pp 15-38). Elsevier.

- Lindanger, M., Roy H. Gabrielsen & Alvar Braathen. (2007) Analysis of rock lenses in extensional faults. *Norwegian Journal of Geology*, 87, pp 361-372.
- Lindsay, N., Murphy, F., Walsh, J. & Watterson, J. (1993) Outcrop studies of shale smears on fault surfaces, In Flint, S. and Bryant, I. (Ed.) *The geological modelling of hydrocarbon reservoirs and outcrop analogues* (pp 113-123). Blackwell Scientific Publications.
- Lipponen, J., McCulloch, S., Keeling, S., Stanley, T., Berghout, N., & Berly, T. (2017) The Politics of Large-scale CCS Deployment. *Energy Procedia*, 114, pp 7581-7595.
- Lohr, T., Krawczyk, C. M., Oncken, O. & Tanner, D. C. (2008) Evolution of a fault surface from 3D attribute analysis and displacement measurements. *Journal of Structural Geology*, 30 (6), pp 690-700.
- Loosveld, R.J.H. & Franssen, R.C.M.W. (1992, November 16-18) *Extensional versus shear fractures - implications for reservoir characterisation*. [Paper presentation] Society of Petroleum Engineers, European Petroleum Conference, Cannes, France, p. 23–30.
- Lyon, P., Boulton, P., Mitchell, A. & Hillis, R. (2004) Improving fault geometry interpretation through 'pseudo-depth' conversion of seismic data in the Penola Trough, Otway Basin, In Boulton, P., Johns, D. and Lang, S. (ed.) *Eastern Australian Basin Symposium II* (pp 395-706). Adelaide: Petroleum Exploration Society of Australia, Special Publication.
- Marchal, D.A., Guiraud, M., & Rives, T. (2003). Geometric and morphologic evolution of normal fault planes and traces from 2D to 4D data. *Journal of Structural Geology*, 25, pp 135-158.
- Marjanac, T. & Steel, R. J. (1997) Dunlin Group sequence stratigraphy in the northern North Sea: a model for Cook Sandstone deposition. *AAPG bulletin*, 81 (2), pp 276-292.
- Marrett, R. & Allmendinger, R.W. (1991) Estimates of strain due to brittle faulting: sampling of fault populations. *Journal of Structural Geology*, 13 (6), pp 735-738.
- Martz, J., Kirkland, J.I., Milner, A.R., Parker, W.G., & Santucci, V.L. (2017) Upper Triassic lithostratigraphy, depositional systems, and vertebrate paleontology across southern Utah. *Geology of the Intermountain West*, 4, pp 99-180.
- Meneguolo, R., Sundal, A., Martinius, A.W., Veselovsky, Z., Cullum, A. and Milovanova, E. (2022) Impact of the lower Jurassic Dunlin Group depositional elements on the Aurora CO2 storage site, EL001, northern North Sea, Norway. *International Journal of Greenhouse Gas Control*, 119.
- Michie, E.A.H., Mulrooney, M.J. & Braathen, A. (2021) Fault interpretation uncertainties using seismic data, and the effects on fault seal analysis: a case study from the Horda platform, with implications for CO2 storage. *Solid Earth*, 12, pp 1259–1286.
- Michie, E.A.H & Braathen, A. (in press) Strategies to De-Risk Faults in the Subsurface for CO2 Storage: A Case Study from the Northern Horda Platform

- Miocic, J., Johnson, G. & Bond, C. E. (2019) Uncertainty in fault seal parameters: implications for CO₂ column height retention and storage capacity in geological CO₂ storage projects. *Solid earth*, 10 pp 951-967.
- Mitchell, T., Faulkner, D. (2012) Towards quantifying the matrix permeability of fault damage zones in low porosity rocks. *Earth and Planetary Science Letters*, 339-340, pp 24-31.
- Mulrooney, M. J., Osmond, J. L., Skurtveit, E., Faleide, J. I. & Braathen, A. (2020) Structural analysis of the Smeaheia fault block, a potential CO₂ storage site, northern Horda Platform, North Sea. *Marine and Petroleum Geology*, 121, pp 104598.
- NCCS (2021) *Norwegian CCS Research Centre (NCCS)-Annual Report 2021*. Sintef Report. Available: https://www.sintef.no/globalassets/sintef-energi/nccs/annual-report/nccs_2021_hr.pdf [Accessed 27.04.2023].
- Nicol, A., Watterson, J., Walsh, J.J., & Childs, C. (1996). The shapes, major axis orientations and displacement patterns of fault surfaces. *Journal of Structural Geology*, 18, pp 235-248.
- Norwegian Ministry of Petroleum and Energy (2020) *Longship – Carbon capture and storage. Meld. St. 33 Report to the Stortinget (white paper)*. Available: <https://www.regjeringen.no/en/dokumenter/meld.-st.-33-20192020/id2765361/> [Accessed 10.05 2023].
- NPD (2014) *Norwegian Petroleum Directorate - Geology of the North Sea*. Available: <https://www.npd.no/en/facts/geology/lithostratigraphy/> [Accessed 13.03.2023].
- NPD Factpages (2023) *Norwegian Petroleum Directorate Factpages* [Online]. Available: <https://factpages.npd.no/> [Accessed 06.04 2023].
- O'Byrne, C., & Flint, S. (1996) Interfluvial sequence boundaries in the Grassy Member, Book Cliffs, Utah: criteria for recognition and implications for subsurface correlation, *Geological Society special publication*, 104 (1), pp 207-220.
- Ogata, K., Senger, K., Braathen, A., & Tveranger, J. (2014) Fracture corridors as seal-bypass systems in siliciclastic reservoir-cap rock successions: Field-based insights from the Jurassic Entrada Formation (SE Utah, USA). *Journal of Structural Geology*, 66, pp 162-187.
- Pattison, S. A. J., Williams, H. & Davies, P. (2008) Clastic sedimentology, sedimentary architecture, and sequence stratigraphy of fluvio-deltaic, shoreface, and shelf deposits, Upper Cretaceous, Book Cliffs, eastern Utah and western Colorado. In R. G. Raynolds (Ed.), *Roaming the Rocky Mountains and Environs: Geological Field Trips* (10, pp.17-43). Geological Society of America.
- Peacock, D., Knipe, R. and Sanderson, D. (2000) Glossary of normal faults. *Journal of Structural Geology*, 22 (3), pp 291-305.
- Phillips, T. B., Fazlikhani, H., Gawthorpe, R. L., Fossen, H., Jackson, C. A.-L., Bell, R. E.,

- Faleide, J. I. and Rotevatn, A. (2019) The Influence of Structural Inheritance and Multiphase Extension on Rift Development, the Northern North Sea. *Tectonics*, 38 (12), pp 4099-4126.
- Pickering, G., Peacock, D.C.P., Sanderson, D.J., Bull, J.M. (1997) Modelling tip zones to predict the throw and length characteristics of faults. *Bulletin of American Association of Petroleum Geologists*, 81, pp 82 – 99.
- Putirka, K. & Platt, B. (2012) Basin and Range volcanism as a passive response to extensional tectonics. *Geosphere*, 8 (6), pp 1274–1285.
- Rahman, M. J., Fawad, M., Jahren, J., Mondol, N. H. (2022) Top seal assessment of Drake Formation shales for CO₂ storage in the Horda Platform area, offshore Norway. *International Journal of Greenhouse Gas Control*, 119, pp 103700.
- Ravnås, R. & Steel, R.J. (1997) Contrasting styles of Late Jurassic syn-rift turbidite sedimentation: a comparative study of the Magnus and Oseberg areas, northern North Sea. *Marine and Petroleum Geology*, 14, pp 417–449.
- Renshaw, C.E., & Park, J.C. (1997). Effect of mechanical interactions on the scaling of fracture length and aperture. *Nature*, 386, pp 482-484.
- Rotevatn, A., Tveranger, J., Howell, J.A. and Fossen, H. (2009) Dynamic investigation of the effect of a relay ramp on simulated fluid flow: geocellular modelling of the Delicate Arch Ramp, Utah. *Petroleum Geoscience*, 15(1), pp 45-58.
- Rotevatn, A., Jackson, C. A. L., Tvedt, A. B., Bell, R. E. and Blækkan, I. (2018) How do normal faults grow? *Journal of Structural Geology*, 125, pp 174-184.
- Rustichelli, A., Celma, C. D., Tondi, Tondi, E., Baud, P., & Vinciguerra, S. (2016). Fibrous gypsum veins as diffuse features and within fault zones: the case study of the Pisco Basin (Ica desert, southern Peru). *Journal of the Geological Society*, 173, pp 405-418.
- Schowalter, T. T. (1979) Mechanics of secondary hydrocarbon migration and entrapment. *AAPG bulletin*, 63 (5), pp 723-760.
- Schueller, S., Braathen, A., Fossen, H. & Tveranger, J. (2013) Spatial distribution of deformation bands in damage zones of extensional faults in porous sandstones: Statistical analysis of field data. *Journal of Structural Geology*, 52, pp 148-162.
- Schultz, R.A., & Fossen, H. (2008). Terminology for structural discontinuities. *AAPG Bulletin*, 92, pp 853-867.
- Sellevoll, M. A. (1973) Mohorovičić discontinuity beneath Fennoscandia and adjacent parts of the Norwegian Sea and the North Sea. *Tectonophysics* 20 (1-4), pp 359-366.
- Sheriff, R. E. (1977) Limitations on resolution of seismic reflections and geologic detail derivable from them: Section 1. Fundamentals of Stratigraphic Interpretation of Seismic Data, In Payton, C. (Ed.) *Seismic Stratigraphy – Applications to Hydrocarbon Exploration* (pp 3-14). AAPG Memoir.

- Sheriff, R. E. (2002). Encyclopedic dictionary of applied geophysics (4th ed.). *Society of Exploration Geophysicists*, 13.
- Shipton, Z.K., Evans, J.P., Kirschner, D.L., Kolesar, P.T., Williams, A.P., & Heath, J. (2004) Analysis of CO₂ leakage through ‘low-permeability’ faults from natural reservoirs in the Colorado Plateau, east-central Utah. *Geological Society, London, Special Publications*, 233, pp 43 - 58.
- Shreyash, N., Sonker, M., Bajpai, S., Tiwary, S.K., Khan, M.A., Raj, S., Sharma, T., Biswas, S. (2021) The Review of Carbon Capture-Storage Technologies and Developing Fuel Cells for Enhancing Utilization. *Energies*, 14 (16), pp 1-34.
- Steel, R. (1993) Triassic–Jurassic megasequence stratigraphy in the Northern North Sea: rift to post-rift evolution. *Geological Society, London, Petroleum Geology Conference series*. Geological Society of London, 4 (1), pp 299-315.
- Stokes, W.·L. (1986) Geology of Utah: Utah Museum of Natural History and Utah Geological and Mineral Survey, p 280
- Sundal, A., Miri, R., Ravn, T. and Aagaard, P. (2015) Modelling CO₂ migration in aquifers; considering 3D seismic property data and the effect of site-typical depositional heterogeneities. *International Journal of Greenhouse Gas Control*, 39, pp 349-365.
- Sundal, A., Nystuen, J. P., Rørvik, K.-L., Dypvik, H. and Aagaard, P. (2016) The Lower Jurassic Johansen Formation, northern North Sea–Depositional model and reservoir characterization for CO₂ storage. *Marine and Petroleum Geology*, 77, pp, 1376-1401.
- Torabi, A. (2014) Cataclastic bands in immature and poorly lithified sandstone, examples from Corsica, France. *Tectonophysics*, 630, pp 91-102.
- Torabi, A., & Berg, S.S. (2011) Scaling of fault attributes: A review. *Marine and Petroleum Geology*, 28, pp 1444-1460.
- Torabi, A., Alaei, B., & Libak, A. (2019). Normal fault 3D geometry and displacement revisited: Insights from faults in the Norwegian Barents Sea. *Marine and Petroleum Geology*, 99, 135-155.
- Torabi, A., Balsamo, F., Nogueira, F., Vasconcelos, D., Silva, A., Bezerra, F & Souza, J. (2021) Variation of thickness, internal structure and petrophysical properties in a deformation band fault zone in siliciclastic rocks. *Marine and Petroleum Geology*, 133 (10).
- Torsvik, T. H., Carlos, D., Mosar, J., Cocks, L. R. M. and Malme, T. (2002) Global reconstructions and North Atlantic paleogeography 440 Ma to recent, *In Eide, E. (Ed.) BATLAS–Mid Norway plate reconstruction atlas with global and Atlantic perspectives* (pp 18-39). Trondheim: Geological Survey of Norway.
- Torp, T. A. and Gale, J. (2004) Demonstrating storage of CO₂ in geological reservoirs: The Sleipner and SACS projects. *Energy*, 29 (9-10), pp 1361-1369.

- Trudgill, B. and Cartwright, J. (1994) Relay-ramp forms and normal-fault linkages, Canyonlands National Park, Utah. *Geological Society of America Bulletin*, 106(9), pp.1143-1157.
- UGS (n.d.) Popular geologic history. Available: <https://geology.utah.gov/popular/geologic-history/#toggle-id-1> [Accessed 07.02.2023]
- Underhill, J. R. & Partington, M. (1993) Jurassic thermal doming and deflation in the North Sea: implications of the sequence stratigraphic evidence. *Geological Society, London, Petroleum Geology Conference Series*. Geological Society of London, 4 (1), pp 337-345.
- Vermilye, J.M., Scholz, C.H. (1995) Relation between vein length and aperture. *Journal of Structural Geology*, 17 (3), pp 423–434.
- Vollset, J. and Doré, A. (1984) *A revised Triassic and Jurassic lithostratigraphic nomenclature for the Norwegian North Sea*. Norwegian Petroleum Directorate Bulletin 3. Available: <https://www.npd.no/globalassets/1-npd/publikasjoner/npd-bulletins/npd-bulletin-3-1984.pdf> [Accessed 03.04.23].
- Walker, R. G. (1984) Shelf and shallow marine sands. In R.G., Walker, (Ed.), *Facies models* (2nd ed., pp 141-170) Geoscience Canada Reprint Series 1.
- Walsh, John J. & Watterson, Juan. (1988) Analysis of the relationship between displacements and dimensions of faults. *Journal of Structural Geology*, 10, pp 239-247.
- Walsh, John J. & Watterson, Juan & Yielding, Graham. (1991) The importance of small-scale faulting in regional extension. *Nature*, 351, pp 391-393.
- Walsh, J., Watterson, J., Heath, A., Gillespie, P. & Childs, C. (1998) Assessment of the effects of sub-seismic faults on bulk permeabilities of reservoir sequences. *Geological Society, London, Special Publications*, 127, pp 99–114.
- Warren, J.K. (2006) *Evaporites: Sediments, Resources and Hydrocarbons*. Springer, Berlin.
- Watts, N. (1987) Theoretical aspects of cap-rock and fault seals for single-and two-phase hydrocarbon columns. *Marine and Petroleum Geology*, 4 (4), pp 274-307.
- Whipp, P., Jackson, C. L., Gawthorpe, R., Dreyer, T. & Quinn, D. (2014) Normal fault array evolution above a reactivated rift fabric; a subsurface example from the northern Horda Platform, Norwegian North Sea. *Basin Research*, 26 (4), pp 523-549.
- Wills, B. J. & Gabel, S. (2001) Sharp-based, tide-dominated deltas of the Sego Sandstone, Book Cliffs, Utah, USA. *Sedimentology*, 48 (3), pp 479-506.
- Woodcock, N.H., & Mort, K. (2008) Classification of fault breccias and related fault rocks. *Geological Magazine*, 145, pp 435 - 440.
- Yielding, G. (2002) Shale gouge ratio—Calibration by geohistory, In Koestler, A. G. and

-
- Hundsdale, R. (ed.) *Norwegian Petroleum Society Special Publications* (pp 1-15), Amsterdam: Elsevier.
- Yielding, G., Freeman, B. & Needham, D. T. (1997) Quantitative fault seal prediction. *AAPG Bulletin*, 81 (6), pp 897-917.
- Yielding, G., Bretan, P. & Freeman, B. (2010) Fault seal calibration: a brief review. *Geological Society, London, Special Publications*, 347 (1), pp 243-255.
- Young, R. G. (1955) Sedimentary facies an intertonguing in the Upper Cretaceous of the Book Cliffs, Utah-Colorado. *Geological Society of America Bulletin*, 66, pp 177-202.
- Ziegler, P. (1975) Geologic evolution of North Sea and its tectonic framework. *AAPG bulletin*, 59 (7), pp 1073-1097.
- Zuchuat, V., Sleveland , A., Sprinkel , D., Rimkus , A., Braathen , A., and Midtkandal , I. (2018) New Insights on the Impact of Tidal Currents on a Low-gradient, Semi-enclosed, Epicontinental Basin—the Curtis Formation, East-central Utah, USA. *Geology of the Intermountain West*, 5, pp 131-165.
- Zuchuat, V., Sleveland, A.R., Pettigrew, R.P., Dodd, T.J., Clarke, S.M., Rabbel, O., Braathen, A., & Midtkandal, I. (2019). Overprinted allocyclic processes by tidal resonance in an epicontinental basin: The Upper Jurassic Curtis Formation, east-central Utah, USA. *The Depositional Record*, 5, pp 272 - 305.

Appendix

Sedimentary log A

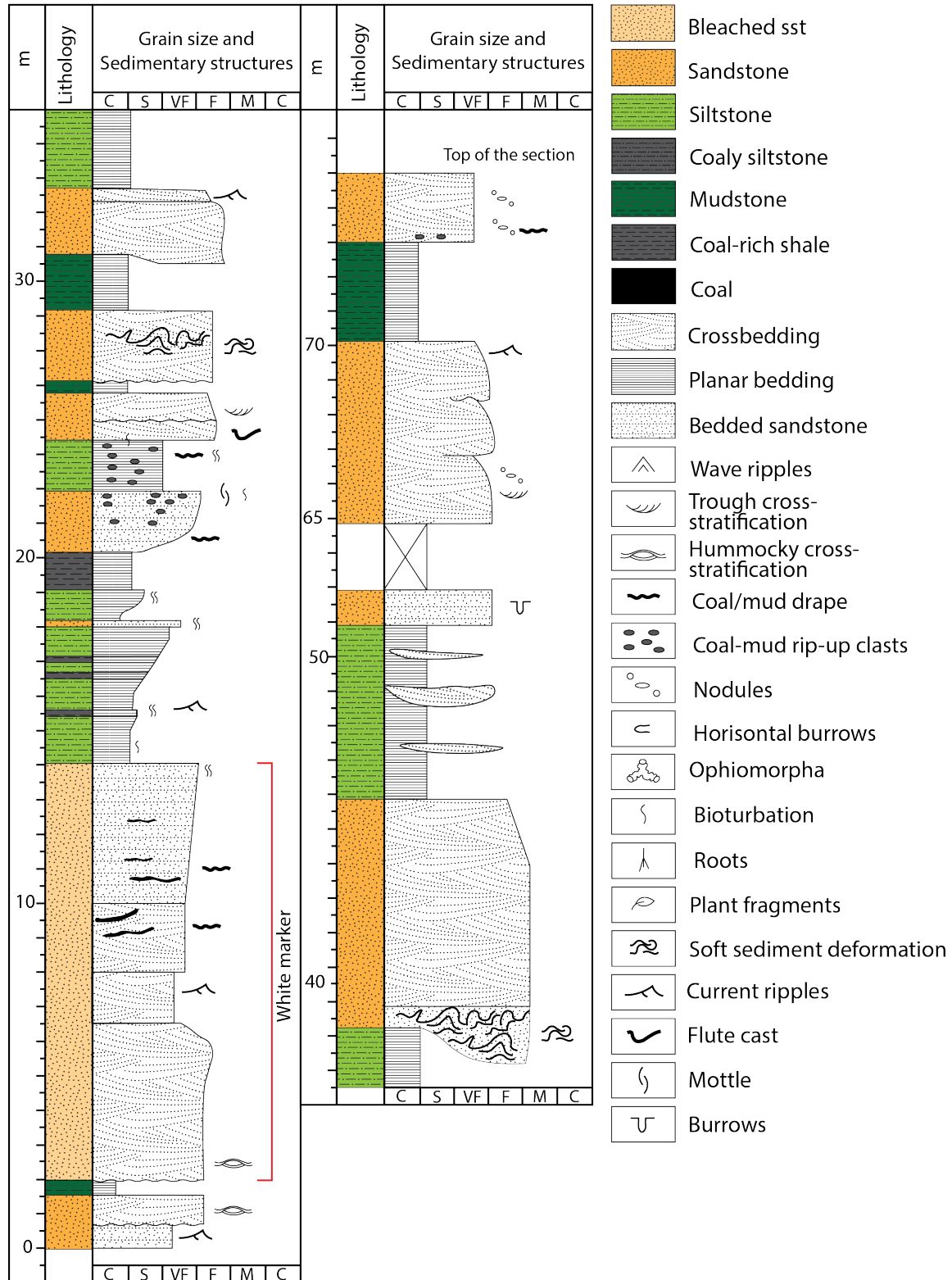


Figure Appendix 1 - Schematic illustration of logged section A. See Figure 5.2 for location. Logging was conducted by Alvar Braathen. Redrawn by Victoria Kjeldstad.

Sedimentary log B

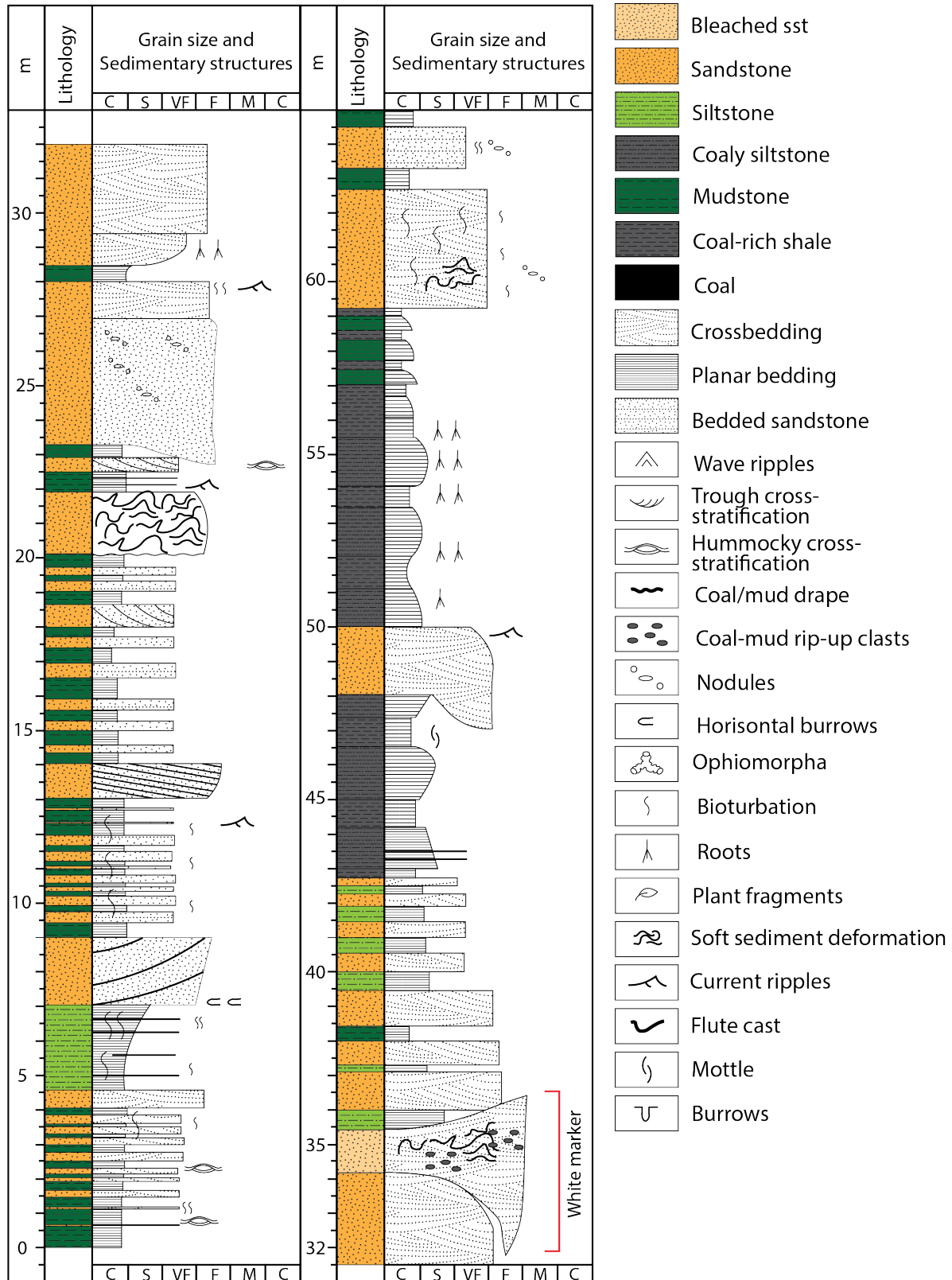


Figure Appendix 2 - Schematic illustration of logged section B. See Figure 5.2 for location. Logging was conducted by Alvar Braathen. Redrawn by Victoria Kjeldstad.

Sedimentary log C

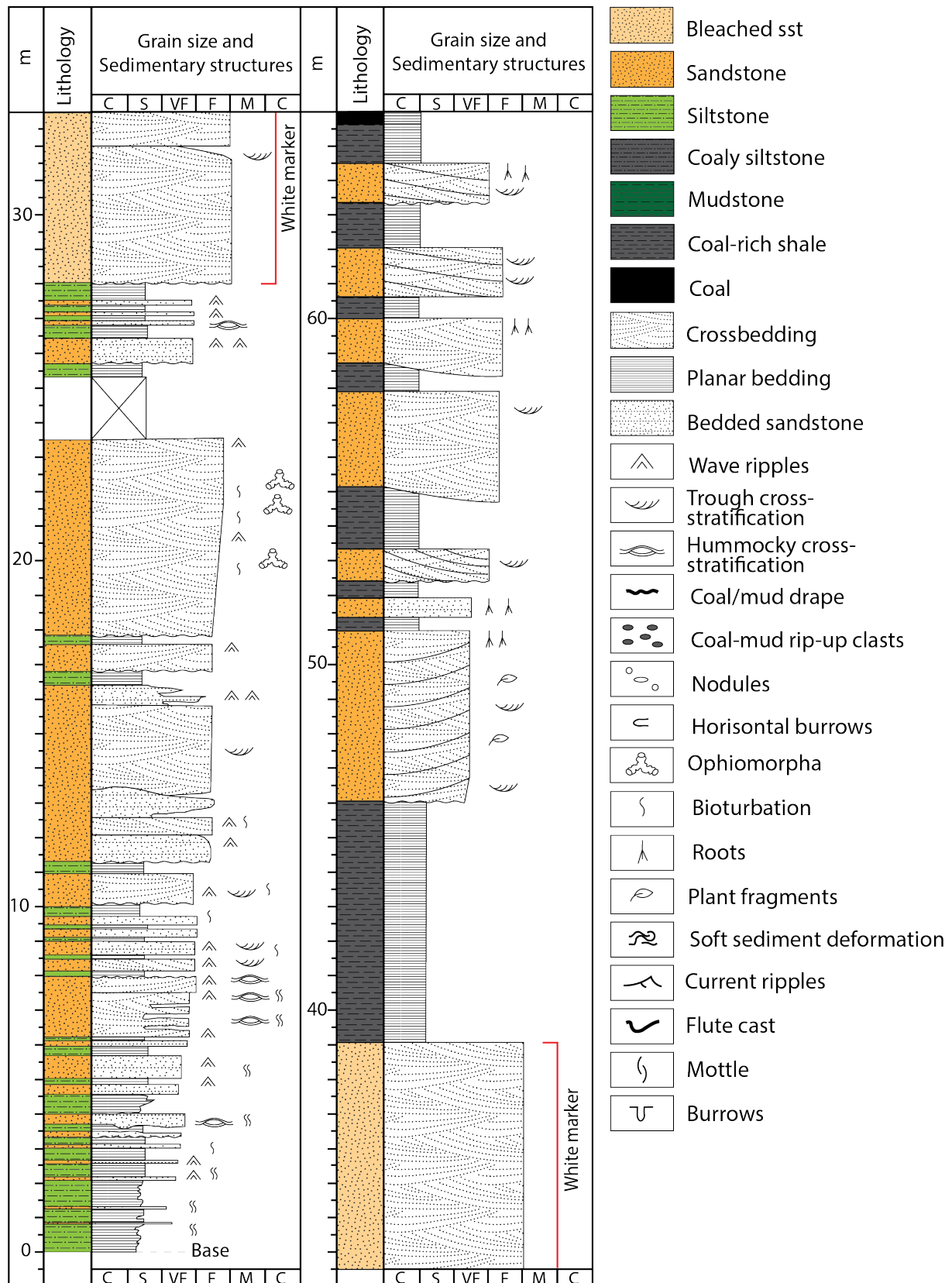


Figure Appendix 3 - Schematic illustration of logged section C. See Figure 5.2 for location. Logging was conducted by Rikke Bruhn. Redrawn by Victoria Kjeldstad.

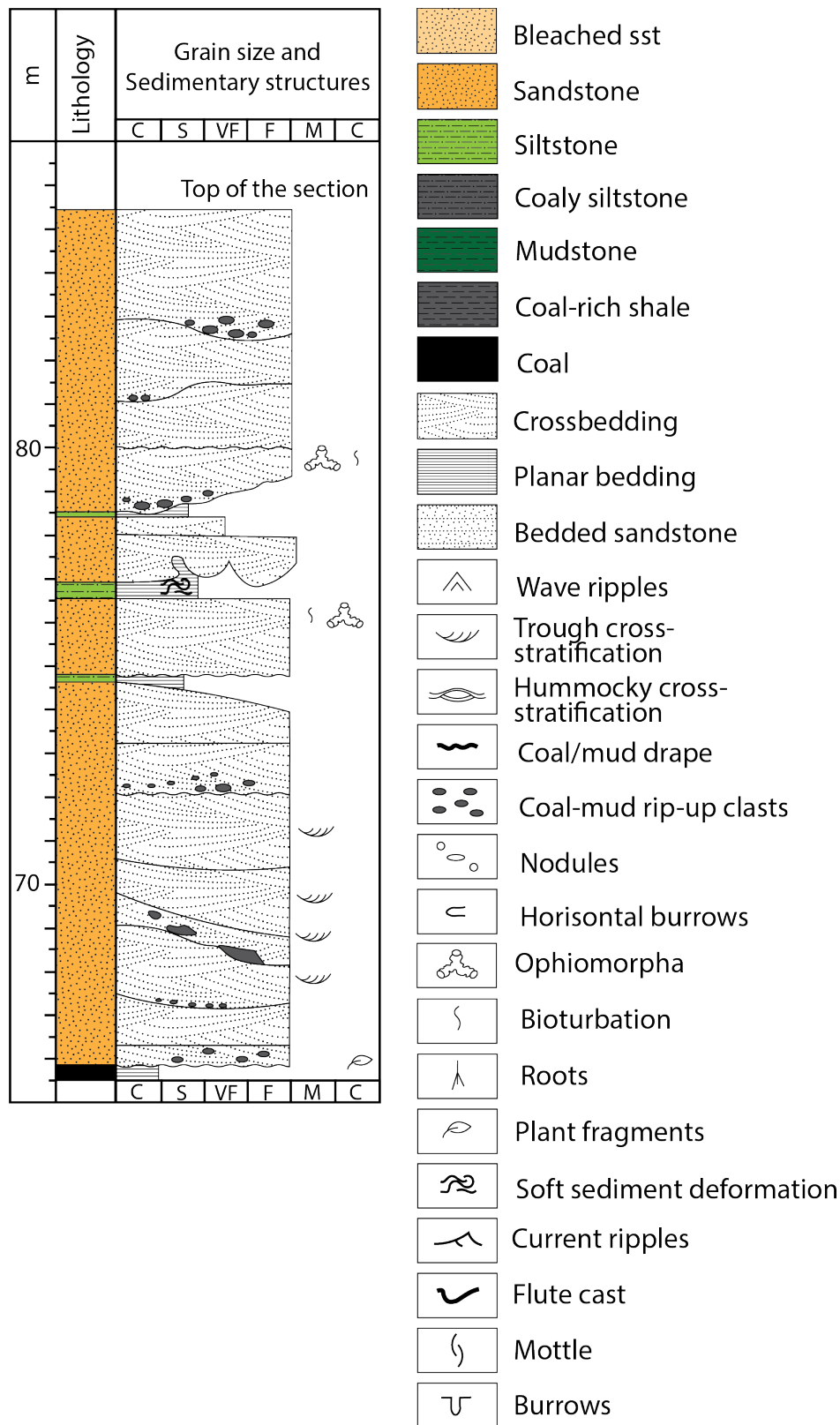


Figure Appendix 4 – Last upper portion of logged section C. See Figure 5.2 for location. Logging was conducted by Rikke Bruhn. Redrawn by Victoria Kjeldstad.